ABSTRACT

INVESTIGATION OF SMALL-SCALE ENERGY RELEASE AND TRANSFER PROCESSES IN THE SOLAR ATMOSPHERE WITH HIGH-RESOLUTION OBSERVATIONS IN INFRARED

by
Xu Yang

Solar spectrum in the infrared (IR) contains abundant information of solar activities, however, it has not been widely observed with ground-based solar telescopes. Diverse spectral lines in the solar IR spectrum provide different tools to probe the solar atmosphere in various heights. This radiation band in such relatively long wavelength includes various atom and molecule spectral lines that are generated by relatively small energy level transitions. The temperature-sensitive and highly-dynamic spectral lines could reveal the energy transmission process more easily than those in the visible wavelength of solar emission. Moreover, the better magnetic sensitivities for the infrared lines resulting from their longer wavelength make them detect the solar magnetic fields more precisely. Another reason to develop the IR solar physics is for its better observation seeing conditions.

With the advances in instrumentation techniques embodied in the 1.6-meter aperture Goode Solar Telescope (GST), Big Bear Solar Observatory (BBSO) has developed a series of high spatial and temporal resolution instruments in IR. Near-InfRared Imaging Spectropolarimeter (NIRIS) provides imaging spectropolarimetric data with the Fe I 15648.5 Å and imaging spectroscopic data for the He I 10830 Å, which offer powerful tool to detect the vector magnetic field in the deepest solar photosphere and the dynamic measurement from the high chromosphere to the low transition region, respectively. CrYogenic infRAred spectrograph (CYRA) is a new facility instrument that operates at the Near-IR wavelengths in 1-5 μm, which is not only powerful for photospheric magnetic measurement but also unique for chromospheric structure diagnostic.

The main achievements in this dissertation are as follows: (1) The high-resolution spectroscopic imaging in He I 10830 Å and H_α for a set of active region magnetic loops of different sizes I carried out. Movies made of blue and red wing images give counter-streaming motions, i.e., chromospheric absorption features in blue and red wing images move in opposite directions, at different strands. The moving pattern is detected with the local correlation tracking method and confirmed by Doppler shifts. For counter-streaming motions in long loops, I show that unidirectional mass flows in two opposite directions are accompanied by simultaneous weak EUV brightenings. (2) Observations with the GST, showing that the emergence of new magnetic flux occurred at the edge of a filamentary light bridge I presented. The emergence was accompanied by brightness enhancement of a photospheric overturning convection cell at the endpoints of the emerging magnetic structure. A fan-shaped jet was observed to be spatially and temporally correlated with the endpoint of the OCC intruding into the light bridge. My observation is the first report of flux emergence within a granular light bridge with evidence in the evolution of vector magnetic field as well as photosphere convection motions and supports the idea that the impulsive jets above the light bridge are caused by magnetic reconnection. (3) CYRA is the first fully cryogenic spectrograph in any solar observatory. It has been installed and the author is involved in the implementation, commission as well as the data acquisition and reduction for CYRA. The preliminary scientific results have been highlighted as well in this dissertation.

INVESTIGATION OF SMALL-SCALE ENERGY RELEASE AND TRANSFER PROCESSES IN THE SOLAR ATMOSPHERE WITH HIGH-RESOLUTION OBSERVATIONS IN INFRARED

by
Xu Yang

A Dissertation
Submitted to the Faculty of
New Jersey Institute of Technology and
Rutgers, The State University of New Jersey – Newark
in Partial Fulfillment of the Requirements for the Degree of
Doctor of Philosophy in Applied Physics

Department of Physics

December 2019

APPROVAL PAGE

INVESTIGATION OF SMALL-SCALE ENERGY RELEASE AND TRANSFER PROCESSES IN THE SOLAR ATMOSPHERE WITH HIGH-RESOLUTION OBSERVATIONS IN INFRARED

Xu Yang

Dr. Wenda Cao, Dissertation Advisor — Date
Professor, Physics, New Jersey Institute of Technology

Dr. Thomas Schad, Committee Member — Date
Assistant Astronomer, National Solar Observatory

Dr. Andrei Sirenko, Committee Member — Date
Professor, Physics, New Jersey Institute of Technology

Dr. Haimin Wang, Committee Member — Date
Distinguished Professor, Physics, New Jersey Institute of Technology

---

Dr. Zhen Wu, Committee Member — Date
Professor, Physics, Rutgers University - Newark

BIOGRAPHICAL SKETCH

Author: Xu Yang

Degree: Doctor of Philosophy

Date: December 2019

Undergraduate and Graduate Education:

- Doctor of Philosophy in Applied Physics,
  New Jersey Institute of Technology, Newark, NJ, 2020
- Master of Science in Astrophysics,
  Purple Mountain Observatory, Chinese Academy of Science, China, 2014
- Bachelor of Science in Optical Science and Technology
  Sun Yat-Sen University, Guangzhou, Guangdong, China, 2010

Major: Applied Physics

Presentations and Publications:

Yang, Xu and Cao, Wenda and Ji, Haisheng and Hashim, Parida and Shen, Jinhua, "High-Resolution Spectroscopic Imaging of Counter-streaming Motions in Solar Active Region Magnetic Loops", *The Astrophysics Journal Letter*, vol. 881, pp. L25. 2019

Yang, Xu and Yurchyshy Vasyl and Ahn, Kwangsu and Penn, Matt and Cao, Wenda, "Light Bridge Brightening and Plasma Ejection Driven by a Magnetic Flux Emergence Event," *The Astrophysics Journal*, Accepted on Oct. 1st. 2019

Yang, Xu and Ji, Haisheng and Li, Haochuan, "Multi-wavelength Analysis to Corona Heating Events", *ACTA Astronomical Sinica*, vol. 55, pp. 193. 2014

Hong, Zheng-Xiang and **Yang, Xu** and Wang, Ya and Ji, Kai-Fan and Ji, Haisheng and Cao, Wenda, "Location of Energy Source for Coronal Heating on the Photosphere," *Research in Astronomy and Astrophysics*, vol. 17, pp. 10. 2017

Li, Dong and **Yang, Xu** and Bai, Xianyong and Su, Jiangtao and Ning, Zongjun and Cao, Wenda and Deng, Yuanyong, "Spectroscopic Diagnostic of Sunspot Oscillation in Infrared and Ultraviolet Wavelengths", *The Astrophysics Journal*, Under Review

Şahin, S. and Yurchyshyn, V. and Kumar, P. and Kilcik, A. and Ahn, K. and **Yang, Xu**, "Magnetic Field Dynamics and Varying Plasma Emission in Large-scale Coronal Loops", *The Astrophysics Journal*, vol. 873, pp. 11. 2019

Wang, Ya and Su, Yingna and Shen, Jinhua and **Yang, Xu** and Cao, Wenda and Ji, Haisheng, "Hi-resolution He i 10830 Å Narrowband Imaging for an M-class Flare. II. Multiple Hot Channels: Their Origin and Destination", *The Astrophysics Journal*, vol. 859, pp. 148. 2018

Yang, Xu, "Observation of Light Bridge Brightening and Plasma Ejection Triggered by a Magnetic Flux Emergence Event", *Oral Presentation*, Triennial Earth-Sun Summit, Leesburg, VA, 2018

Yang, Xu, "Magnetic Flux Emergence Triggered Light Bridge Brightening and Reconnection Jets", *Poster*, COSPAR, Pasadena, CA, 2018

Yang, Xu, "Counter-Streaming Motions in Active Region Magnetic Arches Observed by Helium I 10830 Å Spectroscopy", *Oral Presentation*, AAS, St.Luis, MI, 2019

To someones, all his endeavor after grown-up originates from the deepest impression to the amazing world in the childhood. To me, it is the bright Beidou when I looking up to the sky in my third-grade summer.
有时候一个人一生的努力，都源于年少时印于心底的高大背影。对我来说，这个背影就是三年级夏天，在我仰望星空时看到的明亮的北斗。

For the love to Dad and for the memory to Mom.
献给我的爸爸妈妈，感谢他们无尽的爱。

ACKNOWLEDGMENT

Firstly, I would like to sincerely thank my advisor, Dr. Wenda Cao for guiding me into the academy of solar physics and introducing me to the experts in solar science and instrumentation filed. He provided me precious opportunities to get involved in advanced projects with frontier facilities and promising techniques. Without his wise advice or patient instruction, I could not have successfully finished my dissertation study in science and engineering. The most important thing I learned from him is to bravely confront the difficult scientific problems with tenacious spirit and never easily give up. With his tutoring, I achieved the ability to specify and solve the problems. With his mentoring, I am excited to search for the new academic problems that I am interested in. Moreover, the support I got from him during my graduate studies is not only in the academy, but also in my personal life. I am always grateful to proud of this interesting and fruitful graduate study experience with him.

Secondarily, I would like to deeply thank all of my committee members: Dr. Thomas Schad, Dr. Andrei Sirenko, Dr. Haimin Wang and Dr. Zhen Wu for their advice, support and taking the time to read my dissertation and give valuable feedback.

I am specially grateful to Dr. Haisheng Ji and Dr. Vasyl Yurchyshyn for their instructions during my science studies and their help in my life. With their advising on the scientific research based on the accumulated wealth of the knowledge in solar physics, I achieved deep understanding about the small-scale magnetic reconnection activities in the lower solar atmosphere. Other than advisors and collaborators in the science studies, they are my elder friends who changed and colored my life to the better. I am sincerely grateful for their comfort and encouragement when I met difficulties.

I would faithfully thank all my collaborators I have worked with and who have contributed to various parts of my research, particularly Dr. Matt Penn, Dr. Kwangsu Ahn, Dr. Xianyong Bai, Dr. Christine Beck and Dr. Kaifan Ji, who supported my research and broadened my knowledge through the precious discussions with them.

I am grateful to Ms. Erika Norro, Dr. Kwangsu Ahn, Dr. Wenda Cao, Dr. Phul Goode, Mr. Nicolas Gorceix, Mr. Jeff Nenow, Mr. Claude Plymate, Dr. Dirk Schmit, Mr. Sergey Shumko, Dr. John Varsik, Dr. Haimin Wang and Dr. Vasyl Yurchyshyn and all rest of the supporters at Big Bear Solar Observatory for their co-working and companionship. I really had a good time staying there during this dissertation work.

I appreciate the support from staff of Center for Solar-Terrestial Research and New Jersey Institute of Technology. Special thanks to Ms. Christine Oertel and Ms. Cheryl James for their professional work and kindly help in everything I asked for. I also would like to thank Ms. Clarisa Gonzalez-Lenahan, the Associate Director of the Office of Graduate Studies for her patient guidance and helpful support.

Also to all my friends especially Dr. Zhicheng Zeng, Dr. Xin chen, Ms. Nengyi Huang and Mr. Jiasheng Wang and my old friends in the Purple Mountain Observatory. I enjoyed the time sharing together with them which was full of happiness. The discussions with them inspire me. I would like to thank the Arkin family for providing me a warm and friendly residence.

Lastly but most importantly, I would like to thank all my family and friends who encouraged and supported me to pursue my academic degrees. My father, Jinde Yang strongly supported me to conquer any difficulties. I am proud to become a strong person like him.

TABLE OF CONTENTS

TABLE OF CONTENTS
(Continued)

Chapter **Page**

LIST OF TABLES

LIST OF FIGURES

Figure **Page**

LIST OF FIGURES
(Continued)

Figure **Page**

LIST OF FIGURES
(Continued)

LIST OF FIGURES
(Continued)

Figure **Page**

LIST OF FIGURES
(Continued)

Figure **Page**

CHAPTER 1

INTRODUCTION

1.1 Solar Physics

The Sun is one of the innumerable ordinary stars in the universe, however, it is the one that mostly related to the humanity. Benefiting from the sunshine, life, including mankind and all other creatures, get a chance to keep their necessary environment. From the round of day and night and the round of seasons to the changes of weather and the growth of plants, all these nature activities in the earth result from the solar activities. Historical documents recorded the rise and fall of the great dynasties are also influenced by the changes in the solar activities and the consequent changes in the climate. With the developments in the electric and electronic techniques, the modern civilization is highly dependent on the power system and integrated-circuits. Although the highly energetic particles that ejected by normal solar activities could be trapped and expelled by the terrestrial magnetic field, destruction and paralysis of power system and communication system, lead by the large and massive solar eruption event, may happen and indeed happened in 1859[1].

According to this close relationship between the Sun and the human life, people are spontaneously promoted to study the nature of the Sun. An important branch of the astrophysics has been developed to research and discuss the solar physical structure, the solar interior and exterior physical phenomena and its evolution process, which is called "**Solar Physics**". The meaning and importance for the solar physics could be concluded as follows: (1) The Sun is one of the common stars. The studies in solar physics will help us to understand the nature of the general stars. (2) The Sun provides an extreme physical environment which is difficult to replicate in the earth.

---

[1] Carrington Event: wikipedia.com

Thus, the Sun becomes an important and precious laboratory for the theoretical physics. (3) The studies to solar activities and the solar-terrestrial relationship has important practical meanings to the society and economy.

Observation shows the mean distance of the solar center to the terrestrial center, defined as one astronomical unit (1 AU), is approximately 1.496×10^8 km. At this mean distance: (1) It takes 8 minutes 19 seconds for light to travel from the solar surface to the terrestrial surface. (2) Each one arc-second (") in the plane of sky equals to 725.3 km. (3) The observed solar radius is $R_\odot$=960"=6.963×10^{10} cm, which is 109 times to the Earth's radius. Calculate with the Kepler's third law of planetary motion, the solar mass is $M_\odot$=1.989×10^{33} g, and the averaged density is ρ=1.408 g/cm^3.

The solar constant, S, is the amount of power that the Sun deposits per unit area that is directly exposed to sunlight at the mean distance. It is measured as S=(1367±2) W/m^2, by the "Solar Maximum Mission" satellite. Other words, the total solar luminosity is $L=4\pi A^2 \cdot S=3.828\times10^{33}$ erg/s.

1.2 Solar Structures

The Sun is a Main sequence star in the Hertzsprung-Russell diagrams. Its G2V spectrum indicates the surface temperature of the Sun is approximately 5,778 K. The interior temperature of the Sun is much higher. Under this kind of high temperature, all materials in the sun are excited as plasma. According to the standard solar model, the structure of the Sun is formed with different spherical layers. From the interior to exterior, these layers, shown in Figure 1.1, are: core, radiative zone, convective zone, photosphere, chromosphere and corona. The core, radiative zone and the convective zone form the solar body. The photosphere, chromosphere, transition region and corona form the solar atmosphere, as shown in Figure 1.2.

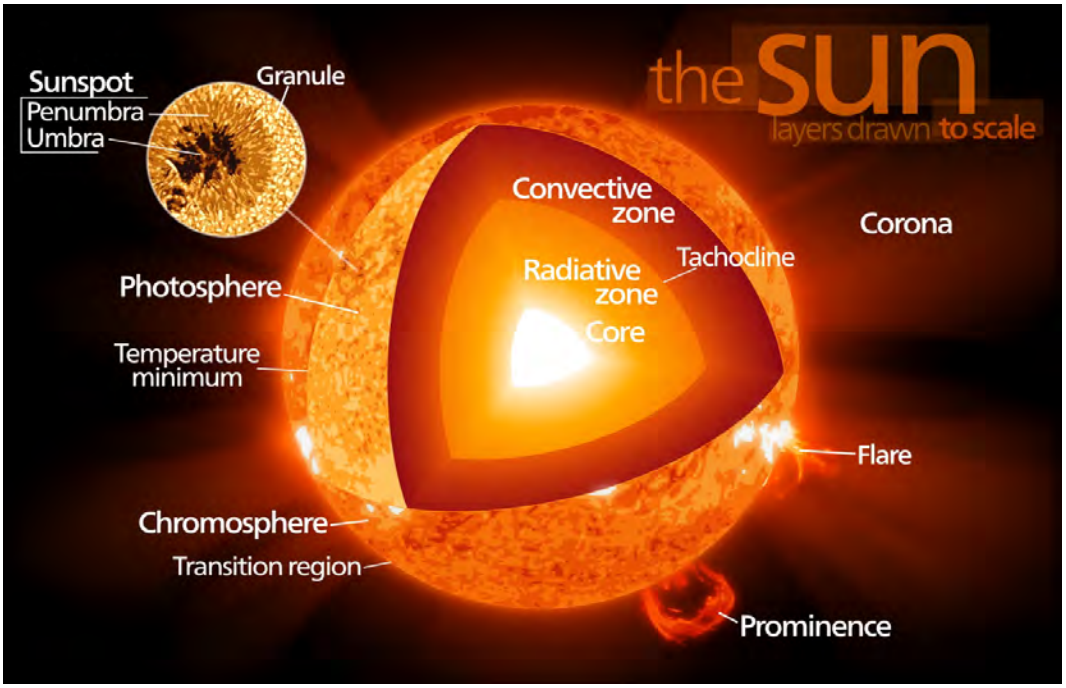

Figure 1.1 Diagram of solar structure.

Source: wikipedia.org

1.2.1 Solar Core

The region from the solar center to about one quarter of $R_{\odot}$ is the solar core. According to density as high as 151 g/cm^3, the solar core contains two percent of solar volume and half of the $M_{\odot}$. Continuous nuclear fusion occurs under extremely high temperature and pressure and huge amount of energy are released during the process when Hydrogen fuses into Helium through the proton-proton chain and CNO cycle.

1.2.2 Radiative Zone

From one quarter to three quarters of the $R_{\odot}$, the temperature drops from approximately 7 million K to 2 million K.Convection is not created in this region so that the thermal radiation is the primary method of energy transfer. After scattered innumerable times in this region, the high frequency gamma photons from the solar core are transferred to the convective zone within $\sim 10^7$ years and transformed to lower frequency visible photons during this process.

1.2.3 Convective Zone

Utilizing the high-resolution helio-seismology data, scientist find that a region with high temperature gradient are formed from 0.7 $R_\odot$ to the solar surface, due to the increases of the medium opacity. When temperature gradient become lager than the adiabatic temperature gradient, convection instability are created and the convection region is constructed. According to the solar dynamo theory, this region is the origin of the solar magnetic field. Based on the observation to the solar atmosphere, the convection cells are presented as granulation pattern, medium granulation pattern and super granulation pattern. These patterns are correspond to the ionization-recombination of H I, He I and He II, respectively.

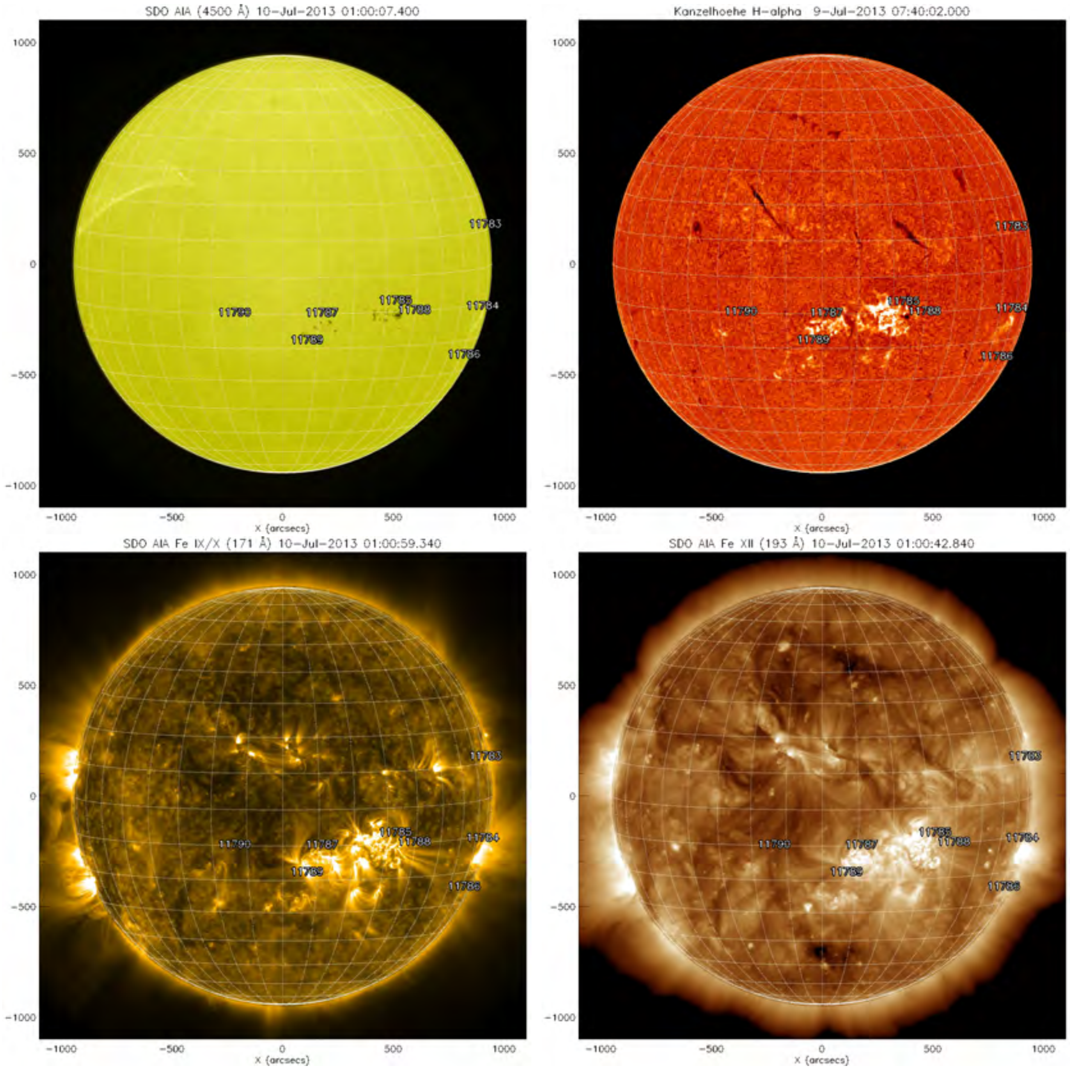

Figure 1.2 Images of solar atmosphere in photosphere, chromosphere, transition region and solar corona.

Source: solarmonitor.com.

1.2.4 Photosphere

The bottom of the photosphere is defined as where the optical opacity of 500 nm light equals one (τ_{500}=1 and h=0). From here, temperature decreases with height and finally researches a minimum value around 4200 K. Recent studies report the existence of "cold" gases, which are not stable in the temperature of 3700 K. Normally, this temperature minimum layer (T_{min}) is considered as the top of the photosphere.

The Photosphere is about 500 km thick and its particle number density is about 10^{16} /cm^3. Almost all the visible lights are radiated by the this thin layer and this is the reason how the name of photosphere comes from. The radius and surface of the Sun are defined with the top boundary of the solar photosphere. People can observe the sunspot, granulation (Figure 1.3), medium granulation, super granulation and facula in the photosphere.

Sunspots are straight forward and striking phenomena on solar surface. They are presented as dark and cool features and stand for the solar magnetic activities. Sunspots have been observed by naked eyes since 2000 years ago and they are observed by modern telescopes in various of wavelengths from gamma ray to microwave. A simple sunspot is composed of a dark core and surrounding filamentary structures, which are named as umbra and penumbra.

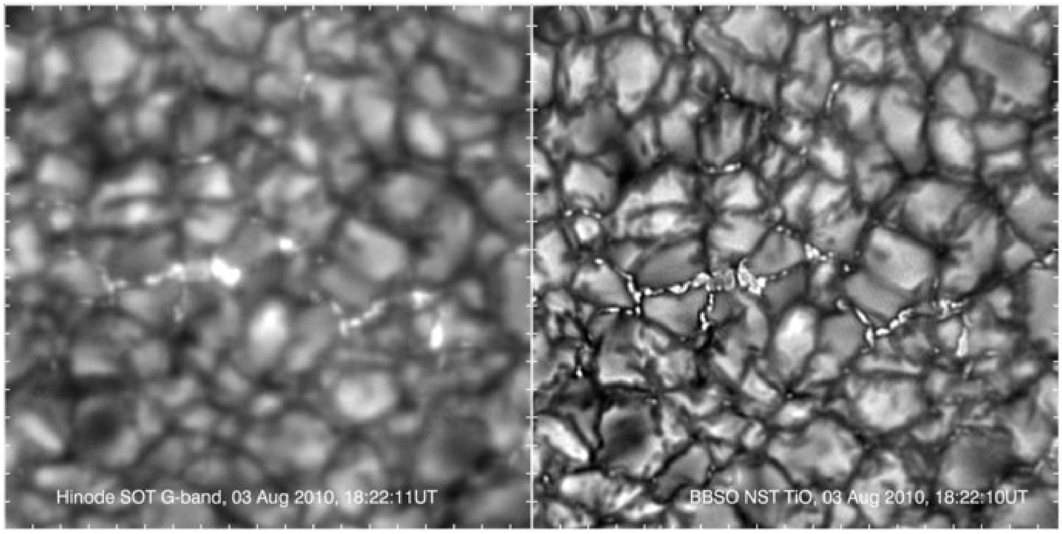

Figure 1.3 Observations to the granulation. Left: observed by Hinode/SOT. Right: observed by BBSO/GST.

Source: Abamenko et al., 2012[3].

1.2.5 Chromosphere

The layer exterior to the photosphere is chromosphere. The chromosphere stars from h=500 km. It is thicker than the photosphere and its outer boundary is irregular. Commonly, the thickness of the chromosphere is considered as several thousands kilometers. The chromospheric plasma is quite homogeneous under h=2000 km, and in the form of spicule-like structures above that height. On one hand, the particle number density in the chromosphere is much lower than that in the photosphere. On the other hand, its temperature is much higher. The chromospheric temperature is 4200 K at the bottom and reaches 2×10^4 K at the top. Scientists normally observe the chromosphere with Hα line, Ca II H line and K line. The observable features include chromospheric network, plage, filament and prominence. Figure 1.4 shows the chromosphere observed in Hα.

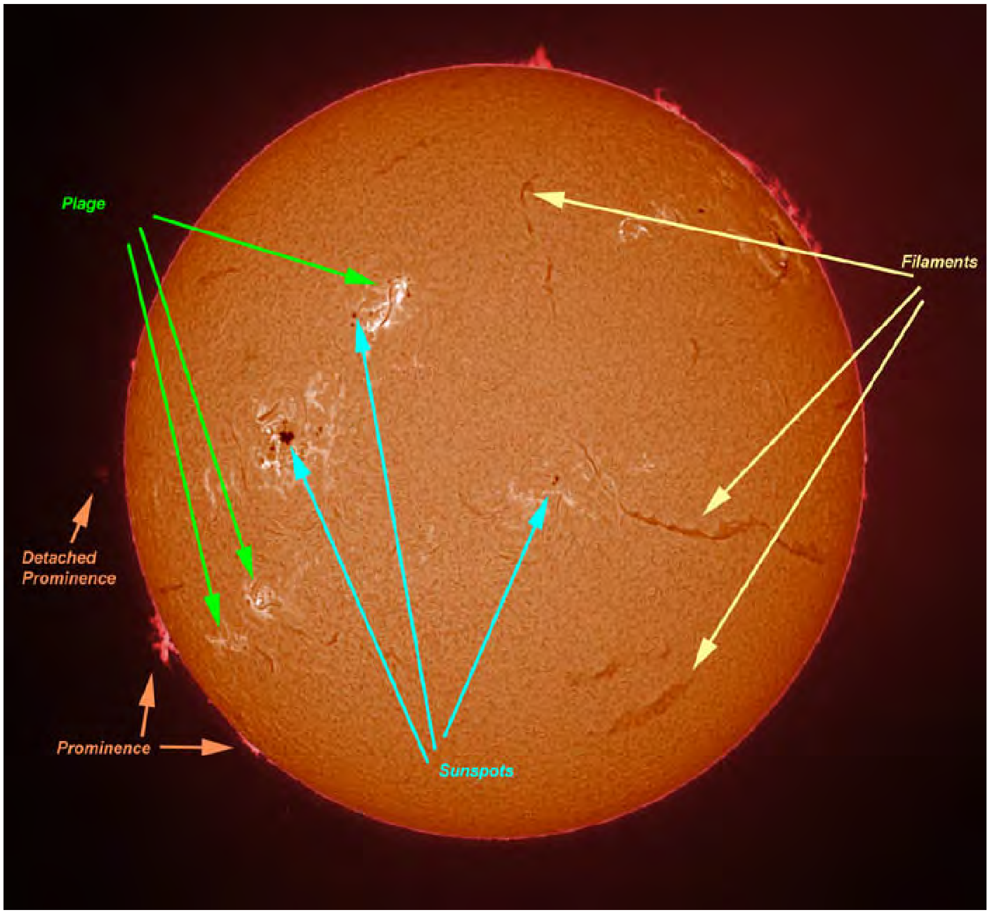

Figure 1.4 Solar chromosphere and the observable features.

Source: wikipedia.org.

1.2.6 Transition Region

Transition region is a layer as thin as 200 km, locating between chromosphere and corona. The temperature increases from 2×10^4 K to 10^6 K in this region. According to the spatial inhomogeneity of the hot plasma, its definition with temperature is more accurate than the definition with height. The transition region is defined as the region where LogT=4.5∼5.5 in some studies. The best wave band to observe the transition region is the Extreme Ultra-Violet (EUV) band.

1.2.7 Corona

Above the transition region, the next layer is solar corona. The temperature of corona can reach to 2×10^7 K. Solar corona has no regular appearance and no obvious boundary. According to its extremely high temperature, the corona beyond several solar radius are expending and creates the solar wind. In the general definition, solar corona extends with the solar wind and finally approaches to the boundary of the solar system. In normal situation, the luminosity of corona is 6 orders lower than the photosphere. Therefore, scientific observation to solar corona should be taken during the solar eclipse or with specially designed coronagraph.

Coronal light comes from three primary sources. The K-corona (K for kontinuierlich, which means "continuous" in German) is created by the Thompson scattering between sunlight from photosphere and free electrons in the corona. Strong Doppler broadening obscures the spectral lines in the scattered light and produces a continuous spectrum. The F-corona, named after by Joseph Fraunhofer, is created by the sunlight scattered by dust. The original Fraunhofer spectral absorption lines can be observed in the F-corona. The E-corona, or emission corona, consists large amount of emission lines produced by highly ionized coronal plasma.

According to the MagnetoHydroDynamic (MHD) theory, the coronal plasma is frozen with the magnetic field. Therefore, the observed coronal features represent for the distributions of coronal magnetic field. Modern high resolution corona images shows the corona loops in the solar active regions (AR), corona holes in the quiet Sun regions (QS) and plums near the polar region. Coronal helmet and coronal rain can be observed much brighter than the surroundings in the AR.

As solar corona is three orders hotter than photosphere and the second thermal-dynamic law prevents heat flowing directly from cooler temperature object to hotter object, the coronal heating problem become an hot and maybe the most important topic in solar physics.

The corona plasma is so hot ($\sim 10^6$ K) that the thermal radiation process will cool it down quickly, unless there is sufficient and continuous heating mechanics to provide energy from the lower atmosphere. Scientists created many different theoretical models to interpret the potential methods to transfer the energy. Current hypotheses can be classified into two types: heating through MHD waves (Schatzman 1962[4]) and through nano-flare based on magnetic reconnections (Parker 1988[5]). Up to now, most of the relevant studies are based on the statistics or numerical methods and lack of the support from high resolution observation evidence. One of the motivation of this dissertation is to study the energy transfer process for the photosphere to transition region through the chromosphere.

1.3 Infrared Solar Physics

From simply counting sunspots to launching space crafts with multi-wavelength detectors, solar observations have been made in the past hundreds of years, and have made a series of significant science achievements. However, the infrared window to the Sun is quite "young". After William Herschel's discovery of infrared radiation in 1800, this wave band – red-ward to the visible limit of human eyes – was not completely opened until the last decades due to the telluric distortion.

A fair question is "why we are making our best effort to get solar infrared radiation data, rather than just using other backup windows that can be observed relatively easier?" The answer is: there are many properties make the infrared solar observation so different and irreplaceable, both in advantages and disadvantages, for the consideration of science and instrumentation.

Atmospheric seeing is the main factor that prevents the ground-based telescopes from approaching their diffraction limits. This is why a large ground-based solar telescope have no better resolution than a backyard telescope with 20 cm aperture, under bad atmosphere distortion. Things become better until the Adaptive Optics (AO) system were applied in. However, the AO system is much more like a kind of icing on the cake, not a timely help. There is a quantity, known as Fried parameter r_0, which measures the optical quality of the atmosphere, shown as:

r_0=[0.423 $\mathrm{k}^2 \sec\beta \int C_2^n(\mathrm{z})\mathrm{dz}] \propto \lambda^{\frac{6}{5}}$

Seeing improves when wavelength increases, just as what have been known from long time observation experience. And this mechanism improves the performance of AO system in two ways – enlarge the correctable angle and increase the time scale of atmosphere stability. At the same time, there are some other instrumentation advantages for infrared solar observation, for example, less atmospheric scattering, less instrumental scattering and less instrumental polarization.

Earth's atmosphere scatters blue light much more than red light and infrared, which makes the sky blue on one hand and makes the red light to be the best warning sign on the other hand. As shown by the approximate solutions of particle simulation, scattering coefficient varies with λ^{-4}, which is also confirmed by early observations with the dependence of $\lambda^{-1.7}$ Penn 2014[6].

Both of the reflection and refraction telescopes suffer from the scattered light inside the light path. For the ideal condition, under which the mirrors are perfect clean, the total scattering could decrease by a factor of 100 as the wavelength moving from 1.15 microns to 10.6 microns. However, the scattering coming from the dust on mirrors contributes more to the total integrated scatter, than the diffuse reflection caused by the surface roughness. Thus, real measurement and the simulation show that the actual scattering only decreases by a factor of 20.

From the scientific aspect, it is also more precise to take the magnetic field measurement through the infrared window. For example, the magnetic sensitivity in infrared spectrum observation is greatly increased – compared to those observed with the visible lines. The Zeeman splitting of atomic sub-level in a static magnetic field varies with $\lambda^2 \cdot \mathrm{g}_{eff}$, where the g_{eff} is called effective Landé factor. The ratio of Zeeman splitting to the spectral line width ($\lambda \cdot \mathrm{g}_{eff}$) is defined as the magnetic resolution of a spectral line. Table 1 gives a list of magnetic sensitivities of some solar spectral lines. A larger value of g_{eff}, of course can make some help to give a better magnetic sensitivity during the observation, however it is more efficient to increase the wavelength to make a more accurate magnetic field measurement (magnetic sensitivity increases by a factor of 10 with the observing wavelength increases from 500 nm to 5000 nm).

Another scientific advantage for infrared solar physics is that there are a large number of molecular rotation-vibration lines. Changes in rotational state lead to microwave emission and changes in vibrational states, always coupled by

Table 1.1 Magnetic Sensitivity of Spectral Lines

Region	*Atom*	*Wavelength [nm]*	g_{eff}	$\lambda{\cdot}g_{eff}$
Photosphere	Fe I	525	3.0	1575
	Fe I	630	2.5	1575
	Fe I	1565	3.0	4695
	Ti I	2231	2.5	5778
	Fe I	4064	1.25	5080
	Fe I	4137	2.81 ?	11625 ?
	Mg I	12318	1.0	12318
Chromosphere	Ca I	854	1.1	939
	Mg I	3682	1.17	4307
	Ca I	3697	1.1	4067
Corona	Fe XIV	530	1.33	706
	Fe XIII	1075	1.5	1612
	Si X	3934	1.5	5901

Source: M.J.Penn, 2014[6].

the changes in rotational states, lead to the infrared emission. Making a simple approximation,with the parameters of water molecule and solar surface temperature of 6000 K, considering the rotational energy equals to the thermal energy of molecule itself, it will produce an infrared emission with a wavelength of 25 microns. Due to the thermal instability, molecules only exist in the coolest regions on the Sun. In all other regions, these molecules can not remain for a long time and will be easily destroyed by the thermal perturbation. This feature, on one side, limits the observation objects; on the other side, provides us a way to probe the cool regions around the sunspot and the temperature minimum in the quiet sun.

The solar continuum radiation is mainly produced by the H-minus bound-free transition at the wavelength shorter than 1.6 microns, and then dominated by the H-minus free-free transition when wavelength becomes longer. It offers the biggest optical depth at 1.6 microns, where people can see the deepest level into solar atmosphere —- 40 km blow the photosphere bottom (where the optical depth is 1, observed at 500 nm wavelength). Although it seems to be a small height difference, it does make great help to observe the much stronger magnetic field in the deeper photosphere.

Of course, there are also some disadvantages of infrared solar observation. Instrumentally, comparing to the shorter wavelength optical window, telescopes give less spatial resolution for longer wavelengths, due to the diffraction limit. And also, as a 300 K black body emits at the peak of 9656 nm, the ground based infrared solar observation suffers from increased background levels and small signal to noise ratio. Even if with very good cooling system, a variety of observation method should be used to increase the data quality. Scientifically, the observation in infrared wavelength will face the problem of fewer solar photons and fewer atomic absorption.

1.3.1 Research Motivation and Dissertation Outline

The key scientific problem that author would like to solve is the energy and mass transferring mechanics in the lower solar atmosphere from photosphere bottom to temperature minimum region and from chromosphere to transition region. In the purpose of utilizing the benefits for IR observations mentioned above, I developed several advanced focal plane IR instruments for the GST at the BBSO, which are the Near InfRared Imaging Spectrometer (NIRIS) and CrYogenic infRAred spectrograph (CYRA). NIRIS can perform observations in Fe I 15648 Å channel and He I 10830 Å channel, which target on the magnetic field at the bottom of photosphere and the ejection activities at higher chromosphere and lower transition region, respectively. CYRA focuses on the spectrum at the mid IR between 1∼5 microns, the first light studies will be performed with Carbon-monoxide (CO) 4667 nm spectrum and Ti I 2231 nm spectrum, which contain the thermal and oscillation signals in the temperature minimum region. The introduction to data acquisition and analysis tools will be described in Chapter 2.

In this dissertation, I focused on three works: (1) In order to study the magnetic flux emergence (MFE) process, I performed two different Stokes inversion methods on Fe I 15648 Å spectropolarimetry date to obtain the vector magnetic field maps. Comparing photospheric vector magnetic field data, continuum emission data and chromospheric spectroscopic data, I got a chance to study how the magnetic field emerges from the bottom of the photophere and interacts with the back background AR magnetic field. Plasma is ejected to the chromosphere from the photospheric reconnection footpoint and energy is transferred upward after the MFE process. (2) In order to study the fast mass ejection event and mass flow process in the chromosphere and transition region, I studied and practiced the image processing for the He I 10830 Å imaging spectroscopic data. I performed the data reconstruction step by step from dark and flat fielding, speckle reconstruction to developing Doppler maps, combined multi-wavelength maps, flow maps and performing wavelet analysis. I discovered the counter-streaming flow pattern in the transition region loops above an emerging flux region (EFR).(3) In order to study the IR emissions in the temperature minimum region, I put efforts into the instrumentation work and developed a new focal plane IR instrument. By processing and analyzing the original CO data, I find the propagation patterns for the oscillation from the temperature minimum region to the transition region.

The studies and results of work (1) and (2) will be stated in Chapter 3 and 4, respectively. The engineer work and first light of data analysis of CYRA will be shown in Chapter 5.

CHAPTER 2

INSTRUMENTATION AND DATA REDUCTION

2.1 Data Sources

2.1.1 Ground-based Observations with Goode Solar Telescope

GST, the 1.6-meter aperture Goode Solar Telescope is in operation and taking scientific data in Big Bear Solar Observatory (BBSO). It is a new generation ground-based high-tech solar telescope and it is also the largest optical solar telescope right now (GST/BBSO, Goode et al., 2010[7]; Cao et al., 2010a[8]). Its off-axis design and open structure – with wind gate and exhaust system on the dome – helps to maintain the static thermal environment and clear the concentrations of heat around the optical paths.

GST is equipped with high-order adaptive optics (AO) and its focal plane instrumentation, which includes broadband filter imager – BFI; visible imaging spectrometer – VIS; near-infrared imaging spectropolarimeter – NIRIS; fast-imaging solar spectrograph – FISS; and cryogenic infrared spectrograph – CYRA.

Advanced AO system, **AO-308**, is now in service for GST, helping the whole telescope system approach to its diffraction limit with high temporal resolution. AO-308 utilizes a wavefront sensor of 308 sub-apertures across the telescope pupil. In most of observing time, the high order AO-308 can help GST acquire the diffraction limit of the telescope. New generation Multi-conjugate AO system is being developed by BBSO and the testing is promising. People should expect a great improvement in future observation.

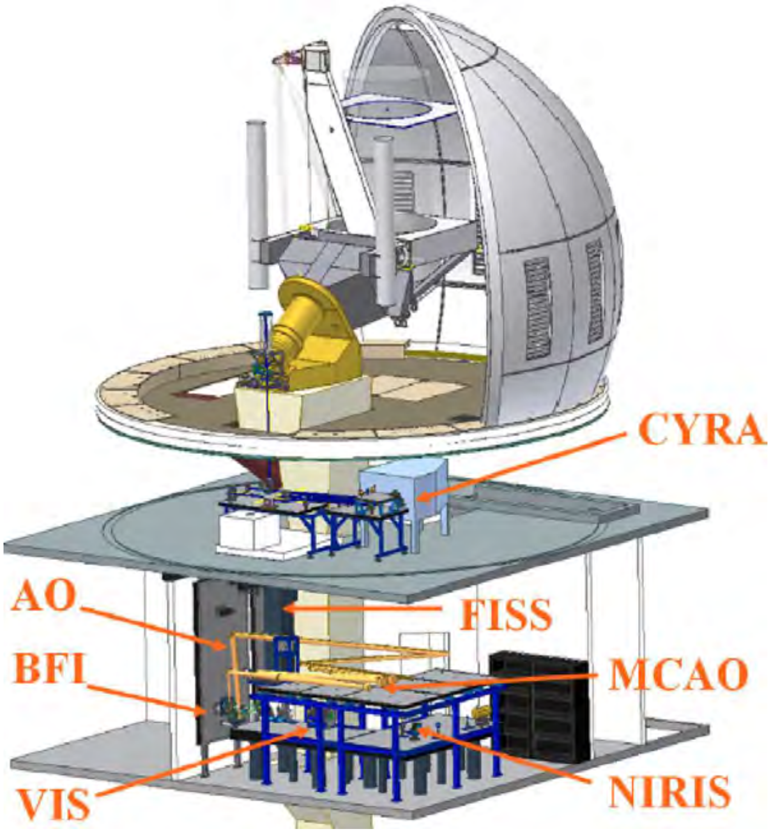

Figure 2.1 A schematic of the Goode Solar Telescope at Big Bear Solar Observatory (GST/BBSO), including the dome and observational instruments.

Source: bbso.njit.edu

BFI provides solar photospheric continuum context data using a high-speed 2k × 2k CCD camera. When working at TiO 7057 Å with a 10 Å interference filter, BFI provides an AO-corrected 70" × 70" field of view (FOV). Typically, each BFI observing burst contains 70 image frames and the exposure time for each frame is 0.18 ms. The temporal cadence is normally set to 15 or 30 s depending on the seeing condition.

VIS is based on single Fabry-Pérot etalon to produce a narrow bandpass (0.07 Å) over a 74" × 68" circular FOV at 0".29/pixel image scale, tunable from 550nm to 700 nm. There are 13 pre-set wavelength positions with the possibility to choose an arbitrary number of positions during observations, which are 0, ±0.2, ±0.4, ±0.6, ±0.8, ±1.0, ±1.2 Å form the H_α line center at 6563 Å. Typically, a burst of 25 frames are taken for each wavelength position with the exposure time varying from 7 to 25 ms when moving from line wings to line center. The cycle cadence depends on the number of scanning wavelengths and the size of the burst and may range from 3 to 30 s.

NIRIS uses a dual Fabry-Pérot etalon that provide an 85" round FOV imaged on a Teledyne camera, Which is a 2k × 2k HgCdTe, closed-cycle Helium cooled IR array. The primary spectral lines used by NIRIS are the Fe I 15648 Å and the He I 10830 Å red component. The Fe I bandpass is 0.1 Å while the He I bandpass is 0.05 Å.

In Fe Channel, a dual beam system simultaneously capture two-polarization states side by side, each 1k × 1k pixels in size, resulting in an image scale of 0".083/pixel. The polarimetry measurements are performed using a rotating 0.35λ wave plate that allows us to sample 16 phase angles at each of more than 60 line positions (40 in the Fe 15648 Å) at a cadence of 30 s per full spectroscopic measurement (full-Stokes I,Q,U,V). 16 images are taken at each line position and the exposure time for each frame is 33 ms.

NIRIS offers an imaging spectroscopic observations in He channel, with a bandpass of 0.05 Å and an image scale of 0".063/pixel. Typically, NIRIS takes about 3 s for an acquisition of a burst of 40 frames in one certain wavelength point to achieve high temporal resolution data set, the spectroscopy observations were performed at line center and ±0.2, ±0.4, ±0.6, ±0.8 Å of the He I 10830 Å line red component.

CYRA, is a newly developed focal-plane instrument for GST, located at one floor beneath the telescope deck (shown in Figure 2.1). The scientific objective of CYRA is to make the solar spectrum observation at mid IR wavelength of 1-5 microns. The detailed description of CYRA instrument will be introduced in the Chapter 5.

2.1.2 Space-based Observations

The solar transition region and corona, exhibits extraordinary high temperature, are dominated by high energy EUV and X-ray radiations.

The GST data set was complemented by the data taken by the instruments onboard the Solar Dynamics Observatory (SDO) and the Interface Region Imaging Spectrograph (IRIS). SDO data is the mostly used. Its facility instruments Atmosphere Imaging Assembly (AIA) provides images from all layers in solar atmosphere. Helioseismic and Magnetic Imager provides photosphere white light image and vector magnetic field data. IRIS provides photosphere, chromosphere and transition region images with selected spectral information.

2.2 Data Reductions and Analysis

2.2.1 Reduction for Imaging Data

The GST photospheric TiO and chromospheric Hα, He I 10830 Å data were dark-fielded, flat-fielded, bad pixels corrected and then speckle reconstructed using the Kiepenheuer-Institute Speckle Interferometry Package code[9]. A sample imaging data reduction flow is shown in Figure 2.2. Additionally, the Hα data set was processed with two-dimensional Discrete Wavelet Transform (DWT) and Principal Component Analysis (PCA) reconstruction methods to remove noise patterns in the reconstructed Hα images. The utilized technique works as follows. First, an image is decomposed by 4th-order Daubechies wavelet with four levels and an approximation is generated as well as horizontal and diagonal coefficients for each level. Second, I applied PCA reconstruction technique to the horizontal and vertical coefficients at each level to extract the horizontal and vertical pattern of coefficients in the wavelet domain. Next, I recomposed the extracted coefficients by an inverse DWT and generated image with horizontal and vertical noise pattern in a spatial domain. Lastly, I removed the noise patterns from the observed image.

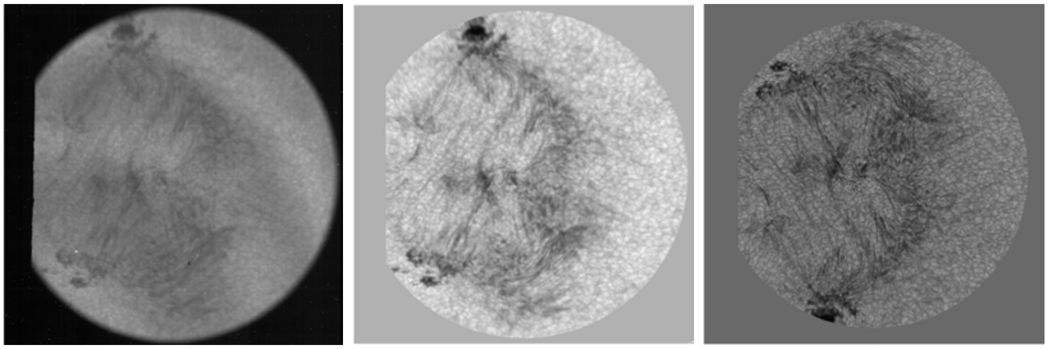

Figure 2.2 Reduction flow of imaging data. Left panel: raw image with bad pixels and interference fringes. Middle panel: dark-fielded, flat-fielded and bad pixel corrected image. Right: speckle reconstructed image.

2.2.2 Reduction for Spectopolarimetric Data

For the NIRIS Fe I 15648 Å data, I applied two inversion methods to its Stokes profiles. The Milne-Eddington (ME) inversion code used in this study was developed by J. Chae, and its early version was applied to the Hinode/SP data[10]. An inverted data set includes nine parameters among which are the total magnetic field flux density, the inclination and azimuth angles, and the Doppler shift. This code uses a simplified model of solar atmosphere and performs very fast inversion, which is desirable when inverting a large data set. I applied it here to a series of spectropolarimetric line profiles to analyze the temporal evolution of the MFE event.

To better understand the height dependence of the magnetic field and to obtain reliable thermal information, a more complex inversion should be used. For this purpose, I applied a Stokes inversion method based on Response functions (SIR) developed by Ruiz Cobo & del Toro Iniesta, 1992[11]. A simple SIR inversion model with one-component (1C) gradient magnetic field configuration – 3 nodes for perturbing temperature, linearly evolving magnetic strength, line of sight (LOS) velocity, inclination, azimuth and no straylight correction applied – works well for the umbra, the LB and the most part of the penumbra in this region. The inversion results contain data for different solar atmosphere heights ranging from Logτ = 1.4

to Logτ = -4. A comparison of the inversion result between the two methods are presented in Figure 4.3. I resolved the 180-degrees ambiguity by using HMI/SDO ambiguity-resolved vector magnetic field as reference and applying the acute angle approach, i.e., azimuth was assigned in the direction that was making smallest angle with the corresponding HMI azimuth.

One problem for the SIR 1C inversion is that it can not properly reflect the real magnetic structures in complex EFRs. Some of the fitting samples are provided in Figure 2.3. The last column of Figure 2.3 shows that 1C inversions work well for the brightening at the LB OCC region and only one strong vertical magnetic field component may be used to invert the data at this pixel. The left column displays the observed Stokes profiles and the 1C inversions the at point 0. The thing to notice is that the lobes in the observed Q profile are closer together than those in the V profile and they have smaller width. As for the 1C inversions, the lobes in the inverted Q profile are simply too broad to fit the observed ones, but they match the width of Stokes V lobes. The reason why the 1C inversions failed to match the observations is that at this pixel I probably have a mix of two magnetic components. The one that is more horizontal and produces the Stokes Q signal has a lower field strength, while most of the contribution into the Stokes V comes from a more vertical component This is why the lobes in Q have a lower width, while Stokes V lobes are more separated.

With an ultra-strong gradient (nodes for B/gamma/phi $\geq$ 2), I can "emulate" those two different components in one stratification, however the fields have then to change their inclination by about 90 degrees within the range Logτ 0 to -2, and their fields flux density has also to change rapidly within that narrow spatial range. In this case, a two-components (2C) magnetic field model is needed for those pixels that display this kind of Stokes profiles (Figure 2.3, second column).

We then applied a 2C inversion atmospheric model to selected pixels of interest, and assigned two nodes for temperature with a constant magnetic field and LOS velocity, For point 0, the 2C inversion resolved a slightly inclined strong vertical magnetic field component (which dominates the penumbra region) and a weak horizontal magnetic field component (which is common in the flux emergence region). Similarly, for point 3 located at the magnetic minimum region, I found an opposite polarity magnetic field component that is mixed with the background penumbra magnetic field.

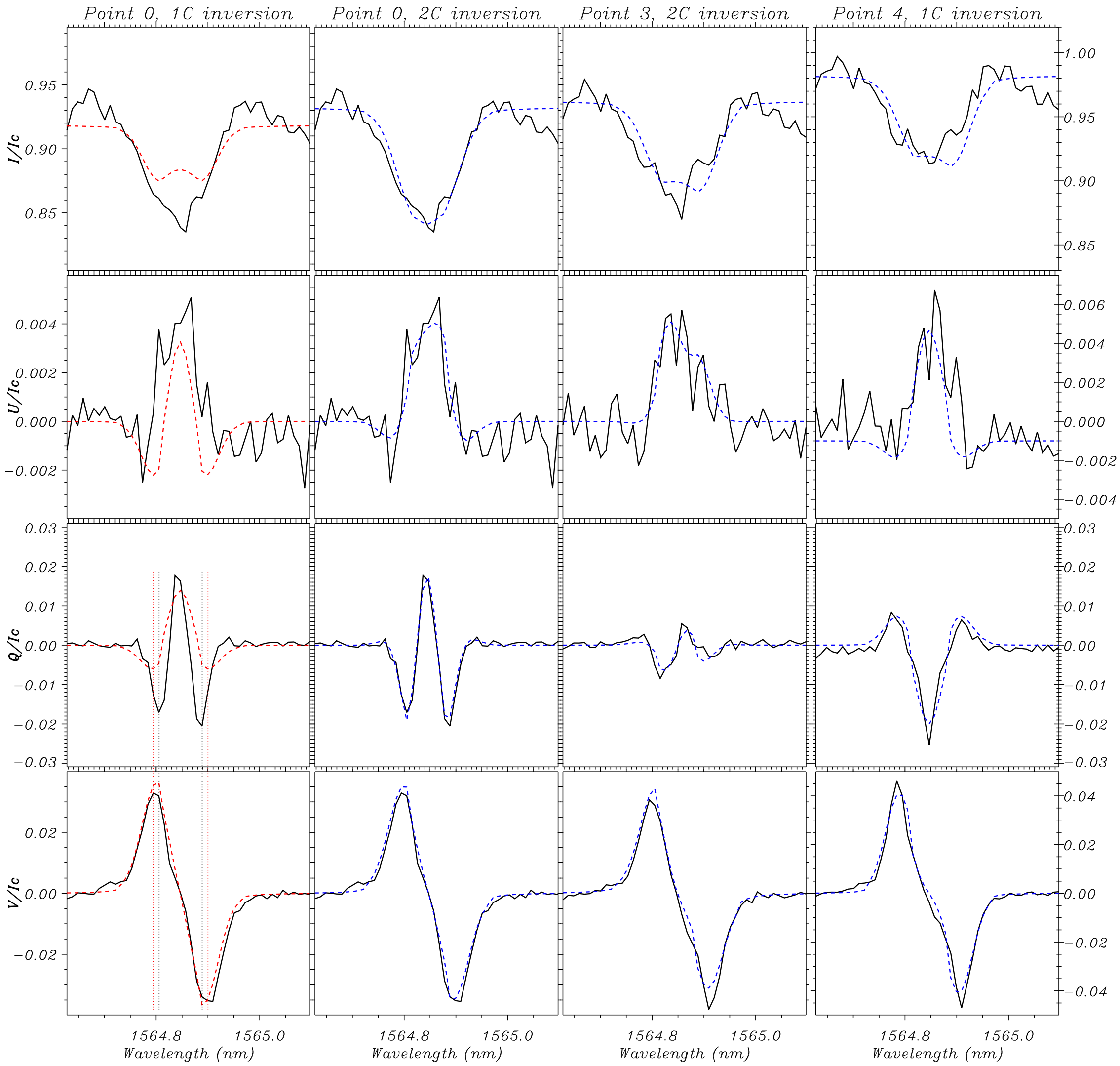

Figure 2.3 The black solid line in each panel represents for observation profile. The red and blue dash line in each panel shows the fitting result. Left column: the one-component fitting for the point in an EFR, with the location of the lobes in Stokes Q and V marked by black and red dot lines. Second column: the 2-components fitting result for the same EFR point. Right two columns are the fitting results for a pixel with the minimum transverse field in the whole EFR and a pixel above a brighten light bridge (LB) overturning convection cell (OCC), respectively. The one-component fitting works well for the LB OCC, while the two-component fitting is required for the EFR.

Source: Yang et al., 2019a

CHAPTER 3

COUNTER-STREAMING MOTIONS IN ACTIVE REGION MAGNETIC LOOPS

3.1 Introduction

The highly magnetized solar upper atmosphere consists of numerous discrete fine-scale magnetic loops, the brightness of which comes from confined plasma of different temperatures. More and more observations and models show that the magnetic loops are far from hydrostatic. Consequently, the motions of plasma along the loops are very important for mass transfer and energy exchange between solar upper atmosphere and lower atmosphere, a key physical process for understanding the problem of coronal heating (Martinez-Sykora et al., 2011[12]). Tremendous advances in this topic have been achieved since space age and high-resolution era (see Aschwanden et al., 2000[13]; Reale et al., 2014[14] and references therein). Generally speaking, I can conclude three kinds of flowing patterns in coronal loops: upward filling (e.g., Sakao et al., 2007[15]; Hara et al., 2008[16]; De Pontieu et al., 2010[17]; He et al., 2010[18]; Tian et al., 2011[19];[20]; Tian et al., 2017[21]), downward draining (e.g., Pneuman et al., 1978[22]; Winebarger et al., 2013[23]) and siphon flows (e.g., Terica et al., 2004[24]). All the results were obtained via measurements of intensity perturbation in images and, especially, Doppler shifts observed by space as well as ground based instruments.

Dynamics of solar filaments (e.g., Pareti et al., 2013[26]) and chromospheric loops (e.g., Ji et al., 2012[27]) have been studied in H_α, He I 10830 Å and EUV observations through the analysis of the paths of absorption features and Doppler shift. Tracing features of time-sequence images and analyzing spectral line profiles reveal two complementary components: plane-of-sky velocity and line-of-sight motion of mass flows. Counter-streaming flows on the Sun were first discovered in filaments

---

[0] Figures and table in this chapter are from Yang et al., 2019[25]

(Zirker et al., 1998[28]; Shen et al., 2015[29]). Because of insufficient spatial resolution, I were unable to separate the superimposed upflows and downflows. With the application of high spatiotemporal resolution observations, researchers are allowed to study structures of low atmospheric with unprecedented level in detail. Zou et al., (2016[30]) analyzed an active region (AR) filament and indicated that the filament is supported by sheared arcades without magnetic dips, and the counter-streaming motion is due to unidirectional flows with alternative directions, while wang et al., (2018[31]) reported the counter-streaming motion of an AR filament above sunspot light bridge is due to physical mass motion along threads. With the advent of large-aperture telescope, pinning down the origin of these chromospheric flows in photosphere will help us to understand not only the nature of counter-streaming flows in chromosphere but also the problem of coronal heating. A previous study has shown the unique role of high-resolution He I 10830 Å imaging with large-aperture solar telescope on ground for precisely locating in the photoshpere the roots of coronal loops (Ji et al., 2012[27]). For AR loops, they found that upward mass and energy flows of ultra-fine channels take their roots at inter-granule lanes. With the same set of data, energy sources originating from inter-granule lanes heating solar upper atmosphere were revealed in solar quiet region (Hong et al., 2017[32]).

With the aim to further investigate the mass and energy flows in coronal loops, I carried out high-resolution spectroscopic imaging in He I 10830 Å for an AR with the 1.6 meter aperture Goode Solar Telescope at Big Bear Solar Observatory (GST, Goode et al., 2010[7]). Simultaneous high-resolution photospheric filtergrams in TiO 7057 Å and chromospheric spectroscopic images in H_α were acquired with GST. In this study, I present the first observations of counter-streaming motions of arcade fibrils in an AR obtained with the He I 10830 Å spectroscopy. Observations and results are given in Sections 3.2 and 3.3, followed by a summary in Section 3.4.

3.2 Observations

On July 18th, 2016, I observed NOAA AR 12569 at N16 E35 (the GST FOV center was at x=-518", y=206", $\mu \equiv \cos\theta = 0.59$) using the NIRIS, VIS and BFI with the aid of AO system. The NIRIS spectroscopic observations were performed at line center and ±0.2, ±0.4, ±0.6, ±0.8 Å of the He I 10830 Å line red component. BFI provides high contrast imaging on the photosphere in the TiO molecular bands in 7057 Åwith a cadence of 15 s. The VIS spectroscopic observations were performed at line center and ±0.4, ±0.8, ±1.0 Å of the H_α line. VIS takes 3 s to acquire a burst of frames and its temporal cadence was set to 30 s (with 9 s delay between each full wavelength scan). The AR was observed from 16:35:51 UT to 22:37:39 UT, while the data between 20:20:55 UT and 20:45:25 UT are selected for this study. Corresponding ultraviolet and extreme ultraviolet observations are provided by AIA on board SDO.

Data sets of different wavelengths were spatially co-aligned for the time of 2016.07.18 20:21 UT by taking HMI/SDO continuum image as reference. Then each data set was reduced by performing alignment to that time, respectively. Utilizing the sub-pixel shift method, I acquired the well-aligned data sets with the alignment accuracy better than 0".03.

3.3 Results

Figure 3.1 provides snapshots of overall observations for AR NOAA 12569. The map for line-of-sight (LOS) magnetic field observed by HMI in panel f gives overall magnetic structure of the AR. The AR contains a negative leading polarity and a positive trailing polarity, between which a bipolar magnetic flux emerged, forming a typical quadrupole magnetic configuration. The field of view (FOV) of GST observations in $H\alpha$ and He I 10830 Å is marked by a black box in the panel, with two sample GST images given in panels a and b. Panels c, d and e show corresponding AIA/SDO observations in 304, 171 and 1600 Å with the same FOV as the black box.

Note that around the trailing sunspot is a diffusive plage area. The plage area for negative polarity of the emerging flux forms a narrow strip (panel e).

In the FOV, roughly two kinds of loops can be seen from space and ground observations: higher fan-like loops prominently in 171 Å images and low-lying arcade loops in 10830 Å. Furthermore, as displayed by the He I 10830 Å image, I can divide the low-lying arcade loops in the FOV into two sets according to their different morphology and connectivity. They have different lengths and curvature, all starting from the trailing polarity (or the diffusive plage region) of the AR. Short and highly curved loops, which is located in upper part of area 2, get into nearby network polarity while long and more straight loops connect with the adjacent polarity of the emerging flux. Notably, in H_α images, the long loops are actually an Arch Filament System (AFS). However, the AFS is not an emerging flux and it has weak EUV emissions at all AIA wavelengths showing that it is slightly heated. Meanwhile, Figure 3.1 panel a gives the counterpart of an AFS in He I 10830 Å. In the coming analysis, I will refer to them as short loops and long loops respectively.

Comparing animations made of blue wing and red wing images of either He I 10830 Å or Hα immediately demonstrate obvious counter-streaming motion patterns in the low-lying arcade loops, teeming in the north-west quarter of Figure 3.1 a (the area in white box, see on-line animations). I constructed flow maps with local correlation tracking (LCT [33]) method to show the observed counter-streaming motions (Figure 3.2).

The mass flow directions inside the loop fibrils are opposite between blue wing and red wing images. The blue wing images give flows behaving a clock-wise (CW) pattern in the region of short loops (deep blue arrows) and a westward pattern in the long loops (light blue arrows). Meanwhile, the red wing images provides a opposite flow pattern (see on-line animation of Figure 3.2). High-resolution images unambiguously show that the counter-streaming flows occur along alternative

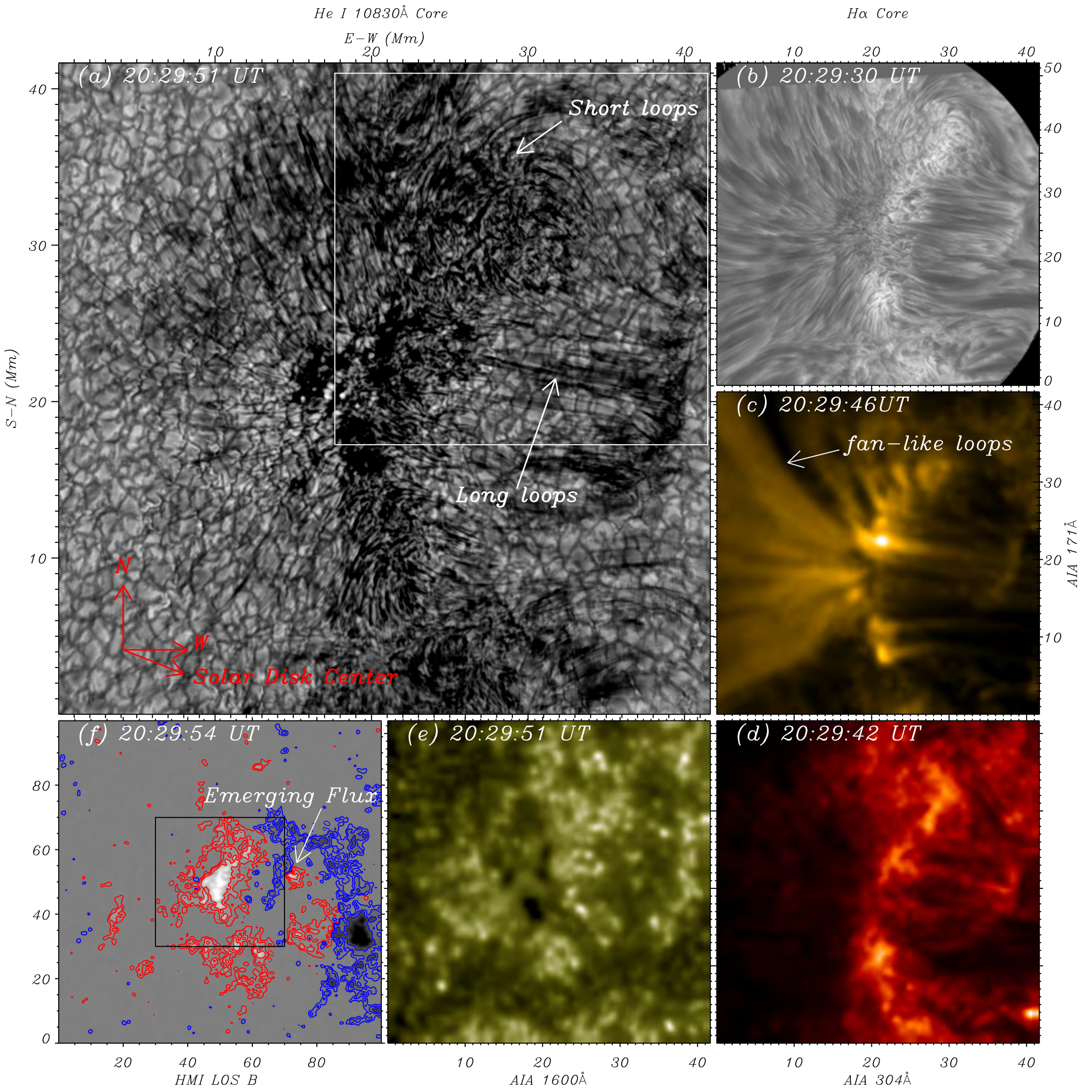

Figure 3.1 Overview of the AR NOAA 12569 observed on 2016 July 18. Panels (a) and (b), with the same FOV, display snapshots of high-resolution spectroheliograms in He I 10830 Å and H_α line center. Simultaneous observations, with the same FOV, by AIA on board SDO are given in panels (c)-(e), which in turn are maps of 171, 304, and 1600 Å. Panel (f) gives the map of line-of-sight magnetic field observed by HMI on board SDO with a larger FOV, in order to give an overall magnetic structure of the AR. Red/blue contours depict the magnetic field in the range of ±30∼300 Gauss.

Source: Yang et al., 2019[25]

loops. In consideration of the AR's location and viewing angle from the Earth, the observations show that the counter-streaming flows might be due to unidirectional mass flows driven by material injection at loop footpoints. I can exclude the possibility of downward streaming at two different sides of the arcade loops, since it can not produce the flow pattern in Figure 3.2.

The mass flow directions inside the loop fibrils are opposite between blue wing and red wing images. The blue wing images give flows behaving a clock-wise (CW) pattern in the region of short loops (deep blue arrows) and a westward pattern in the long loops (light blue arrows). Meanwhile, the red wing images provides a opposite flow pattern (see on-line animation of Figure 3.2). High-resolution images unambiguously show that the counter-streaming flows occur along alternative loops. In consideration of the AR's location and viewing angle from the Earth, the observations show that the counter-streaming flows might be due to unidirectional mass flows driven by material injection at loop footpoints. I can exclude the possibility of downward streaming at two different sides of the arcade loops, since it can not produce the flow pattern in Figure 3.2.

To illustrate the counter-streaming motion patterns, I select two loops as shown in Figure 3.3. Material in long loop 1 flows toward the solar limb (eastward) and contains only red wing absorption signal, while long loop 2 shows an opposite phenomenon: flows westward and contains only blue wing absorption signal. Time-distance diagrams for both loops are given in Figure 3.4 and the apparent flow velocities are found to be 16-25 km s^{-1} for westward motion and around 15 km s^{-1} for eastward. Especially, simultaneous and co-spatial brightenings can be found and they give clear evidence of warm ($\sim 10^5$ K) plasma flows in the same direction, suggesting heating processes.

To confirm the flow patterns inside these loops, I carried out line fitting with a Gaussian profile as an approximation to He I 10830 Å lines. I performed velocity

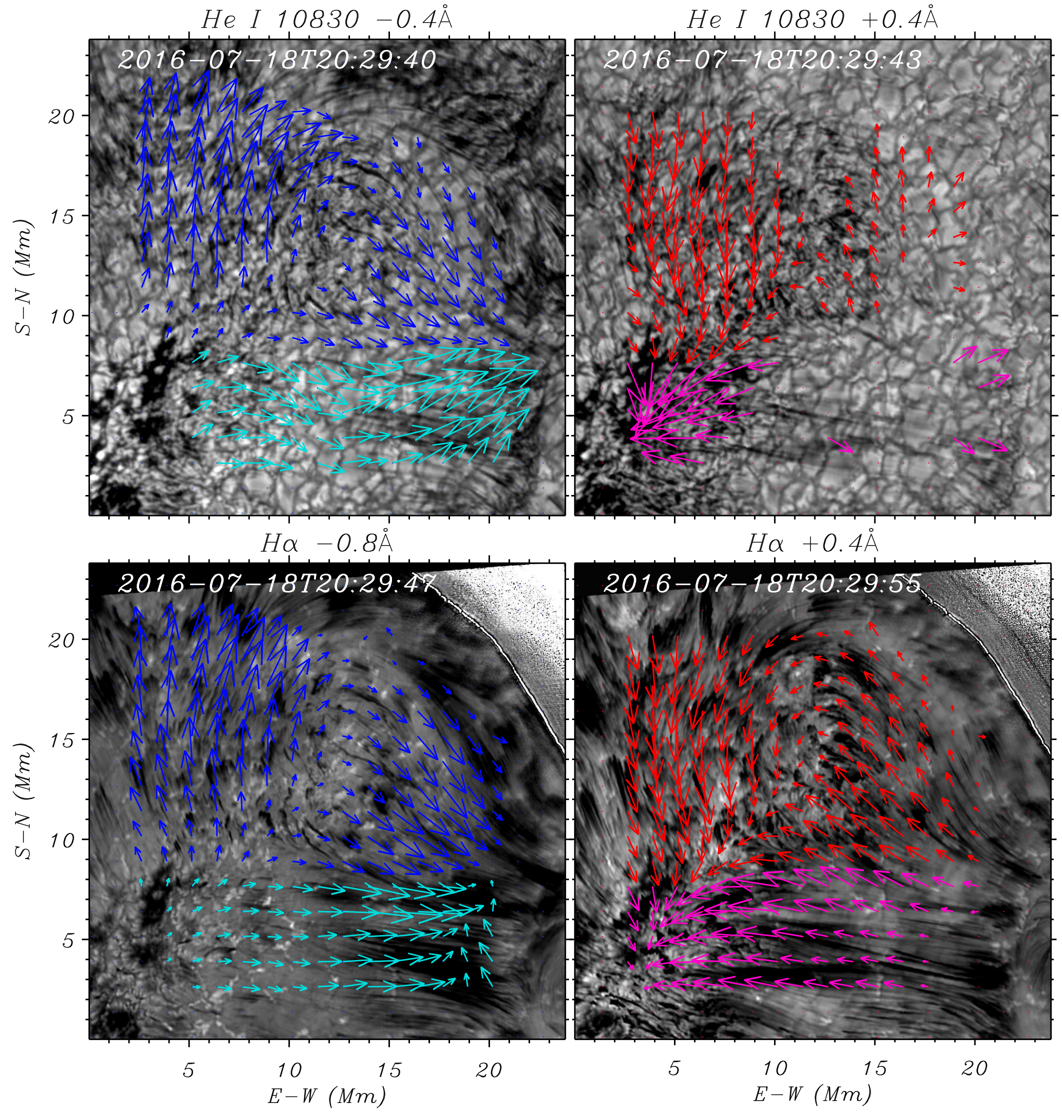

Figure 3.2 Flow maps created with He I 10830 and H_α off-band observations. Top: mass flow maps constructed with He I 10830 ±0.4Å data sets. Bottom: mass flow maps constructed with H_α -0.8 Å and +0.4 Å data sets. The flow maps are derived with LCT method. On-line animation is provided to illustrate the counter-streaming patterns.

Source: Yang et al., 2019[25]

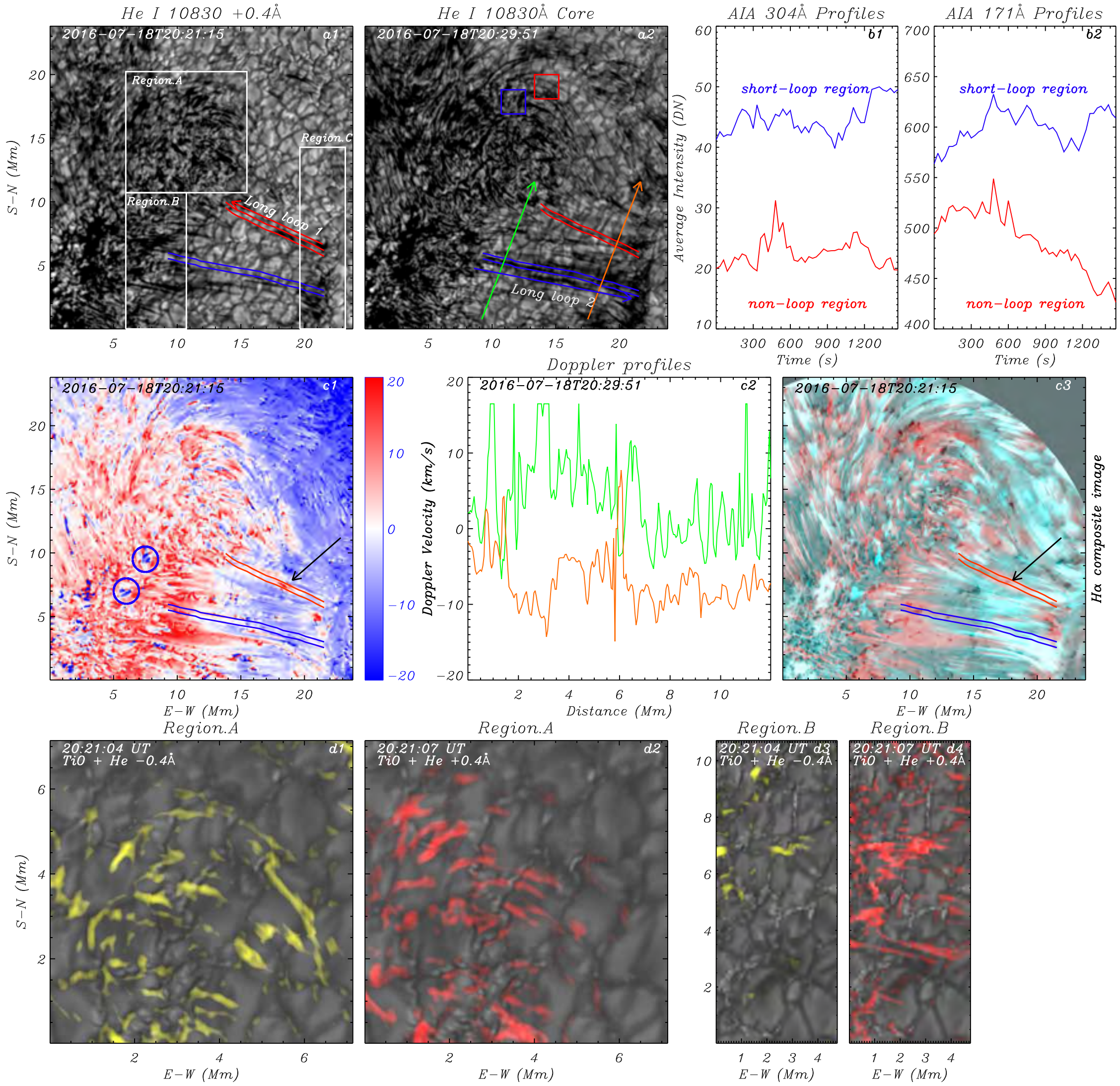

Figure 3.3 Panel a1 and a2: sample He I 10830 Å images overlaid with region information for other panels and Figure 3.4. The double solid lines in different colors mark each selected long loop with nearby arrow indicating the flow directions inside the loop. Panel b1 and b2: blue light curves are for averaged intensities in 171 and 304 Å over the area of short loops and red light curves are over the area of little He I 10830 Å absorption (red box in the top left panel). Doppler velocity maps created with He I 10830 Å spectroscopy data. The black arrows indicate the red-shifted mass flow inside the long loop 1. The blue circles indicate clusters of blue-shifted flows in and around the Region B. Panel c2: Doppler velocity profiles along the two slits (green and orange arrow) in panel a2. The blue circles indicate clusters of blue-shifted flows in Region B. Panel c3: a composite image created with H_α off-band images, showing the different loop positions. Panel d1-d4: Composite images for Region A and B. The background is TiO and the yellow/red color represents the absorption features in He 10830 -0.4 Å and +0.4 Å, respectively.

Source: Yang et al., 2019

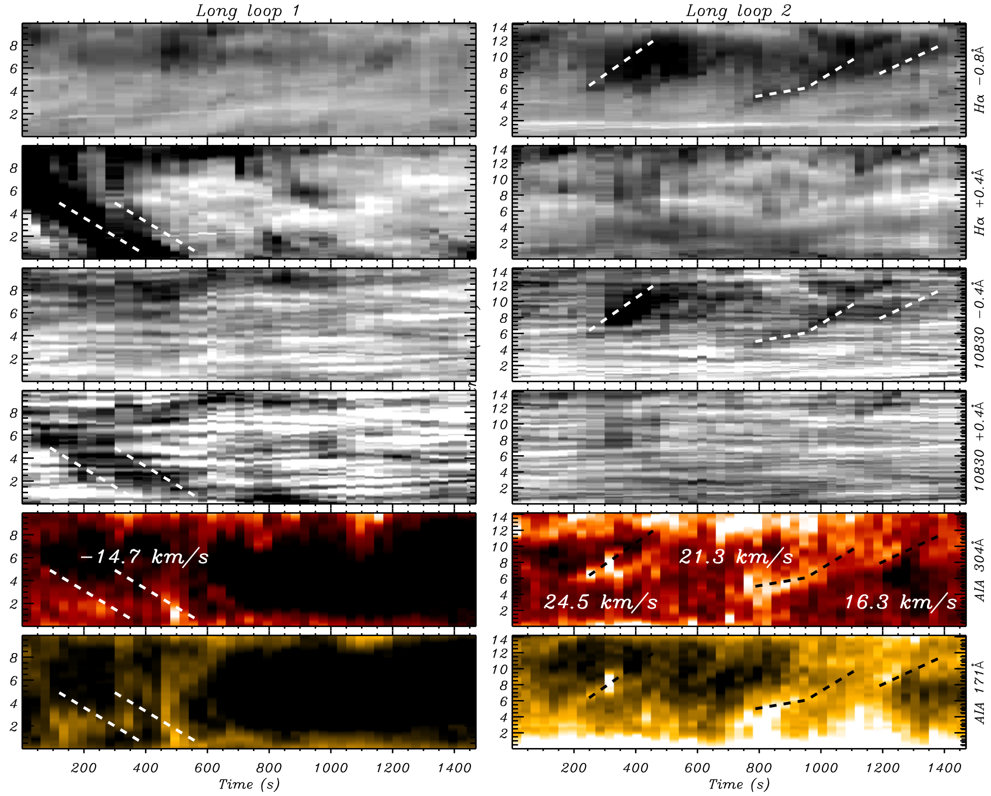

Figure 3.4 The time-distance diagrams in H_α -0.8Å and +0.4Å, He I 10830 ±0.4 Å, AIA 304 and 171 Å for the cutting strips along the long loop 1 and long loop 2. Note that the red-wing absorption features in He I 10830 Å and H_α move eastward along the long loop 1, as indicated by the arrow in the Figure, 3.3 a1. The mass flow inside the long loop 2 is also unidirectional and only contains blue-wing absorption features.

Source: Yang et al., 2019[25]

calibration by setting the line shift averaged over a quiet region near the solar disk center to zero. Doppler velocity is thus obtained from line center shifting and the map is given in panel c1 of Figure 3.3. The same loops (loop 1 and 2) are indicated by the colored double solid lines. The Doppler velocity along the two loops basically confirms conclusions given above. The Doppler velocity can be as high as ± 20 km s^{-1} for red-shifted and blue-shifted components. A composite image made of H_α blue- and red-wing images is given in panel c3 of Figure 3.3. The unidirectional motion in loop 1 and 2 is again confirmed.

For the long loops, absorption features in both He I 10830 Å and H_α in the two footpoint regions are strongly imbalanced. For the left footpoint area (region B in Figure 3.3), I see more absorption features in red wing images. Meanwhile, more absorption features can be seen near the right footpoint area (region C) in blue wing images. I speculate that material for drainage at one side comes from injection at the other side footpoints. As stated in the introduction, material injection is usually hot and, thus, will not be observed with the line from neutral Helium atoms. Material ejected from one footpoint of a strand is cooling down and slowing down when it arrive at the other footpoint. The pattern in Doppler map is reflecting downward drainage. But I see that the drainage is not like the one in a rising AFS.

Furthermore, the dominated line-shift pattern at the two sides contains some oppositely line-shifted component. Panel c2 of Figure 3.3 give the distributions of Doppler velocity along two parallel lines (green and orange lines in panel c2) right across the long loops near the two footpoint regions. Occasional opposite flow directions is evident, especially alone the green line,shows the observation occasional ejection of cool material.

On the other hand, the short loops behave repeating surge-like motions in line core, with slower speed (less than 5 km s^{-1}), and their response in the higher atmosphere is not obvious. The space scale of short loops are normally around 2∼3

Mm, which are only 5∼7 pixels in AIA image. Thus, it is hard to make time-distance diagrams for the short loops. However, the light curve diagrams (Figure 3.3,top right panels) reveal the correspondence between He I 10830 Å absorption features and EUV emissions. I compared the average intensities in a region containing abundant short loops (short-loop region, red box) and a nearby region barely containing He I 10830 absorption (blue box). The EUV emission above the short loop is significantly higher than the region without He I 10830 Å loops.

The He I 10830 Å is optically thin in most part of the solar chromosphere and information from solar photosphere can be obtained from He I 10830 Å spectroheliogram. Thus, alignment between the photospheric and chromospheric images can be carried out at precision of unprecedented level, being up to less than 0.2 arcsec. The advantage has led to a finding that He I 10830 Å blue wing absorption features are rooted in the inter-granule lanes (Ji et al.,2102[27]; Hong et al., 2017[32]). In the similar way, I make composite RGB images by overlapping absorption features of both blue wing and red wing on simultaneous TiO images. Lower left two panels of Figure 3.3 give the results for the region of short loops, where there are abundant 10830 Å absorption features both in blue wing and red wing. I see that the 10830 Å absorption features, either in blue wing or red wing, are mostly located around the area of inter-granule lanes. Only region B is well covered by the FOV of TiO images. Composite images for this area confirmed the above results, i.e., I see that material flows into and out of the area of inter-granule lanes. This shows us that footpoints of magnetic loops are rooted in inter-granule lanes.

From the animations, I can see that absorption features exhibit a kind of periodic behavior, especially in the diffusive plage area. I carried out "Wavelet Analysis for Images" (Torrence et al., 1998[34]) of Hα red and blue wings, with oscillation period maps being given is Figure 3.5. Strong oscillation signature with the period of ∼4 minutes dominates the diffusive plage area where the short loops take their roots, which shows the possible leakage of photospheric p-mode oscillation. However, in the strip plage area, oscillation signature is scarce. Mass flows inside the long loops and co-spatial EUV brightenings show an impulsive nature when they flow out and into footpoint area. Even though some of strands give oscillation periods peaking around 9∼10 minutes, they may actually reflect the time interval between the mass flow tracks obtained in Figure 3.4. I speculate that the flows in the long loops are driven by magnetic reconnection.

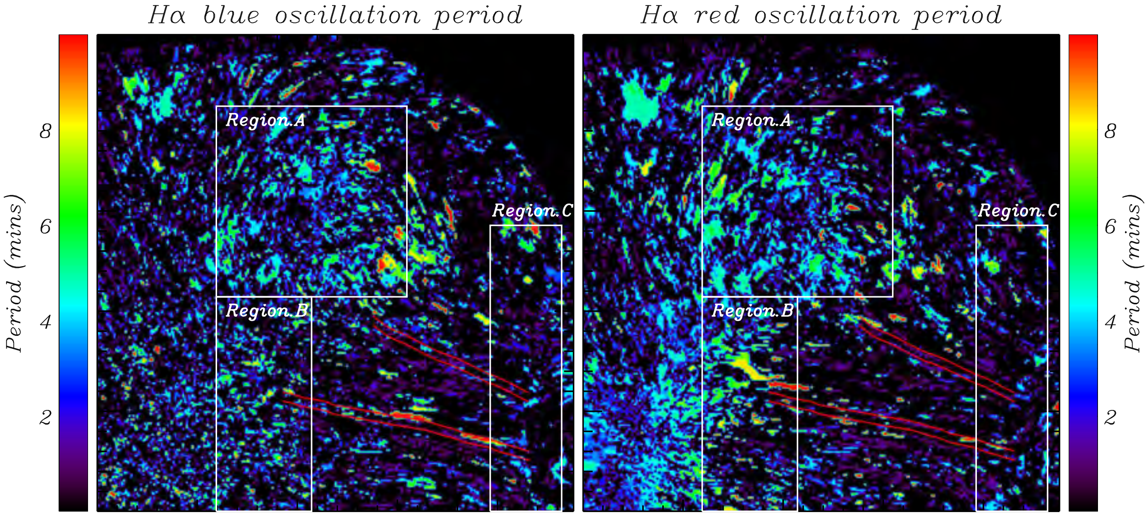

Figure 3.5 Maps for dominating oscillation period obtained from wavelet analysis with H_α line wing images. The region A, B and C are the same to those depicted in Figure 3.3.

Source: Yang et al., 2019[25]

3.4 Summary

With GST at BBSO, I carried out high-resolution spectroscopic imaging in Helium I 10830 Å for upper chromosphere loops, aiming at understanding mass and energy flows in the interface region from below. Studies of AFS based on the He I 10830 Å triplet reported slow upflows of 1.5-20 km s^{-1} in the center of the arches (Solanki et al., 2003[35]; Xu et al., 2010[36]) and downflows of 15-90 km s^{-1} at the footpoints (Lagg et al., 2006[37]; Marique et al., 2018[38]). In this study, blue and red wing images in He I 10830 Å and H_α give apparent side by side counter-streaming flows inside AR arcade loops with an unprecedented high-spatial resolution. Simultaneous auxiliary yet indispensable spectroscopic imaging in H_α and broad band imaging in TiO 7057 Å were obtained. Blue and red wing images in He I 10830 Å and H_α give apparent side by side counter-streaming flows inside AR arcade loops with an unprecedented high-spatial resolution. Considering the location of the AR on the Sun and the loops' low height, the counter-streaming motions actually reflect motions along two opposite directions nearly parallel to the solar surface. My observational findings show that the counter-streaming motions are due to unidirectional mass flows along alternative loop strands.

The magnetic loops where counter-streaming flows connect two plage areas (network regions) formed around trailing polarity of the AR and a nearby emerging polarity. In spectroscopic images in He I 10830 Å, the flows take the form of moving absorption features. A precise alignment between 10830 Å images and corresponding photospheric images taken in TiO 7057 Å allow us to find that plasma flows are pumped up from and drained down to the inter-granule lanes. While the phenomena of plasma flowing out of inter-granule lanes along ultra-fine channels has been reported (Ji et al., 2012[27]), the results of this dissertation not only confirms the results but also show that plasma flows into inter-granule lanes along ultra-fine channels. This indicates that each strand of magnetic loops is ultimately rooted in inter-granule lanes.

The moving absorption features in He I 10830 Å along long distances (long loops in this dissertation) are apparently accompanied with co-spatial EUV emissions in AIA 304 Å and 171 Å images, and the moving features are impulsive. No co-spatial

EUV emissions are found during short-range surge-like ejections of absorption features (short loops in this dissertation). While, average EUV emission over these short absorption features is much higher than that of rest of regions. Therefore, the results confirms that heating sources of TR are located in inter-granule lanes.

Wavelet analysis shows that the oscillation power inside these short loops peaks around 4 minutes, indicating possible role of p-mode in pumping out the short-range plasma ejections. However, there is no evidence for that the unidirectional mass flows inside the long loops are also modulated by p-modes. I speculate that magnetic magnetic reconnection or cancellation may play a major role in powering the long range flows. Further study with high resolution magnetograms may reveal the role fine-scale magnetic network activities in powering the counter-streaming mass flows.

CHAPTER 4

LIGHT BRIDGE BRIGHTENING AND PLASMA EJECTION DRIVEN BY A MAGNETIC FLUX EMERGENCE EVENT

4.1 Introduction

Light bridges (LBs) are elongated, bright, granular structures that divide the umbra of a sunspot into two or more umbral regions with the same or the opposite magnetic polarities (Muller 1979[39], Zirin et al., 1990[40], Sobotka et al., 1994[41]). The magnetic field in LBs is weaker that in the sunspot umbra, and the convective motions of plasma inside LBs are not totally inhibited (e.g., Lagg et at., 2014[42]). Simulation results indicate that field-free plasma from the underlying convection zone contains more than enough internal energy to penetrate into the umbra along openings in the magnetic field and it can reach the solar surface manifesting itself as LBs of various thickness and length (Schuessler et al., 2006[43]). LBs can be categorized as faint, strong, or granular depending on their brightness, size and the internal structure. The magnetic field of all types of LBs show a similar pattern of increasing field strength with height, and a cusp-like configuration (Jurcak et al.2006[44]). Recent observations showed that granular LBs are quite similar to quiet Sun granulation (Lagg et al., 2014[42]).

Solar jets, characterized as impulsive evolution of well-collimated bright or dark structures that extend along a particular direction, occur commonly in the upper solar atmosphere. The observed spatial scale of jet-like events ranges from the limits of telescope resolution to hundreds of Mm and they can be detected in all available spectral ranges (e.g., Pariat et al., 2015[46]; Pariat et al., 2016[47]). Kurokawa (1988[48]) and Kurokawa & Kawai(1993[49]) reported that Hα jets often appear at the earliest stage of magnetic flux emergence and could continue for many hours.

---

[0] Figures and table in this chapter are from Yang et al., 2019a[45]

They suggested that the essential mechanism for producing these Hα jets is likely to be magnetic reconnection between a newly emerging flux and a pre-existing magnetic field. Yokoyama & Shibata (1995[50]) further showed in their numerical simulation that such reconnection might indeed produce Hα surges in emerging flux regions.

Chromospheric jets are commonly seen above LBs. Ejected plasma is normally observed rooted between one side of a LB and the adjacent umbra, and moving upward along the magnetic field above the LB (Asai et al., 2001[51]; Louis et al, .2014[52]). These authors stated that the jets suggest the emergence of a bipolar magnetic flux or the presence of opposite polarity field. Bharti et al., (2007[53]) reported evidence of opposite polarity fields emerging in a LB followed by a co-spatial plasma ejection event. Louis et al., (2015[54]) reported observational evidence of a small-scale Ω-loop that emerged in a LB and led to a chromospheric brightening. Recently, Toriumi et al., (2015a[55],b[56]), showed that chromospheric brightenings and dark surges in a LB are a consequence of magneto-convective evolution within the LB interacting with the surrounding magnetic fields. Tian et al., (2018[57]) categorized surge-like activities above the LBs into oscillation-driven surges and reconnection-triggered jets.

An alternative explanation of the LB jets is that they are the result of shocks generated by magnetic reconnection or photospheric waves. Yurchyshyn et al., (2014[58]) reported detailed observations of umbral jets-like structures and demonstrated they might be driven by upward propagating shocks generated by photospheric oscillations. Bharti et al., (2015[59]) and Yang et al., (2015[60]) recently reported on a bright front ahead of a system of Hα jets above LB that were coherently oscillating in vertical direction. Bharti et al., (2015[59]) further noted that magnetic reconnection fails to fully explain the coordinated behavior of these oscillating jets, while Yang et al., (2015[60]) interpreted the oscillating light wall, which is the counterpart of the LB in the chromosphere, as leakage of p-mode waves from below the photosphere. These oscillations were also found to be enhanced or suppressed by external disturbances such as flares (Hou et al., 2016[61]; Yang et al., 2016[62]). Song et al., (2017[63]) observed shock waves, generated by magnetic reconnection between an emerging flux inside a LB and the adjacent umbral magnetic field, that were driving arcsecond-scale plasma ejections above a LB. Zhang et al., (2017[64]) reported that surge-like oscillations above LBs resulted from p-mode shock waves transmitted from the photosphere.

Penumbral microjets (PJs) are fine-scale jet-like features ejected in the chromosphere above a penumbra and they could be triggered in the same way as the LB jets. PJs were first reported by Katsukawa [65] using data from the Solar Optical Telescope/Filtergraph (SOT/FG[66]) onboard the Hinode satellite (Kosugi et al., 2007[67]). Magnetohydrodynamic (MHD) simulations support the idea that reconnection drives these events by inducing strong plasma outflows along horizontal flux tubes (Sakai et al., 2008[68]) or by assuming the horizontal field in a twisted flux tube (Magara et al., 2010[69]). The convective up-flows continuously transport magnetic fields to the surface layers where they later interact with the existing large-scale vertical umbral fields (Toriumi et al., 2015a[55],b[56]). Tiwari et al.(2016[70]) classified PJs as normal or large/tail jets, depending on whether or not they show strong signatures in the transition region (TR). These authors presented a PJs formation mechanism using a modified picture of magnetic reconnection in an uncombed penumbra with a mix of horizontal and inclined fields. Similar to the LB jets, another explanation (Ryutova et al., 2008 [71]) proposes that shocks generated by reconnection between neighboring penumbral filaments can produce PJs and an observational support to this interpretation is given in Reardon et al., (2013[72]).

The above mentioned studies of LB jets often lacked magnetic field measurements that would describe the dynamics of the underlying magnetic fields. In this study I focus on the evolution of a magnetic flux emergence (MFE) event that occurred in a granular LB and caused enhanced brightness of photospheric overturning convection cell (OCC) at that location. A co-spatial and co-temporal chromospheric plasma ejection event was observed in association with the MFE event accompanied by a chromospheric brightening at its origin. For this case study, I utilized high-resolution photospheric and chromospheric images as well as 1564.85 nm vector magnetic field data acquired with the GST. The GST data set was complemented by EUV data taken by the AIA and continuum intensity/vector magnetic field data taken by the HMI onboard the SDO.

4.2 Observations

On February 9th, 2016, I observed NOAA AR 12494 at S12 W56 (center of the GST field of view (FOV) was at x=690", y=-106", $\mu \equiv \cos\theta = 0.69$) using the BFI TiO 705.7 nm, the VIS Hα 656.3 nm and the NIRIS Fe I 1564.85 nm full-Stokes profiles with the aid of the AO system installed on GST. Figure 4.1 presents a part of 19:22:29 UT TiO image, showing the observed AR.

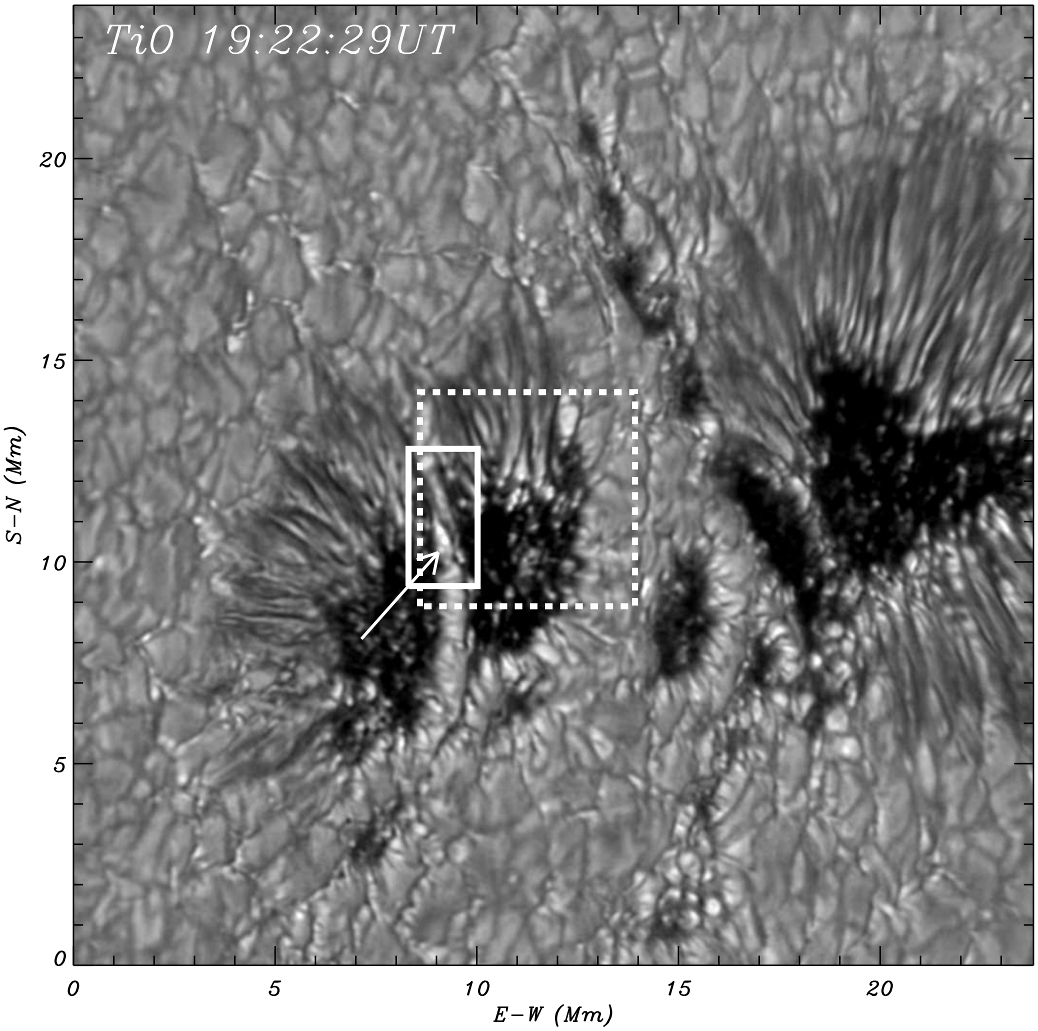

Figure 4.1 Part of TiO white light image (705.7 nm), observed by BFI/GST at 19:22:29 UT. The white arrow indicates brightness enhancement that occurred above an OCC inside the LB. The solid line box, corresponding to a MFE event, shares the same FOV with Figure 4.4. The dash line box marks the FOV of Figure 4.5.

Source: Yang et al., 2019a[45]

In this study, the VIS spectroscopy observations were performed at Hα line center, ±0.04, and ±0.08 nm. The total temporal cadence for BFI and VIS were set before 19:01 UT to 30s and 40 s accordingly, then the cadence was decreased to 15 s and 25 s as seeing conditions improve. NIRIS samples 16 phase angles at each of more than 60 line positions (40 for the Fe I 1564.8 nm) with a cadence of 126 s to perform one full spectropolarimetric measurement including the full-Stokes I, Q, U, V. Selected Stokes profiles are shown in Figure 4.2.

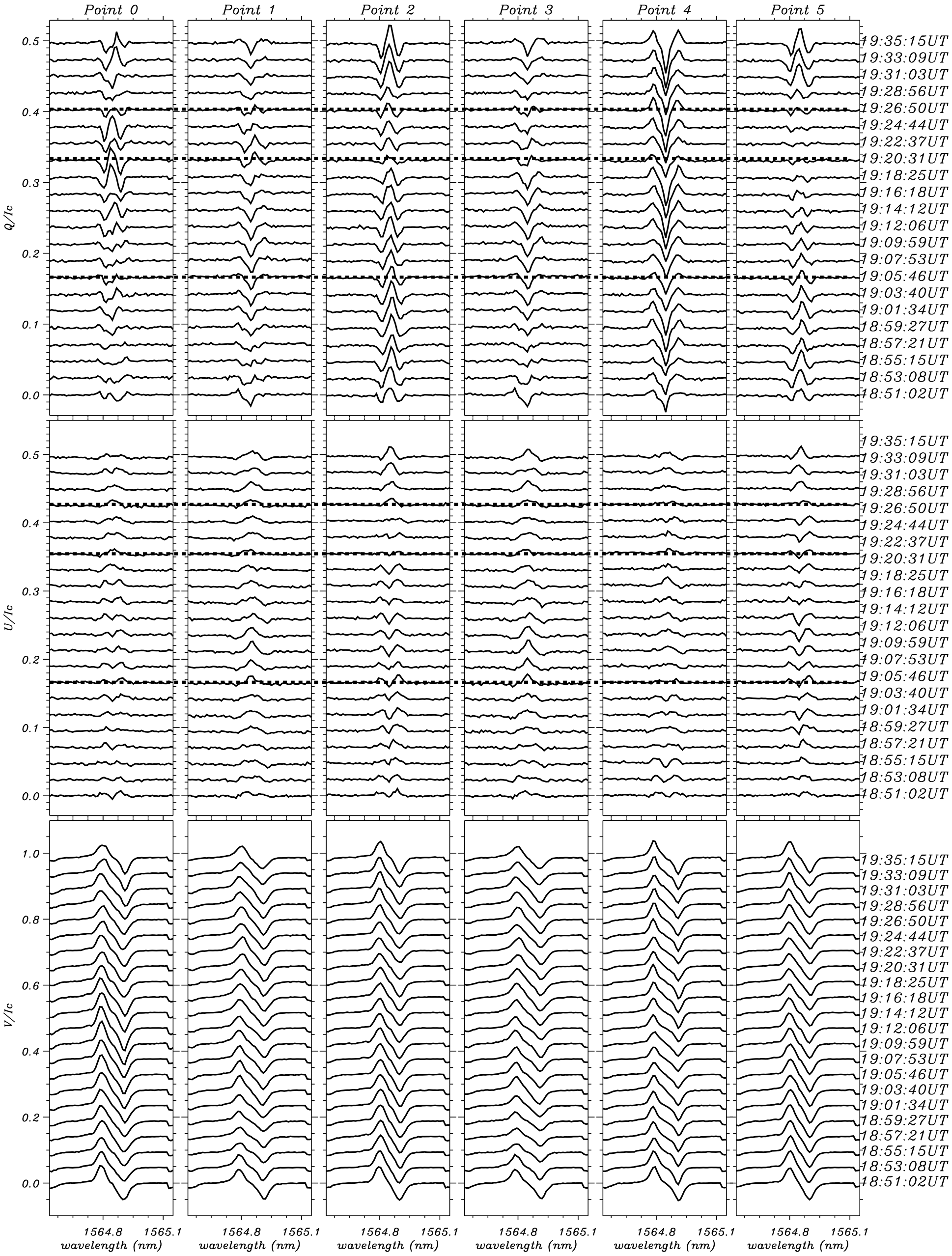

Figure 4.2 Normalized Stokes Q/U/V profiles at each point mentioned in Figure 4.3 during the MFE. Dot lines in top panels (Stokes Q) and middle panels (Stokes U) mark the time when the emerging transverse magnetic field structure appeared, peaked and destructed.

Source: Yang et al., 2019a[45]

4.3 Data Reduction and Analysis

The AR was observed from 17:55:20 UT to 22:57:42 UT, while the data between 18:51:02 UT and 19:35:15 UT were selected for this study. Data sets of different wavelengths were spatially co-aligned for the time of 2016.02.09 18:51 UT by taking HMI/SDO continuum image as reference.

We applied two inversion methods to the NIRIS Stokes profiles. The Milne-Eddington (ME) inversion code used in this study was developed by J. Chae, and its early version was applied to the Hinode/SP data (Chae & Park 2009[10]). An inverted data set includes nine parameters among which are the total magnetic field flux density, the inclination and azimuth angles, and the Doppler shift. This code uses a simplified model of solar atmosphere and performs very fast inversion, which is desirable when inverting a large data set. I applied it here to a series of spectropolarimetric line profiles to analyze the temporal evolution of the MFE event. To better understand the height dependence of the magnetic field and to obtain reliable thermal information, a more complex inversion should be used. For this purpose, I applied a Stokes inversion method based on Response functions (SIR) developed by CoBo (1992[11]). A simple SIR inversion model with one-component (1C) gradient magnetic field configuration – 3 nodes for perturbing temperature, linearly evolving magnetic strength, line of sight (LOS) velocity, inclination, azimuth and no straylight correction applied – works well for the umbra, the LB and the most part of the penumbra in this region. The inversion results contain data for different solar atmosphere heights ranging from Logτ = 1.4 to Logτ = -4. A comparison of the inversion result between the two methods are presented in Figure 4.3. I resolved the 180-degrees ambiguity by using HMI/SDO ambiguity-resolved vector magnetic field as reference and applying the acute angle approach, i.e., azimuth was assigned in the direction that was making smallest angle with the corresponding HMI azimuth.

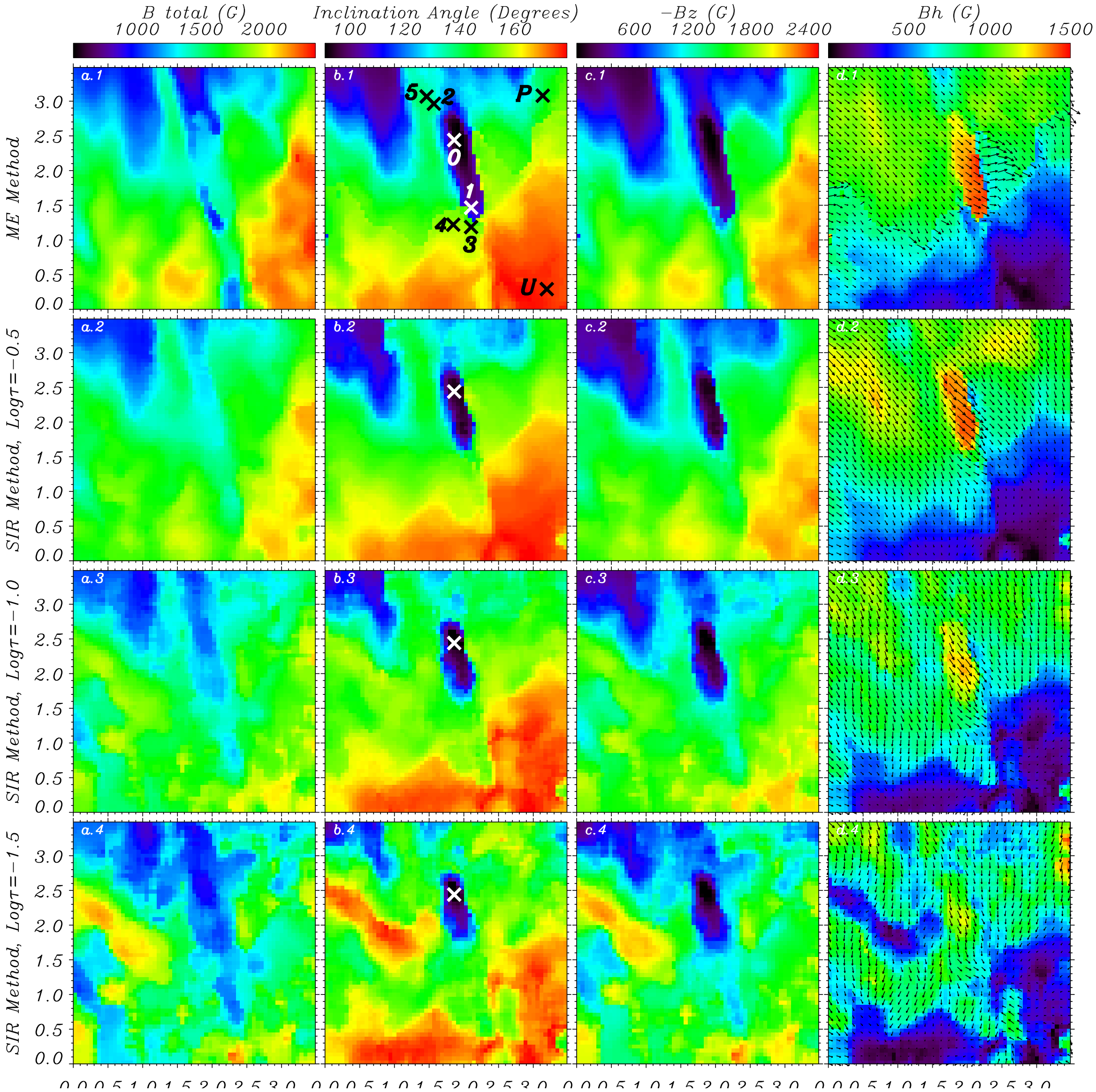

Figure 4.3 A comparison of different Stokes inversion methods applied to the NIRIS 19:20:31 UT Stokes profiles. The first row is the inversion results from ME method and the others are from SIR method (Logτ = -0.5/ -1.0/ -1.5 or τ = 0.316/ 0.1/ 0.0316). Column a shows total magnetic field and the images in columns b, c and d represent the magnetic inclination angle, vertical and horizontal magnetic flux density in the heliographic coordinates, respectively. The four images in each column are drawn with the same dynamic range. Point 0 with white "cross" symbol in b.1 marks the only pixel that contains the opposite polarity in the ME inversion. Point U and P with black "cross" symbol represent selected umbral and penumbral pixel. The magnetic field orientation vectors (black arrows) in the horizontal plane are overplotted on column d images.

Source: Yang et al., 2019a[45]

After inspecting the SIR inversion results at several selected pixels, I found that the 1C magnetic field model did not satisfactory fit the observed profiles in the flux emergence region. Some of the fitting samples are provided in Figure 2.3. The last column of Figure 2.3 shows that 1C inversions work well for the brightening at the LB OCC region (point 4) and only one strong vertical magnetic field component may be used to invert the data at this pixel. The left column displays the observed Stokes profiles and the 1C inversions at point 0. The thing to notice is that the lobes in the observed Q profile are closer together than those in the V profile and they have smaller width. As for the 1C inversions, the lobes in the inverted Q profile are simply too broad to fit the observed ones, but they match the width of Stokes V lobes. The reason why the 1C inversions failed to match the observations is that at this pixel I probably have a mix of two magnetic components. The one that is more horizontal and produces the Stokes Q signal has a lower field strength, while most of the contribution into the Stokes V comes from a more vertical component This is why the lobes in Q have a lower width, while Stokes V lobes are more separated.

With an ultra-strong gradient (nodes for B/gamma/phi ≥ 2), I can "emulate" those two different components in one stratification, however the fields have to change their inclination by about 90 degrees within the range Logτ 0 to -2, and their fields flux density has also to change rapidly within that narrow spatial range. In this case, a two-components (2C) magnetic field model is needed for those pixels that display this kind of Stokes profiles (Figure 2.3, second column).

We then applied a 2C inversion atmospheric model to selected pixels of interest, and assigned 2 nodes for temperature with a constant magnetic field and LOS velocity,. For point 0, the 2C inversion resolved a slightly inclined strong vertical magnetic field component (which dominates the penumbra region) and a weak horizontal magnetic field component (which is common in the flux emergence region). Similarly, for point 3 located at the magnetic minimum region, I found an opposite polarity magnetic field component that is mixed with the background penumbra magnetic field.

The 1C and 2C inverted and de-projected magnetic flux density and inclination angles for the selected pixels are listed in Table 4.1.

4.4 Result

4.4.1 Temporal Evolution of the MFE

Figure 4.1 presents a photospheric image of the MFE event observed in the AR NOAA 12494. A significant brightness enhancement occurred at the top of the LB overturning convection cell (OCC). A regular granular structure of the LB was replaced by one elongated OCC, with one end point moving along the LB toward the sunspot center (inner endpoint, white arrow) and the other one radially outward (outer endpoint). In the area marked by a dashed line, a plasma ejection event was triggered and a brightening at its footpoint was observed in the Hα image between the LB OCC and one of the sunspot umbrae.

Figure 4.4 shows the temporal evolution of the flux emergence event as seen in various wavelengths. Each panel displays the same FOV outlined by the solid line in Figure 4.1. The panels in the upper row present photospheric TiO images. As the OCC (marked with the white line) expanded to reach approximately 2 Mm in length, two enhanced intensity TiO patches developed near the endpoints of the expanding OCC (black contours in the image of 19:22:37 UT). The green contours, obtained by creating running difference images, represent 25% brightness enhancement relative to the running background obtained by averaging five consecutive TiO images acquired during a 75 s interval prior to 19:21:44 UT. The TiO brightenings first appeared at 19:21:44 UT and remained noticeable until 19:27:14 UT. The difference between the 19:22:29 UT image and the background showed a significant central brightness enhancement and a noticeable brightening at lower right. Inspection of unprocessed raw TiO images confirmed them to be real enhancements and not intensity fluctuations introduced by data reconstruction.

Maps of the total linear polarization (L=$\int \sqrt{Q^2 + U^2} d\lambda$) and Doppler velocity obtained from the NIRIS spectropolarimetry data are displayed in the second and third rows of Figure 4.4. According to the data, the emergence lasted for about 30 minutes. It began at a location that already had a lower magnetic field flux density compared to the surroundings. At 18:53 UT NIRIS data showed no magnetic signatures of this new flux and only a strong upflow of about 1.5 km/s at the site of future emergence was distinct in the data. By 19:10 UT the upflow subsided and the transverse magnetic field showed up at the location of the original upflow. NIRIS Doppler maps showed two LOS velocity patches that have developed in association with the flux emergence. The inner endpoint was associated with a compact (<0".3) downflow with velocities exceeding 1.5 km/s at their peak time (19:20 UT), while the outer endpoint only showed very weak downflows that turned into equally weak upflows (approx. 0.1 km/s) by 19:20 UT.

At the same time, the LOS magnetic field began to gradually increase at the inner endpoint, while the LOS field at the outer endpoint remained much lower. By 19:20 UT the transverse flux has peaked, while the LOS field showed strong asymmetry at both endpoints. However, no opposite polarity features were detected at that time, or any other time during the emergence. Compared to the pre-emergence state, the LOS magnetic flux density at the inner (umbra) endpoint has increased from approx 500 G level to over 1000 G, while at the outer endpoint the increase was much smaller and the resulting field did not exceed 900 G level.

Figure 4.5 displays off-band Hα -0.08 nm images, in the same time series as of Figure 4.4, showing a portion of a small sunspot with two umbral cores separated by a thin LB seen in these panels along their left edge. At approximately 19:17 UT, a compact chromospheric brightening developed at the very edge of the umbra

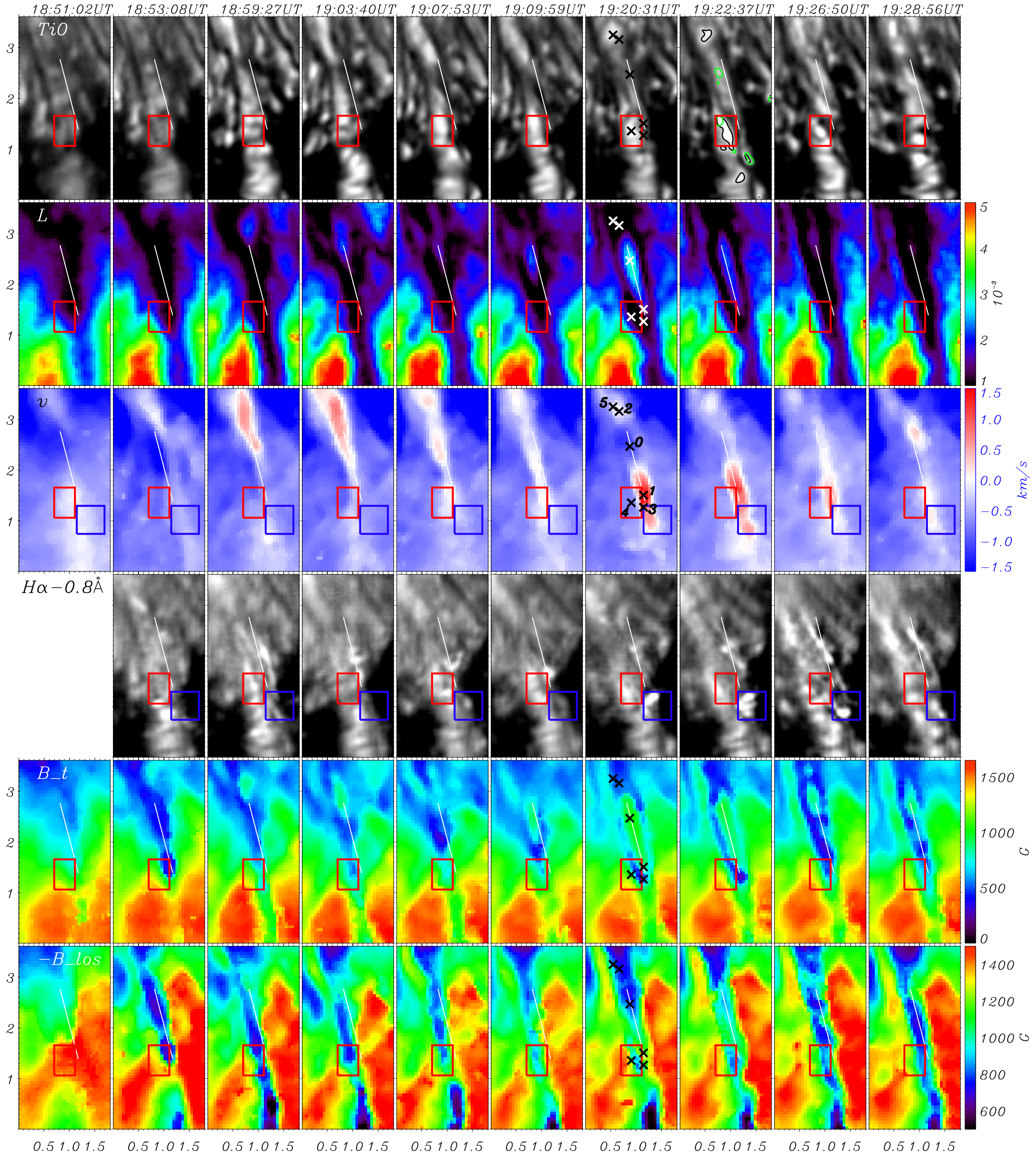

Figure 4.4 Overview of GST dataset. The panels present, from top to bottom 2D maps, evolution of TiO Photosphere, total linear polarization, LOS Doppler velocity and Hα off-band, transversal and longitudinal magnetic field flux density. Green contours presented in the TiO image at 19:22:37 UT represent 25% brightness enhancement to the running background. The black contour indicates 1.3 times of the average intensity of the granulations in the nearby quiet Sun region. The white lines indicate the axis of the emerged flux. Numbers and "X" symbols mark five points for which magnetic flux time profiles and Stokes parameters will be analyzed (maximum inclination (0), Doppler endpoints (1 and 2), transverse field minimum (3), and TiO brightenings (4 and 5).

Source: Yang et al., 2019a[45]

next to the LB (outlined by the white box). Before the brightening onset, several nearly collimated jets were ejected in the direction of the umbra (white arrow) from that compact location forming a narrow fan-line structure. The tips of the jets were aligned and moved together forming a well-defined front. The jets did not exhibit any translational or swaying side-ward motions and increase of their apparent length was the only distinct evolutionary parameter.

In Figure 4.6 I plot orientations of the transverse field along the spine of the emerging structure. The orientation of the transverse field changed during the emergence process. A small differential angle between the transverse field and the longer axis of the magnetic structure (white line) was observed until the maximum of the loop structure and the differential angle has decreased after that time, so that the transverse fields became nearly parallel with the longer axis of the emerging field. I emphasize that the NIRIS magnetic field data were not resolved for 180 degree ambiguity here, so I use the term “orientation angle” rather than the “field azimuth”. The Bx-By plots (left panel) show that the transverse field began to gradually rotate in the CCW direction at about 19:07 UT and the emerging structure can be seen between pixels 9 and 23 as a series of vertically oriented line segments. As emergence proceeded the transverse structure expanded toward the umbra. It is interesting to note that at the onset of the emergence the fields in front of the moving inner endpoint (i.e., between pixels 1 – 7 at 19:07 UT) appear to change their orientation from nearly parallel to the longer axis to nearly orthogonal. It can be speculated that these sudden changes may have resulted from the snow-plow effect where the emerging field was intruding into the LB compressing and folding pre-existing magnetic structures ahead of it. The field inclination has not changed drastically during the event although at the time when the emergent flux reached its maximal length. After the peak of the event the transverse field continued to rotate in the CCW direction so that the differential angle changed its sign. The right panel in Figure 4.6 shows time profiles of

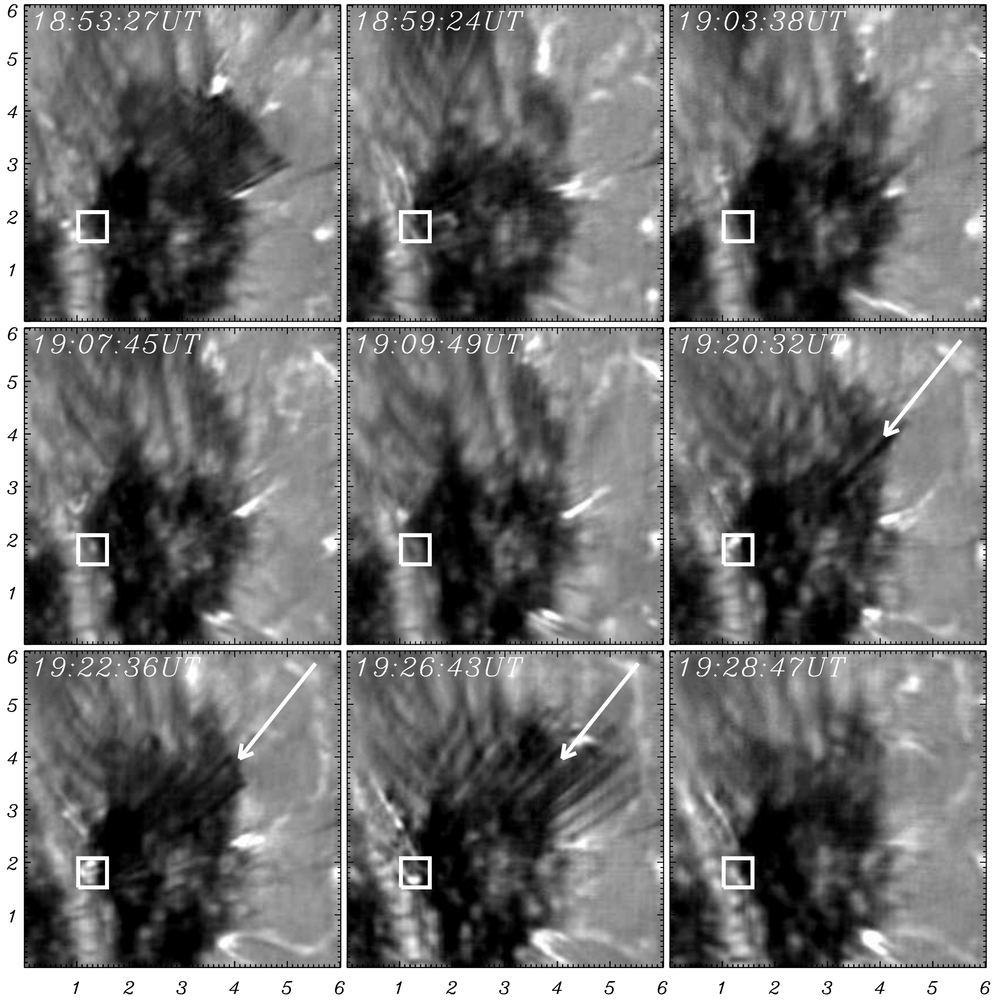

Figure 4.5 Chromospheric jetting activities observed with off-band Hα -0.08 nm. Time sequence of the displayed images is same to Figure 4.4. FOV of each panel is indicated by the white dashed line box in Figure 4.1. A band of narrow straight jets (white arrow) rooted at a compact brightening (white box, indicating the same area of the blue box in Figure 4.4), located at the edge of the LB and the sunspot umbra. The brightening first appeared at 19:17 UT and disappeared at 19:26 UT and was associated with the jet during the entire existence.

Source: Yang et al., 2019a[45]

the differential angle at pixels 2, 7, 12, 17, and 22. Pixel 2 is co-spatial with the inner (umbral side) endpoint of the structure and the differential angle rapidly decreased as new fields appeared at that location. Pixels 12, 17, and 22 were situated near the mid-section of the emerging fields and the corresponding profiles show gradual change of differential angle from 50° to nearly -50°.

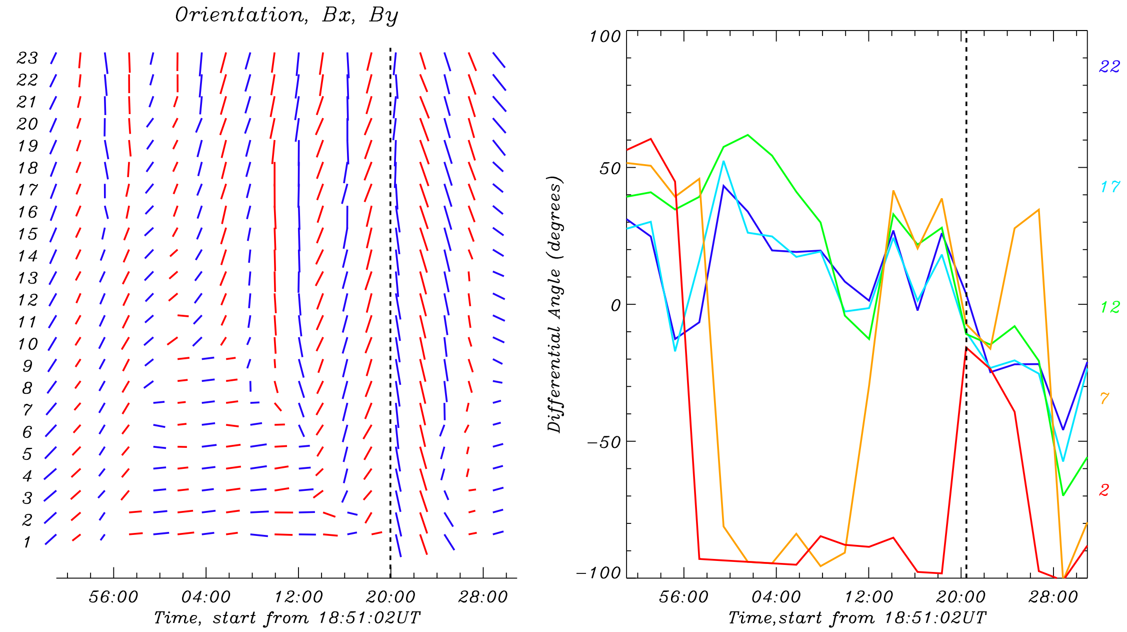

Figure 4.6 Plot of NIRIS data slice along the whitle line on the emerging structure. A total of 23 pixels are selected along the white line starting from the inner endpoint (pixel 1, umbral side) to the outer endpoint (pixel 23, penumbral side). Left: transverse field evolution. Right: differential angle (difference between the direction of the white line and the azimuth angle of pixels along the white line) profiles plotted for pixels 2, 7, 12, 17 and 22(red/yellow/green/light blue/blue). The black dash line in each panel marks the peak time of the MFE.

Although the NIRIS data did not reveal any significant features of opposite polarity associated with the emergence, the magnetic field time profiles (Figure 4.7) suggest a bipolar flux emergence process. During the emergence, the magnetic field became enhanced at the inner endpoint and weakened at the outer magnetic endpoint, which may indicate the emergence of a bipolar structure with a negative (sunspot) polarity at the inner endpoint and a positive polarity at the outer (penumbral side) endpoint. Both outer and inner TiO brightenings occurred during the magnetic field enhancement phase and are located close to the high magnetic gradient region. I speculate that the endpoints of the emerging structure displaced granulation ahead of them, which may lead to increased apparent brightness due to plasma compression. I would like to further note that the observed sequence of events and the rotation of the transverse fields are consistent with the emergence of a horizontal current carrying loop with a positive(negative) field endpoint located in the penumbra(umbra) of the sunspot and right handed twist.

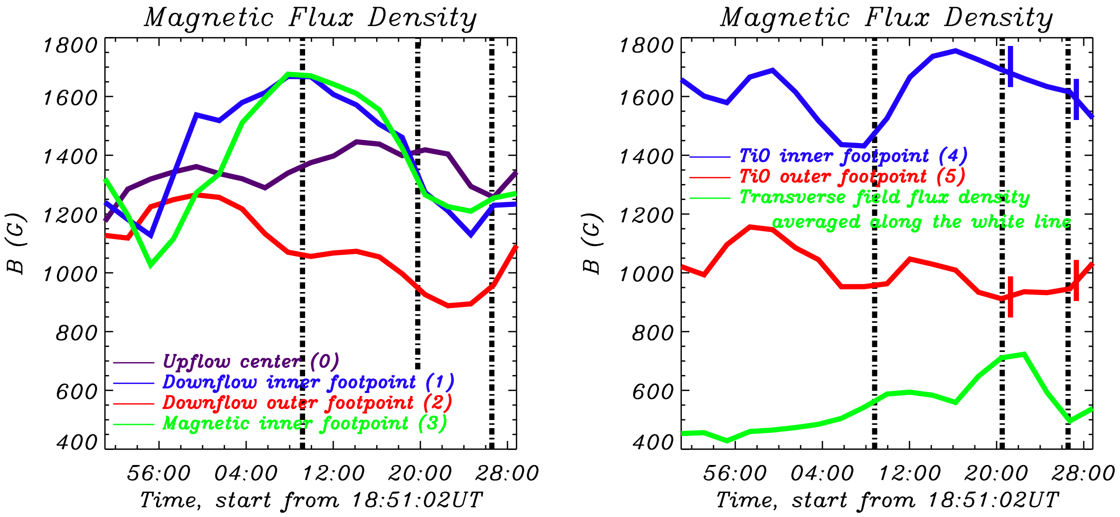

Figure 4.7 Time profiles of magnetic field flux density. X-axis starts at 18:53:08 UT, when a strong blue shift first appeared at the region. Three vertical dot-dashed lines mark the time of first appearance of the transverse field structure (19:09:59 UT), its peak time (19:20:31 UT), and the disappearance time (19:26:50 UT). Left: Time Profiles of the total magnetic field flux density at point 0, 1, 2, and 3 (purple/blue/red/green). Right: The same but for point 4 and 5 (blue/red) as well the profile of the transverse magnetic flux density averaged along the white line (green). The TiO LB OCC brightening started at 19:21:44 UT and ended at 19:27:14 UT and those times are marked with the short vertical bars.

Source: Yang et al., 2019a[45]

Finally, I inspected the relevant NIRIS Stokes profiles to the selected point 0 – 5 (Figure 4.2). The Stokes V profiles were stable during the emergence and did not show any significant variations. (Figure 4.2, bottom panels). The most prominent variations were observed in Stokes Q profiles (upper panels) at point 0, 1 and 2 (Doppler upflows and downflows) during the emergence (between dashed lines), which matches well with the changes in the orientation of the transverse field at those endpoints. I therefore conclude that the absence of the opposite polarity is not a consequence of failing data inversion but is rather an observational fact.

4.4.2 Height Dependence of the MFE

Figure 4.3 compares ME and SIR inversion results. Images in column c represent the vertical magnetic field flux density and column d shows the horizontal field flux density with magnetic field azimuth over-plotted with black arrows. The emerging magnetic flux is prominent in the FOV. Generally, the total magnetic flux density (column a) decreases with height, which is more pronounced in the sunspot penumbral and flux emergence regions. After resolving 180-degrees ambiguity, I converted the vector magnetic field from the native coordinate system into the heliographic coordinate system where the B_z component is normal to the solar surface. The corresponding field inclination maps are displayed in column b. The emerging flux region thus appears to have mostly horizontal fields with the inclination angle slightly above 90 degrees, and a minor increase with height is also visible here as well as in the nearby penumbra. The inverted total magnetic field strength and inclination angle from the ME method is slightly larger than the result from the SIR method, while the presented distribution are similar. The ME result mostly corresponds around the optical depth of $\log\tau =$ -0.7 of the SIR result, which supports the study of [73] that Fe I 1564.85 nm line is formed slightly deeper than the Fe I 630.25 nm line. I carefully examined the inclination angle of the ME inversion result and at each height of the SIR inversion, and found only one pixel in the ME output (b.1, point 0 marked with white “cross”) that showed 89.8 degrees inclination angle. Taking into account the error of measurements and inversion, that inclination angle cannot be considered as evidence of an opposite polarity field.

Table 4.1 Inverted Magnetic Field and Inclination with SIR Method

Point	1C or 2C	B_{total} (G)	γ (°)
U	1C	2150	176
P	1C	1617	147
0	2C	1549 1042	158 69
2	2C	1634 849	155 112
3	2C	1458 857	147 53
4	1C	1740	156

4.5 Summary and Discussion

In this study I report high-resolution observations of a MFE event in a granular LB, which was associated with enhanced brightening of the LB granules and Hα jets in the vicinity of the emerging flux. This kind of an MFE event occurring at the edge of LB is not rare and I observed a similar event appearing twice at the same location. Photospheric expanding OCC and brightness enhancements associated with a new emerging flux have been reported before (Cheung et al., 2008[74]; Lim et al., 2011[75]; Yurchyshyn et al., 2012[76]). Ji et al., (2012[27]) and Zeng et al., (2013[77]) also reported the granulation evolution and plasma ejections triggered by fine-scale MFE in the quiet Sun. However, these studies were mainly associated with bright points in inter-granular lanes. Bai et al., (2019[78]) reported similar jetting activity visible in solar chromosphere, transition region and lower corona, triggered by an emergent magnetic flux at one end of the LB structures. An elongated bright ribbon was observed at the footpoint of Hα jets along with an expanding OCC. Although lacking data on the evolution of vector magnetic field, the OCCs observed in Bai et al., (2019[78]), could be considered as evidence of a new emerging flux (Schlichnmaier et al., 2010[79]), which is supported by this study based on magnetic field data. The emerged magnetic structure in this study reached about 1.5 Mm in length and 0.3 Mm in width at the peak of development, and it had a lifetime of about 17 minutes, which is longer than those occurring in the quiet Sun. The total emergent magnetic flux during the emergence was about 1.91×10^{18} Mx, which is of the same order of magnitude as the total emergent magnetic flux of an MFE event observed in a quiet Sun region by Fischer et al., (2019[80]) and it is one order larger than those reported by Jin et al., 2008[81]; Gonzalez et al., 2009[82]; Goemoery et al., 2010[83]). NIRIS Doppler data showed enhanced upflows several minutes prior the first magnetic signatures of the emerging flux. The maximum of the upflow speed is about 2 km s^{-1}, which is at a higher end of peak upflow speeds found for quiet Sun MFE events (average speeds 0.83 km s^{-1} and maximum at 3 – 3.3 km s^{-1} (Jin et al., 2008[81]; Oba et al., 2017[84]).Louis et al., 2015[54] also reported an emergence of a new magnetic flux near one end of an LB. The emerged dipole measured about 3 Mm along its axis, which is nearly twice the size of this event. It also showed associated Doppler speeds to be about 2 km s^{-1}, which is very close to the speeds detected here, despite the fact that the formation height of Fe I 630.2 nm line is slightly higher than the Fe I 1564.85 nm line used in this study.

This work is the first report of brightness enhancement that occurred on the top of LB OCCs. During the emergence, the existing granulation was modified by the endpoints of the expanding OCC. Being pushed aside and compressed, the top of the granules appeared to have enhanced brightness. This MFE event was associated with jetting activity and a compact chromospheric brightening observed in the Hα

line. Based on the SIR 2C inversion analysis, I speculate that the jet, located next to the bright LB OCC and magnetic field emergence inner endpoint, was triggered by magnetic reconnection between the pre-existing background umbral magnetic fields and the emerging horizontal magnetic fields. This fan-like jet system was located in the umbra in close proximity to the edge of the LB and seemed to be co-spatial with the chromospheric brightening. During their evolution the jets slightly changed their orientation although they did not exhibit any significant lateral movements.

The recent work of Tian et al., (2018[57]) classified the surge-like activities above LBs into two types. Type-I surges are characterized by constant vertical oscillating motions with a relatively stable recurrence period and they are likely to be driven by shocks that form when p-mode or slow-mode magnetoacoustic waves are generated by convective motions propagating upward to the chromosphere. Type-II surges are characterized by impulsive ejection of chromospheric material from selected locations along LBs to heights normally exceeding 4 Mm and often reaching 10 Mm or more. They are driven by reconnection between newly emerged magnetic structures in the LBs and the surrounding umbral magnetic fields (e.g., Kurokawa 1988[48]; Tiwati et al., 2016[70]). Bharti et al., (2017[85]) reported λ-shaped jets in a sunspot and interpreted them as being a result of reconnection between an emerging arcade along the penumbral intrusion and the pre-existing background umbral magnetic field. The authors also noticed that instead of an arcade, rising heavily twisted flux rope (and possibly rotating) could also be the cause of the jets. Singh et al., (2012[86]) found systematic motions of λ-shaped jets due to the emergence of a three-dimensional twisted flux rope. However, previous studies lacked support from high-resolution vector magnetic field data. Without such high resolution data, the magnetic morphology was derived from lower resolution visible or EUV observations.

The data presented in this study is a step forward in the understanding of flux emergence and reconnection in a LB. First, I found that emerging fields seem to affect nearby LB granulation manifested as enhanced brightness of the top of a granule and prominent changes in the magnetic environment in the lower photosphere. The new flux emerging in LBs appears as a well organized, coherent and possibly current carrying structure as evidenced by the rotation of the transverse field during the emergence. Although the event displayed signatures of a bipolar flux emergence, I did not convincingly detect any opposite polarity fields in the emergence region. One reason for that could be a specific morphology of the emerging flux. The target sunspot was located at S12, W56 so that strong projection effect combined with strongly inclined fields made it difficult to resolve the opposite polarity in the local solar surface coordinate system. At that longitude, a significant fraction of the vertical field will be observed as transverse fields so that ambiguity resolution and correction for the projection effect are necessary to reveal real morphology of the emerging flux. Additionally, the outer penumbral endpoint that is supposed to be of the following polarity could have lower field intensity, which probably presented additional difficulties for resolving and detecting these magnetic elements at that viewing angle.

CHAPTER 5

CRYOGENIC INFRARED SPECTROGRAPH (CYRA)

5.1 Introduction

IR solar spectrum, which is not yet widely observed by the ground-based solar telescope, gathers abundant information of the solar activities in the photosphere and chromosphere. Spectral observations, utilizing this largely unexplored wavelength band with various of atomic and molecular spectral lines, are crucial for solving many critical problems in solar physics. CYRA is a newly developed focal-plane instrument operating from 1 to 5 μm for the GST/ BBSO.

The major scientific motivations for CYRA are the measurement of solar magnetic field in solar lower atmosphere and the diagnosis of the chromosphric structure in the IR. The wavelength splitting of Zeeman effect for the atomic sub-levels increases by a factor of $g_{\mathrm{eff}}\lambda^2$. Meanwhile, the spectral line broadening, induced by the Doppler effect of solar micro and macro-turbulent velocities, increases with λ. Thus, a measure of the magnetic resolution of a spectral line is given by the ratio of Zeeman splitting divided by the spectral line width, varying by the factor of $\lambda \cdot g_{eff}$. The effective landé g-factor, g_{eff}, can be calculated with atomic models. Solar spectral lines usually have values of g_{eff} between 1.0 and 3.0. Although there are many spectral lines that have lager values of g_{eff}, to increase the wavelength of the observations usually takes more advantages (e.g., the magnetic sensitivity can increase by a factor of 10 when the wavelength changing from 0.5 μm to 5 μm). Another scientific advantage for infrared solar physics is that there are a large number of molecular rotation-vibration lines. Transitions between vibration states, always coupling with transitions between rotational states, lead to the infrared emission. Due to the thermal instability, molecules only exist in the coolest regions in the solar atmosphere and will be easily destroyed by the thermal perturbation. This feature, provides us a way to probe the cool regions around the sunspot and the temperature minimum in the quiet Sun.

There are two methods to do imaging spectroscopy. One is to take a series of monochromatic images at different wavelengths in a short time with a tunable filter. The imaging spectroscopy based on a Fabry-Pérot interferometer can do excellent imaging with high spatial resolution to the telescope diffraction level. While the disadvantages for this technique are limited free spectral range and relative lower temporal resolution. NIRIS, using a dual Fabry-Pérot etalon, is a good example of this kind of instrument. The other way is to take a series of spectrograms using a grating-spectrograph with a fast scanning slit across the whole FOV. The Fast Imaging Solar Spectrograph (FISS) of the GST is one of this kind instrument, designed to study the fine-scale structure and dynamics of chromospheric plasma, working in the visible wavelength. CYRA, taking the advantage of the grating spectrograph, can directly obtain spectral profiles within a wide free spectral range.

5.2 CYRA Development Strategy and Expected Performance

The GST is configured as an off-axis Gregorian system consisting of a parabolic primary, prime focus field stop and heat reflector (heat-stop), elliptical secondary and diagonal flats. CYRA is located at one floor beneath the telescope deck feed from the Gregorian focal plane. To achieve the scientific and instrumentation advantages of IR solar physics with CYRA, I need to acquire observational data with high temporal and high spatial resolution. The whole system are consisted by fore-optics module and internal elements shown in Figure 5.1. Table 5.1 lists preliminary instrumental characteristics of CYRA. Beam that gathered and collimated by GST will first come to the fore-optics module through a K-mirror image de-rotator. After correcting the Coudé feed rotation and orienting the solar images on the spectrograph slit, light will travel through a tip/tilt mirror to a beam splitter. The reflected beam will reach to a context imager to provide observation live image and a wavefront sensor which, together with the tip/tile mirror, forms a correlation tracker (CT) subsystem . The telluric atmosphere distortion signal, detected by the wavefront sensor will be fed back to the tip/tilt mirror to correct the beam aberration. Transmitting light, after corrected by the CT system, will transfer through an active image scanner and create solar slit images after an intermediate slit.

The image scanner of CYRA performs high accuracy transverse motion driven by step motor. It uses two-mirror system and therefore deflect the incoming beam by 180°. Comparing to the three-mirror, also known as K-mirror system, the two-mirror system is smaller in size and simpler in structure. The image on slit plane at the scanner position is 16 mm × 16 mm in size, which corresponds to the 80" × 80" FOV of the solar image. Light beam will be blocked by the scanner slit and a slit jaw image will be delivered the internal elements in the cryostat.

There are two methods to do imaging spectroscopy. One is to take a series of monochromatic images at different wavelengths in a short time with a tunable filter. The imaging spectroscopy based on a Fabry-Pérot interferometer can do excellent imaging with high spatial resolution to the telescope diffraction level. While the disadvantages for this technique are limited free spectral range and relative lower temporal resolution. Full-Stokes Near Infra-Red Imaging Spectropolarimeter (NIRIS, [87]), using a dual Fabry-Pérot etalon, is a good example of this kind of instrument. The other way is to take a series of spectrograms using a grating-spectrograph with a fast scanning slit across the whole field of view (FOV). The Fast Imaging Solar Spectrograph (FISS) of the GST is one of this kind instrument, designed to study the fine-scale structure and dynamics of chromospheric plasma, working in the visible wavelength. CYRA, taking the advantage of the grating spectrograph, can directly obtain spectral profiles within a wide free spectral range.

A filter wheel is mounted at the entrance of the cryostat, with totally ten slots available for pinhole and different IR filters. The filters in stock at GST is listed in Table 5.2. Currently, one pinhole with four filters for Ti I 2231 nm line, Si IX 3934 nm line, Fe I 4137 nm line and CO 4667 nm line has been installed. For each filter, a compatible image slit is mounted together on the filter wheel.

Table 5.1 CYRA Instrument Characteristics

Instrument Parameters	Variable	Value
Wavelength range	λ	2∼5 μm
Field of view	FOV	80” × 80”
Slit width	ω	15λ
Image focal length	f	1440 mm
Grating groove density	$1/\sigma$	31.6 mm^{-1}
Grating blaze angle	ϕ	71°
Spectral resolving power	R	$\sim 10^6$
FPI	HAWWII II	HgCdTe
Camera format	$Nx \times Ny$	2048 × 2048
Pixel size	$\delta \times \delta$	18 mum × 18μm

The internal elements consist a fully cryogenic folded Czerny-Turner spectrograph utilizing a 2048 × 2048 HgCdTe array with quantum efficiency approaching to 80% and a maximum frame rate of 76 Hz. All the internal elements, shown in Figure 5.1(b), will be closed in a dual layer cryostat. They will be cooled down during the observation (about 70 K for the outer cryostat and 30 K for the inner cryostat), greatly decreases the background infrared emission. The grating is 220 mm × 420 mm with a grating constant of 12.66 μm. The spectral resolution (R_0) ranges from 150,000 up to 750,000 depending on wavelength. Changing the single fold mirror FM5 to a beam-splitter, the spectrograph working mode will be switched from performing spectrograph to a dual-beam polarimetry. The final image will be 9 mm in the spatial direction and 18 mm in the spectral. The image will cover 500 vertical pixels for a plate scale of 0".16/pixel, halving the GST's resolution at 2 μm.

Table 5.2 IR Filters in Stock

Central Wavelength (nm)	Bandwidth (nm)	Peak Transmission	Stock
1565	9.5	84%	4
2231	12	77%	3
3681	20	85%	2
3697	16	86%	2
4064	19	76%	2
4135	18	75%	2
4669	47	68%	2

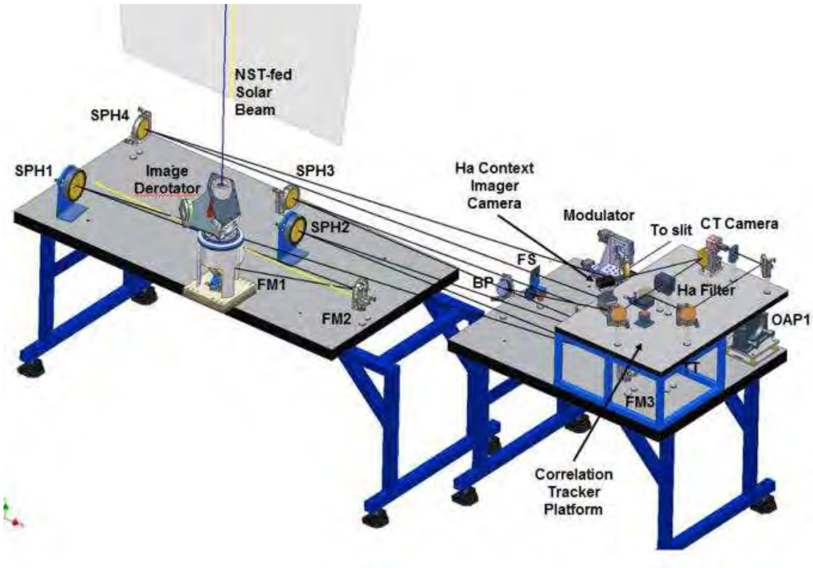

(a) Fore-optics module

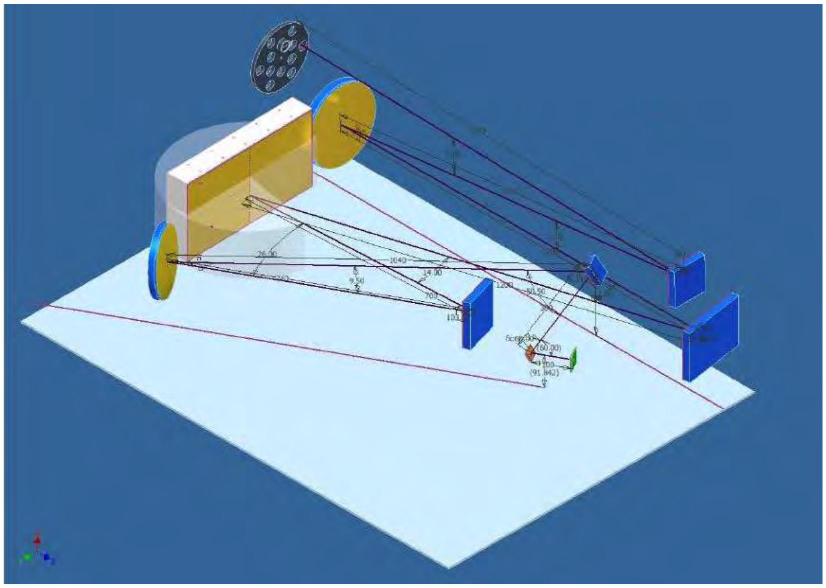

(b) Internal elements

Figure 5.1 CYRA optics design.

(a) Cryostat

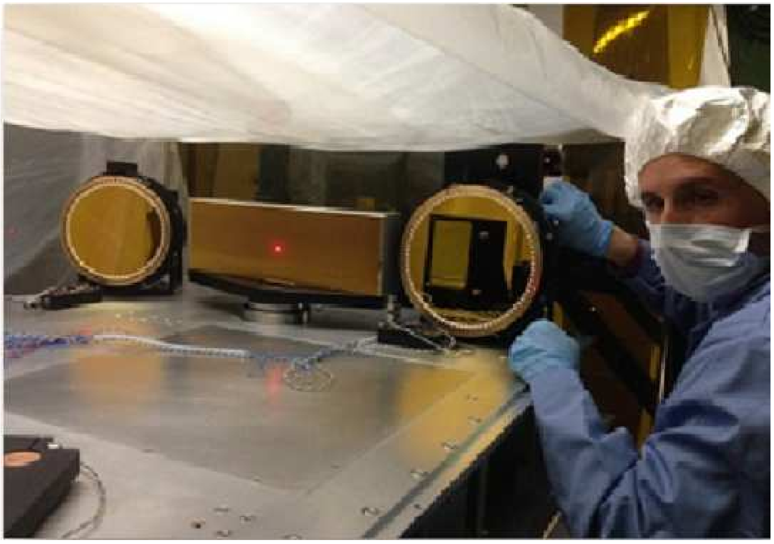

(b) Grating and mirrors inside the cryostat

Figure 5.2 Cryostat and the Spectrograph.

5.3 System Commissioning

My work on CYRA includes both instrumentation and science. I have performed several engineering tests during year 2014 to year 2016 and threes scientific observations since year 2107. The author is responsible for the system commissioning, giving feedback to the engineer team as well as processing and analyzing the observed spectrum data.

5.3.1 System Vibration

One serious issue was the vibration problem induced by the compressors of cryostats. Those compressor pumps impact the cryostats and shake the spectrograph elements. Therefore, the observed spectrum presents obvious vibrations, in both spatial and wavelength directions. The vibration in spatial direction reduces the scanning spatial resolution while the vibration in wavelength direction broadens the spectral line, which can result to inaccurate magnetic field measurement.

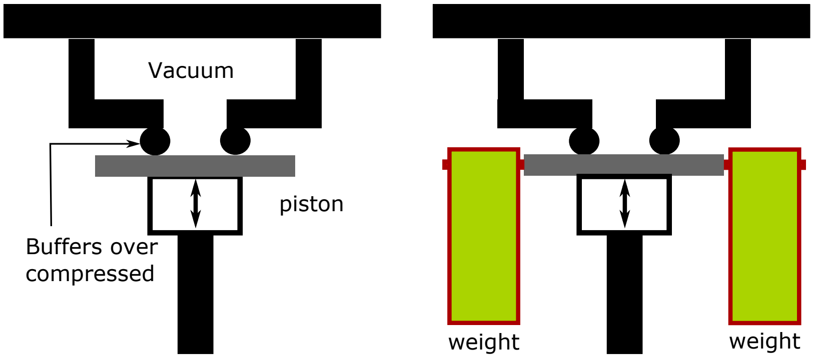

(a) Original compressor (b) Piston loaded weight

Figure 5.3 Pistons of the compressors over compress the buffers.

After loading weights to the two cryogenic compressors, setting pads for the tubes and checking the grating installation, the vibration problem is partly solved, shown in Figure 5.5. The vibrating amplitude become smaller and some high frequency mode is totally disappeared. By measuring the spatial shifts between each

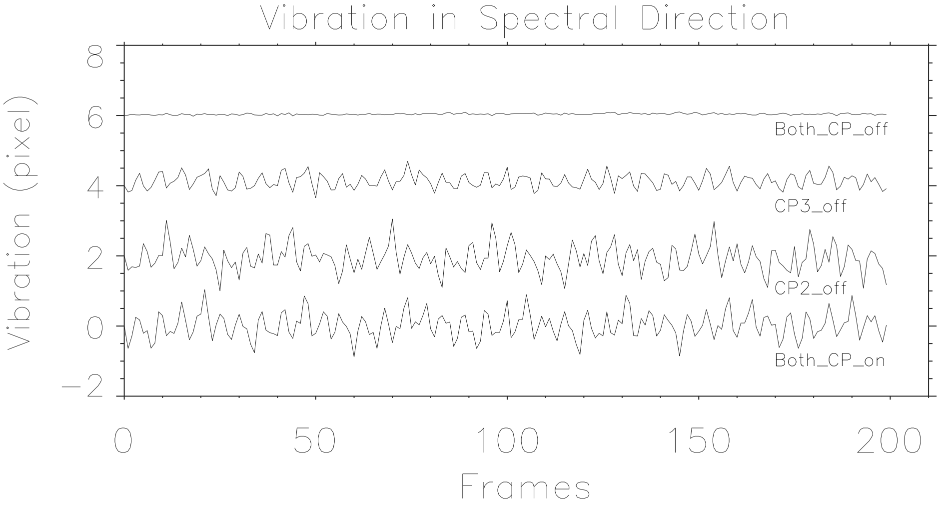

Figure 5.4 Spectral vibration with compressors on/off.

image in a long sequence, I make a plot for the vibrations of the two directions. Shows in Figure 5.5.

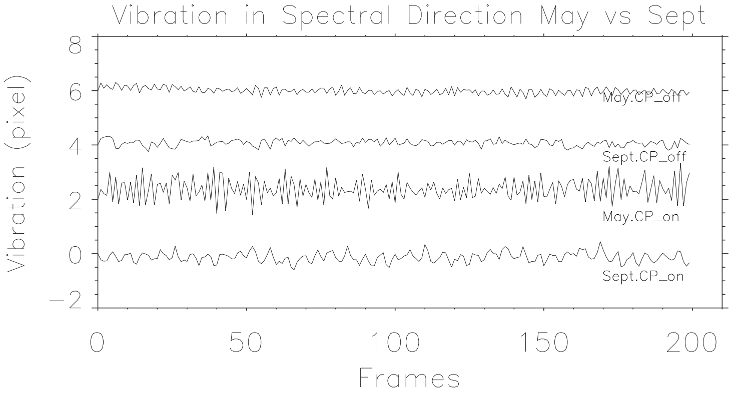

(a) Vibration in spectral direction

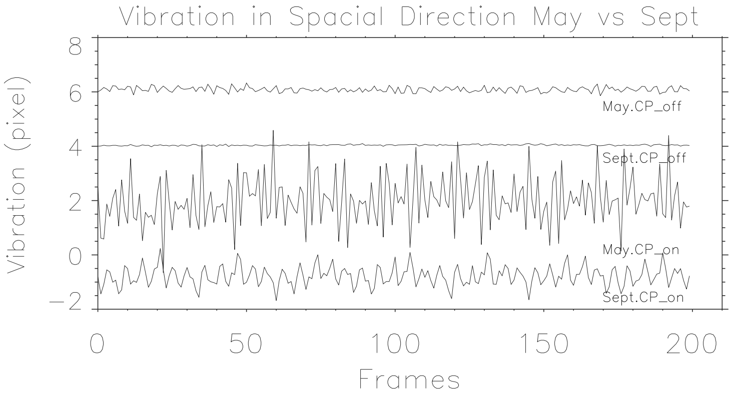

(b) Vibration in spatial direction

Figure 5.5 Spectrum vibration in spectral/spatial direction Sept. 2015 vs May. 2015.

Compared with data taken in 2015 May, data taken in 2015 September has better quality. Some high frequency component vibration disappeared and only low frequency component vibration was left. Currently, the main vibration signals are presented in the wavelength direction, which could be induced by the grating shivering. They are not significant, but still noticeable and blurs the high spectral resolution spectrum.

One urgent care to this issue is to turn off the compressor of the outer cryostat during data collection. However, it leads to another problem of how will the temperature change with this turning-off, and how long I can turn off the compressor of outer cryostat without damaging the camera and other internal elements.

Turning off the outer cryostat compressor for 15 minutes will only heat up the outer shield by 2 K and seems have no influence to the inner shield temperature. However the recovery to the original situation seems to be a long term mission which would take overnight time. The conclusion is, temporary turning-off the outer shield cooler for several single minutes during the observation is a way to increase the image quality, just before this vibration issue can be solved by engineer methods.

During the summer of 2016, I worked on the newly designed copper rope thermal conductors, which are more flexible than the old copper foil ones. As shown in Figure 5.6, the rope, which contains lots of copper fibers, is much softer. Thus, it can absorb the vibration coming from the thermal head, instead of propagating it to the cryogenic shell and the internal optics elements.

Removing the thermal conductor from the compressor's thermal head was a big work. To change the one for the outer shell, I need to lift the inner up the cyrostat. When I change the one for the inner shell, I need to lift up its whole optical plate. The most important thing I need to take care is not to break the vacuum. Any dust, spittle or finger print may induce difficulties for the cryostats evacuation.

As presented in Figure 5.7, the new cooper rope thermal strap works well. The vibration is one order smaller than the original measurement. The improvement can be seen directly from the vibration plot and the spectrum live image. The vibration shows no difference when I turn off the compressors, which means energy does no longer propagates from the compressors to the CYRA internal elements.

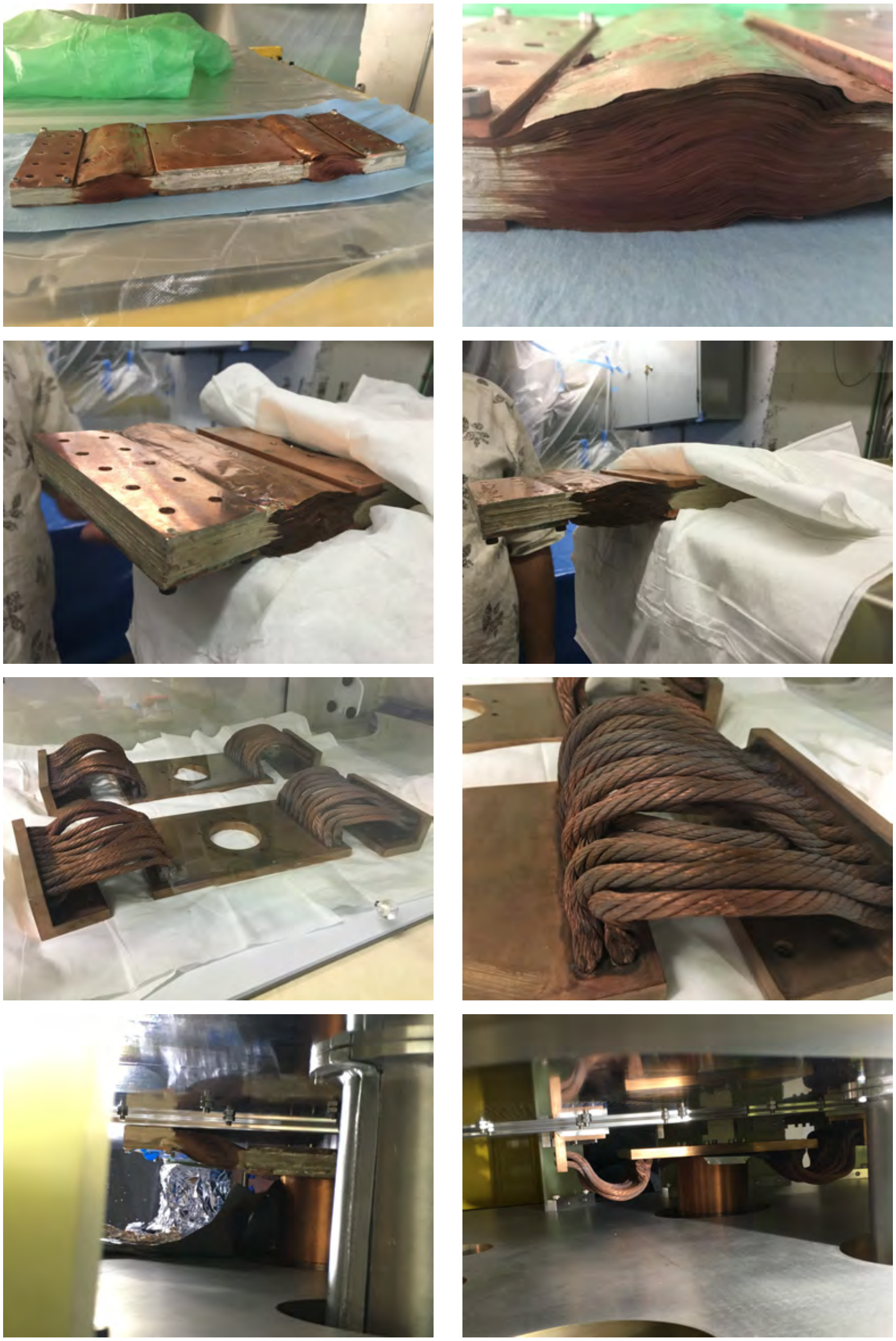

Figure 5.6 Old cooper foil strap and new copper rope strap. The first two rows show the old foil thermal strap which is quit inflexible. The third row shows the new rope thermal strap. The last row shows the before/after I changed the straps.

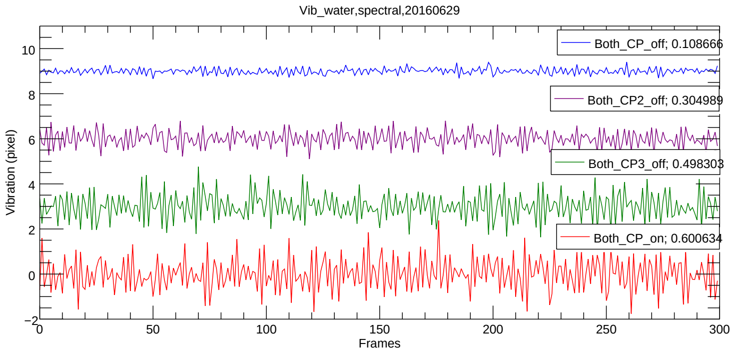

(a) Vibration measurement with outer shield new thermal strap at 201560629

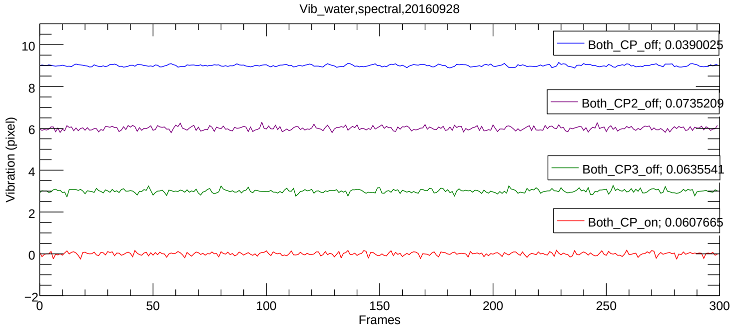

(b) Vibration measurement with outer and inner shield new thermal strap in 20160928

Figure 5.7 Spectrum vibration in spectral/spatial direction after replacing thermal strap.

5.3.2 Camera Performance Test

Camera performance, including linearity and gain, test for a camera is one important step before put it into scientific data acquisition. Scientific measurement requires the measured intensity to be proportional to signal intensity. However, some parts of the image will get saturated by overexposure when observing with long exposure time. Offset from the linearity induces inaccuracy between measured intensity and signal intensity. A linearity test has been made to the camera of CYRA, shows in Figure 5.8.

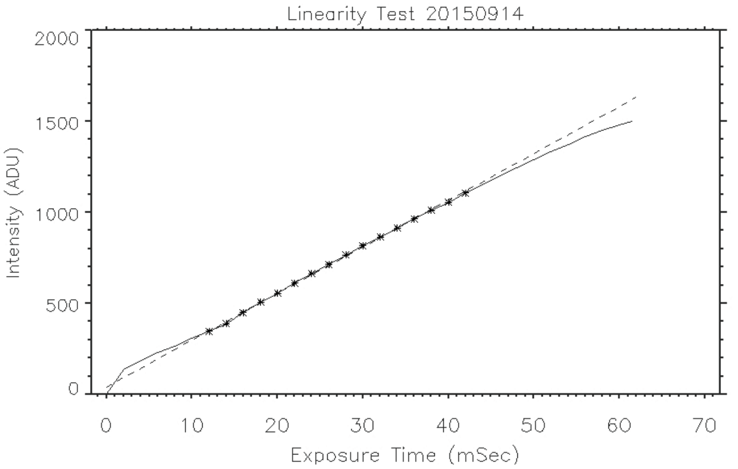

(a) Intensity vs exposure time (with CO filter)

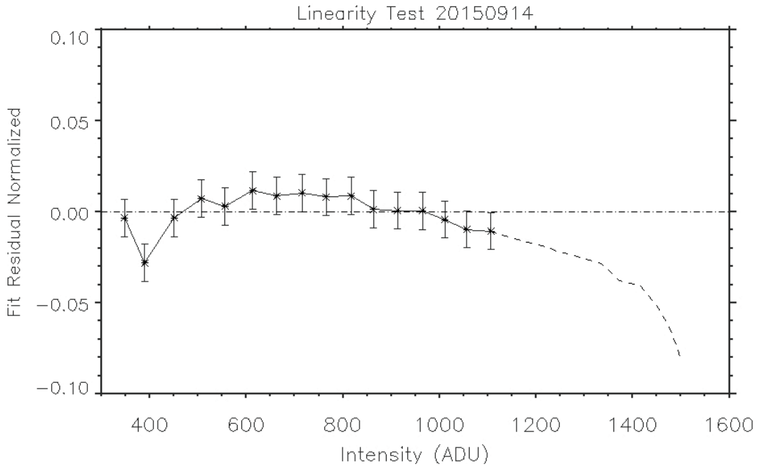

(b) Difference between measured data points and the fitting line over intensity.

Figure 5.8 Linear fit for the camera measured averaged intensity in a data box over exposure time. The chosen data box locates in a good image quality region that is always used during the observation. Solid line is the measured data points; those marked with stars are chosen for linear fit (dash line). It shows good linearity when the exposure time is between 15 ms and 42 ms.

5.3.3 Data Acquisition

CYRA can work in spectrograph mode and spectropolarimeter mode. For each observation mode, three kinds of data, including science data, dark fields image and flat fields image, will be recorded by the instrument. To obtain usable scientific spectrum image, certain data reduction process should be applied on the raw data. Firstly, dark fields data are taken by exposing when the telescope mirror cover is closed. One hundred frames of dark images are recorded with the same exposure time as used for science data. The average frame of the dark fields data is used for locating the bad pixels and creating bias image. Secondly, flat fields data are taken several times during a day for each observing wavelength, by wobbling the telescope FOV around quiet sun region near solar disk center. An average frame of total 1000 images is used to calibrate the spectrum slat and distortion, after subtracting the dark field and replacing bad pixels that detected in the dark field. Thirdly, the non-uniform pattern of spectrum will be corrected. I decompose the flat pattern in to the spatial pattern along the slit direction and the spectral pattern along the wavelength direction. The Figure 5.9 shows the data reduction pipeline.

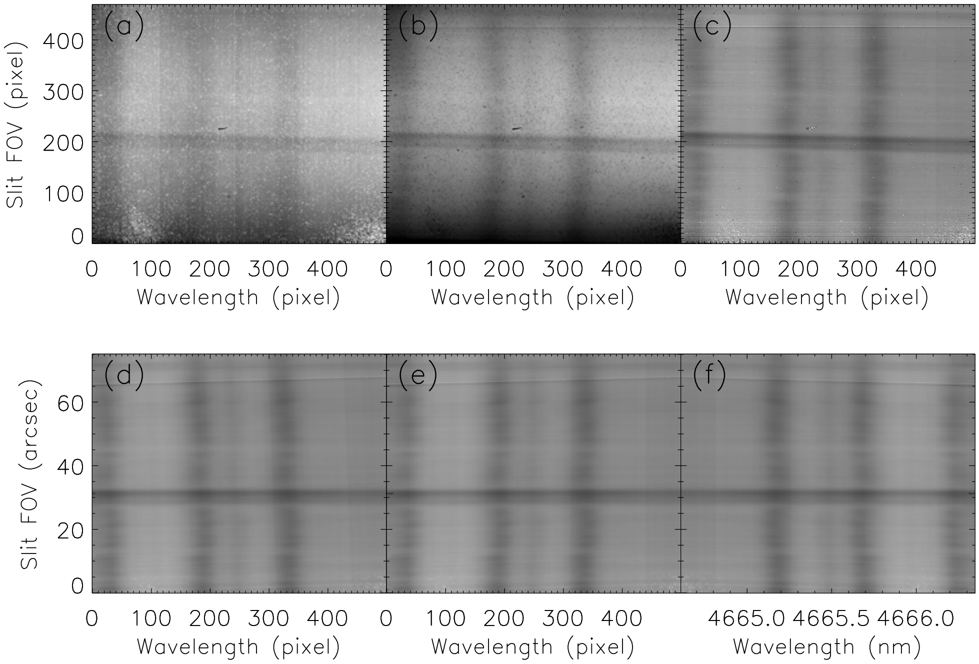

Figure 5.9 Data reduction for CO lines near 4667 nm. The raw data (panel a) is processed with dark fielding (panel b), flat fielding (panel c), bad pixel and hot pixel correction (panel d) and spectral line tilt/curvature correction to get usable spectrum as in panel e. From panel e to panel f, the spectrum has been flipped in the wavelength direction and the the unit for the x-axis has been calibrated from pixel to physical wavelength.

For Ti I 2231 nm, according to the line formation is limited in the sunspot, there is another step to obtain the Zeeman splitting signal. The quiet Sun background need to be removed from the spectrum.

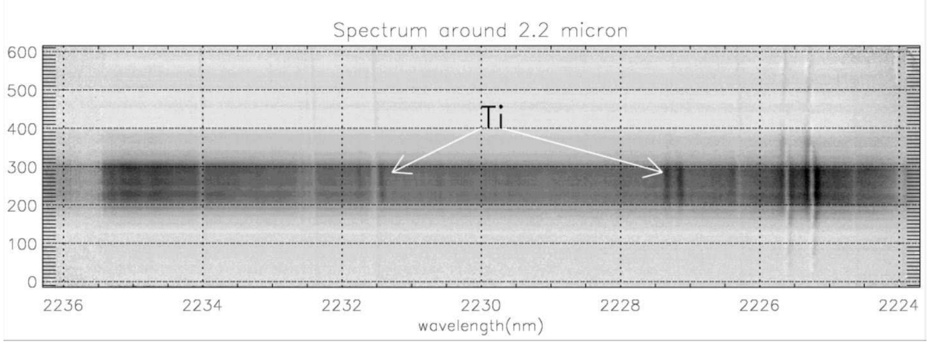

Figure 5.10 Zeeman effect in sunspot for spectral lines around 2231 nm. The dark band in the spectrum is the sunspot. Obvious Zeeman splitting can be observed for Fe 2225.7 nm, Ti 2227 nm and Ti 2231 nm lines.

5.4 Science Studies

Carbon-monoxide line at 4667 nm and neutral Titanium line at 2231 nm are the best spectral lines to test the new instrument.

5.4.1 CO Lines Near 4667 nm

CO molecule spectral lines are widely observed in Astronomy. Its rotational transitions emitting sub-millimeter radiation, can be used to detect interstellar molecular clouds. A variety of CO rotation-vibrational transitions, radiating in infrared wavelengths, surprisingly appears in solar observation. At 4667 nm or wave number around 2143 cm^{-1}, a group of three CO lines (2-1 R6, 3-2 R14, 4-3 R23) was first observed at 1972(Hall et al.,1972[88]) and became a hot topic of infrared solar physics in the following decades.

Early work indicates that these very strong molecular ro-vibrational absorption lines at the extreme limb and off-limb, reveal the very cool temperatures (3500 K) at the supposed hot solar chromosphere (5000 K). The existence of these strong lines means the existence of a large amount of cool gas, however at the same height (400∼480 km), the formation of Ca II and Mg II emission needs a much higher temperature. This apparent conflict has a great impact to the classical solar atmosphere model.

Confined by the telescope spatial and temporal resolution, the classical model explains the solar atmosphere in a view of layers. Begin from the height where the optical depth for 500 nm light $\tau_{500nm} = 1$, there are photosphere, chromosphere and corona - a temperature minimum between the first two layers and a transition region between the last two layers.

Thanks to the advanced instrumentation, modern theory gives a more detailed picture for the fine structures in the solar atmosphere. As shown in Figure 5.11, CO clouds will not appear near the flux tube concentration. This is because, molecules

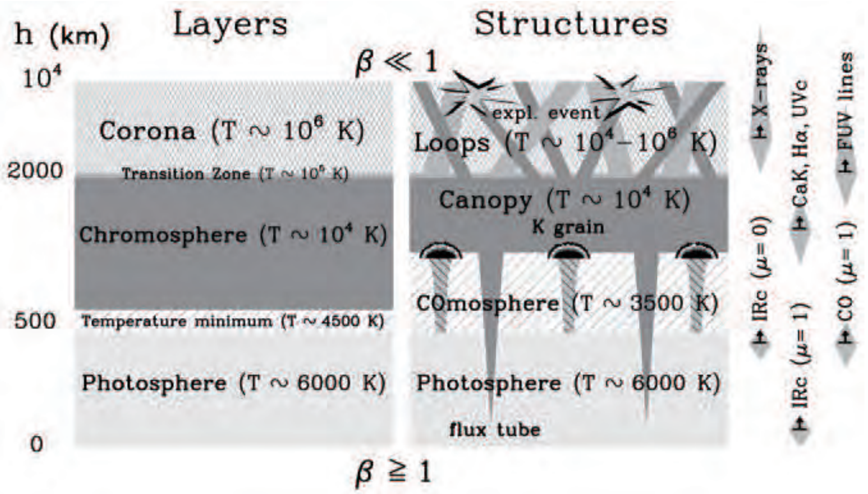

Figure 5.11 Taking CO observation into consideration, the classic "Layers" model of the solar atmosphere should get evolved to a complicated "structure" model, mixing cool ("CO") and hot gas at the similar height, witch is temporal dynamic and spatial chaotic.

Source: Ayres, ApJ, 2002[2]

are not only sensitive to temperature, but also unstable to gas pressure. In higher temperature, heated atoms has more energy to break the internal bound force, however, with a lower gas pressure, the external force that bound the atoms together is weaker. Considering the local thermodynamic equilibrium (LTE), under which there is a balance between gas pressure and magnetic pressure of solar plasma, the strong magnetic field around the flux tube produces high temperature and low gas pressure, and this will in turn decompose the molecule clouds.

Taking advantage of the strong dissociating at temperatures over 4000 K, the CO lines are very suitable for probing the energy transition from the photosphere to higher solar atmosphere. These molecular lines, with narrow contribution function, are existing closely in LTE. Visible atomic lines, on the contrary, strong enough to arise at high altitudes commonly, are affected by NLTE formation, which sharply diminishes their value as thermodynamic tracers. In this case, these CO 4667 nm lines have the potential to be the best lines to reveal the process about how will the lower atmosphere activities influence the higher atmosphere structures and how does the energy transmit from the low temperature inner atmosphere to the high temperature outer atmosphere, which is known as the "Corona Heating" problem.

5.4.2 Study of Spectroscopic Diagnostic of Sunspot Oscillations with IR and EUV Lines

Figures in this part are from Li & Yang et al. 2019, which has been submitted to The Astrophysics Journal and currently under review.

Oscillations are important phenomena in sunspots. Sunspot oscillations can be observed at various layers in solar atmosphere and can be observed in umbrae and in penumbrae above sunspots and in sunspot light bridges (Khomenko & Collados 2012[89]). The detected oscillations in sunspots are normally MHD waves and often interpreted as wave fluctuations. The dominant period of sunspot oscillation in photosphere is about 5 minutes ((Beckers & Schultz 1972[90]; Lites 1988[91]) which is considered to be correspond to the 5-minute p-mode wave ((Thomas 1985[92]; Bogdan 2000[93]; Solanki 2003[35]). Meanwhile, a 3-minute oscillation mod can be detected in photosphere through chromosphere and transition region to corona, supporting the hypothesis of propagating waves ((De Moortel et al. 2002[94]; O'Shea et al. 2002[95]; Brynildsen et al. 2004[96]). Other than these two kinds of oscillations, the running umbral waves (Kobanov & Makarchik 2004[97]; Liang et al. 2011[98]) and running penumbral waves are observed propagating from interior to exterior of the sunspots.

Quasi-periodic oscillations of sunspot are most often seen in the Doppler velocity of spectral lines. At photospheric layers, the velocity fluctuations at both umbra and penumbra of sunspot are similar to the surrounding photosphere. However, the oscillation amplitudes at sunspot umbra and penumbra are clearly reduced when compared to their surroundings, i.e., no more than 1 km s^{-1} (Howard et al. 1968[99]; Soltau et al. 1976[100]; Lites 1988[101]). Doppler shift oscillations of sunspots are much more apparent and easier to be detected in chromosphere, such as the spectral lines of Ca II H & K, He I 10830 Å , Hα off-band, Mg II H & K, C II , and some molecular lines (Lites 1986[102]; Solanki et al. 1996[103]; Bogdan 2000[93]; Khomenko & Collados 2015[89]). Moreover, the oscillation amplitudes at chromospheric umbra are much larger, which can be about 10 km s^{-1} or even much larger (Centeno et al. 2008[104]; Tian et al. 2014[105]). Doppler shift oscillations above sunspots have also been found in transition region, such as the extreme ultraviolet (EUV) spectral lines of Si IV , C IV , and O IV (Gurman et al.1982[106]; Fludra 2001[107]; Maltby et al. 2001[108]). It is still very difficult to observe the intensity fluctuations at photospheric sunspots, since their amplitudes are very small (Beckers & Schultz 1972[90]; Bellot Rubio et al. 2000[109]). Although some authors have detected the very weak intensity fluctuations in G-band, TiO or visible continuous images (Nagashima et al. 2007[110]; Yuan et al. 2014b[111]; Su et al. 2016[112]). While in chromosphere, the intensity oscillations of sunspots are called as "umbral flashes", which are often accompanied by the up and down motions with periods of about 2∼3 minutes (Wittmann 1969[113]; Phillis 1975[114]). Observations also show that the umbral flash is often associated to a vertical wave propagation, suggesting that it is caused by an upward shock propagation (Gurman 1987[115]; Rouppe van der Voort et al. 2003[116]). Finally, the sunspot oscillations in corona have also been reported with a period of roughly 3 minutes, which might be associated with magnetoacoustic waves. They are usually observed at the footpoints of magnetic fan-like loops above sunspot in EUV images(Handy et al. 1999[117]; Nakariakov et al. 2000[118]; Uritsky et al. 2013[119]), or at umbra with the coronal heights in radio observations (Shibasaki 2001[120]; Gelfreikh et al. 2004[121]; Sych & Nakariakov 2007[122]).

Part of the fundamental vibration-rotation transition lines of CO are in the solar infrared spectrum near 46655 Å (Ayres & Wiedemann 1989[123]; Goorvitch 1994[124]). The CO molecular lines contain a wealth of cool plasma at low solar atmosphere, where the temperature could be as cool as ∼3700 K (Solanki et al. 1994[125]; Ayres 1998[1], 2002; Uitenbroek 2000[126]). Therefore, they are valuable tools to investigate the dynamic behaviors of cold heart solar atmosphere, i.e., temperature minimum region between upper photosphere and lower chromosphere on the Sun(Ayres et al. 2006[127]; Penn 2014[6]).. For example, based on the spatially resolved solar infrared CO spectrum, a primary 3-minute period is found in the line-center intensity or depth, while the dominant 5-minute oscillations are clearly seen in the Doppler velocity. Both the normal and inverse Evershed flows at sunspot penumbra are also observed. While using the McMath-Pierce solar telescope on Kitt Peak at National Solar Observatory, the sunspot oscillations at umbra are well separated by double periods of ∼3 minutes and ∼5 minutes in CO molecular lines (Solanki 1996[103]). Using the same facility, oscillations across the whole Sun are detected from the line-core intensity and Doppler velocity in the molecular lines of CO, and these oscillations are thought to be solar p-modes. On the other hand, the typical 5-minute oscillations in the photospheric layer are also found in CO molecular lines, and their peak-to-peak amplitudes of brightness-temperature fluctuations are roughly 225∼300 K, while the peak-to-peak amplitudes in Doppler velocities are ∼1.1 km s^{-1}(Noyes & Hall 1972[128]; Ayres & Brault1990[129]).

The Doppler velocity and line intensity oscillations across the sunspot umbra and penumbra are very complex, which are helpful to understand the magnetic fields and the physical nature of sunspots. In this study, I investigated the sunspot oscillations using solar infrared spectrum, near-ultraviolet (NUV) and far-ultraviolet (FUV) lines. My data are the conjunctions with the ground- and space-based observations, such as the Cryogenic Infrared Spectrograph at Big Bear Solar Observatory (BBSO), the Interface Region Imaging Spectrograph (IRIS, De Pontieu et al. 2014), and the Atmospheric Imaging Assembly (AIA, Lemen et al. 2011[130]) aboard Solar Dynamics Observatory (SDO).

Observation A sunspot near solar disk center at the active region of NOAA 12680 (N08E01) was measured by multiple instruments, including the ground- and space-based telescopes. Figure 5.12 (a)∼(c) shows the SDO/AIA images with a region of interested about 66” × 80” in UV 1600 Å and 1700 Å, as well as visible 4500 Å. They have been pre-processed with the standard AIA routines in solar software (SSW) package (Lemen et al. 2011[130]). AIA 1700 Å and 4500 Å are continuum radiation from photosphere (PH) or temperature minimum (TM) region, and their characteristic temperature is about 5×10^3 K. The AIA 1600 Å emissions are usually from the continuum and C IV line in upper photosphere or transition region (TR), which have formation temperatures of around $6{\times}10^3$ K or 10^5 K (Lemen et al. 2011[130]). A typical sunspot near solar disk center can be seen in these three images, and it is composed of two umbrae and one penumbra, as outlined by the green and purple contours in panels (b) and (c). The sunspot umbrae are separated into two pieces by a light bridge. This sunspot was also measured by IRIS with a large coarse 2-step raster mode from about 16:40:15 UT to 18:01:59 UT on 2017 September 15. The step size is ∼2”, and the time cadence between two nearby slit positions is roughly 19 s. Figure 5.12 (d) and (e) shows the NUV images in 2796 Å and 2832 Å recorded by the Slit-Jaw Imager (SJI) aboard IRIS. SJI 2796 Å image contains radiation primarily from Mg II K line, which is formed in chromosphere (CH) with a formation temperature of $\sim 10^4$ K. SJI 2832 Å emits the radiation dominated by Mg II wing, where the temperatures are roughly $5{\sim}8 \times 10^3$ K. In this observation, the double slits of IRIS are along solar north-south direction and go through the sunspot, as indicated by two blue vertical lines.

During this observations, GST/CYRA measured the sunspot between ∼16:50:14 UT and ∼17:32:25 UT on 2017 September 15, and it performed small 13-step raster scans with a step size of ∼0.4”, while the time cadence between two nearby raster scans is about 15 s. To co-align with other instruments, I also performed a large

400-step raster scan between around 18:14:13 ~18:18:23 UT with a step size of ~0".2, as shown in Figure 5.12 (f)~(i). Panel (f) shows a large raster scan image in infrared continuum nearby the CO 3-2 R14 line with a FOV of around 66" × 80". Two purple "×" symbols mark the crossover points between the second IRIS slit and the penumbral-photospheric boundary. Panels (g)-(i) present the large scan images with a same FOV in line intensity, line width and Doppler velocity of the CO 3-2 R14 line, respectively. Two oblique red lines indicate the first (solid) and 13th (dashed) slits of CYRA small raster scan, which are along a ~29° angle to the solar north-south direction. It can be seen that the slits of CYRA and IRIS are overlapping together in one position ($x \approx$ -67", $y \approx$ 23") at sunspot umbra, as shown by the cyan "$*$" symbol. Finally, panel (i) demonstrates that the penumbra of this sunspot (near solar disk center) shows mainly blue shift, suggesting that there is a horizontal outflow at sunspot penumbra in the photospheric layer, which is best known as the Evershed flow (e.g., Evershed 1909[131]; Uitenbroek et al. 1994[132]; Solanki 2003[35]).

Figure 5.13 (a) shows the solar infrared CO spectrum at ~17:00:45 UT observed by GST/CYRA in its first slit, as indicated with the red solid line in Figure 5.12. A series of absorption lines can be seen from the solar infrared spectrum nearby CO molecular lines. Then, eight obvious lines are identified and labeled with short magenta ticks, including seven CO molecular lines and a telluric line. In this dissertation, two CO molecular lines are applied to study the sunspot oscillations, i.e., a strong line of CO 3-2 R14 and a weak line of CO 7-6 R67. Their formation height is around 500 km above the τ_{500} 500 = 1 (z = 0), ranging from photosphere through temperature minimum region to lower chromosphere. The weak line (CO 7-6 R67) is probing the lower solar layers, such as photosphere. While the strong one (CO 3-2 R14) could vary from roughly 150 to 580 km above $\tau_{500} = 1$, which probes the upper photosphere, temperature minimum region, as well as the lower chromosphere (Ayres 1998[1]; Uitenbroek 2000[126]; Ayres et al. 2006[127]). In addition, a telluric line is also extracted to monitor the variations of Earth's atmosphere and the whole instruments.

Figure 5.13 (b) and (c) displays the IRIS spectra in NUV and FUV bands at around 17:00:41 UT in the second slit, as indicated by the blue solid line in Figure 5.12. They have been pre-processed with the standard IRIS routines in SSW package (De Pontieu et al. 2014). The overplotted curves are the line profiles at the solar position nearby y $\approx$ 23", as marked by a short cyan line on the left side of each panel. The double resonance lines of Mg II K & H are identified in panel (b), and they are mostly formed in chromosphere with a formation temperature of $\sim 10^4$ K. The Si IV 1393.76 Å is also identified in panel (c), which is formed in transition region and has a formation temperature of around 6.3×10^4 K. It can be seen that the signal-to-noise ratios of Si IV 1393.76 Å is a little lower at the most positions of this sunspot.

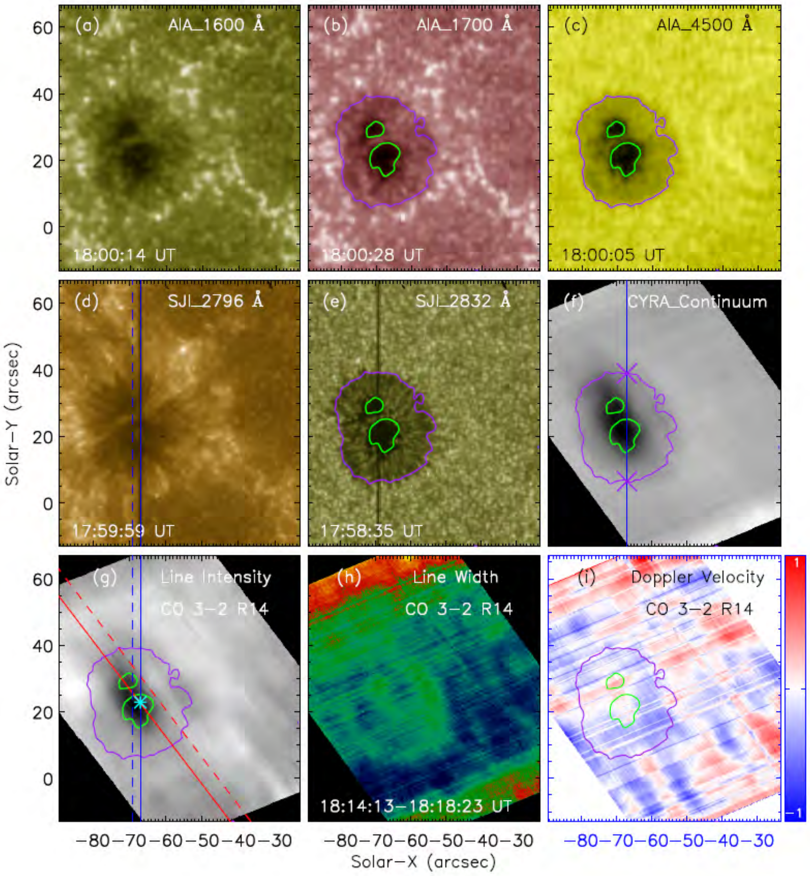

Figure 5.12 Nearly simultaneous snapshots and CO large scan images on 2017 September 15 measured by SDO/AIA, IRIS/SJI, and GST/CYRA. The green and purple contours are derived from the visible continuum radiation in AIA 4500 Å. Two blue lines represent IRIS slits, and double red lines mark the first and last (13th) slits of CYRA. Two purple × symbols in panel (f) marksthe penumbral-photospheric boundaries at the second IRIS slit. The cyan ∗ symbol in panel (g) indicates a crossover point between the slits of IRIS and CYRA at sunspot umbra.

Source: Li & Yang et al., 2019a

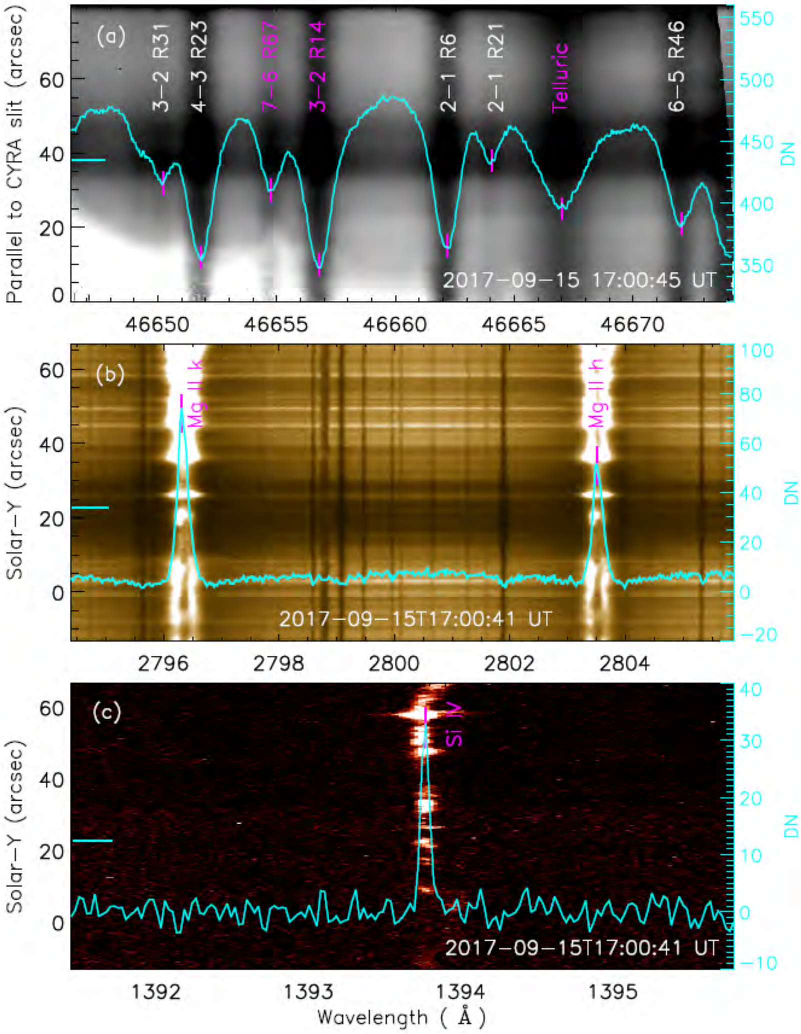

Figure 5.13 Solar spectra in infrared (a), NUV (b) and FUV (c) wavebands at around ∼17:00 UT measured by CYRA and IRIS, respectively. The over-plotted curves are the line spectra marked by a cyan line on the left-hand side of each image. The main lines are labeled and indicated by magenta vertical ticks.

Source: Li & Yang et al., 2019a

Data Reduction and Spectroscopic Diagnostic with infrared lines GST/CYRA observed the sunspot in a quickly raster mode with 13 steps, and the scanned FOV was about 4”.8 × 80”, while the exposure time was ∼40 ms. The 13 slits of CYRA went through the sunspot umbra and penumbra in sequence, as shown in Figure 5.12 (g). Figure 5.13 suggests that each CO molecular line nearby its center is a well

Gaussian profile. Thus, I applied a single Gaussian fit to each line profile of CO molecule and also the telluric atmosphere (see also., Uitenbroek et al. 1994[132]). Then the Doppler velocity, line width and intensity of two CO molecular and one telluric lines can be estimated.

Figures 5.14 and 5.15 present the single Gaussian fitting results from the GST/CYRA spectroscopic observations. Figure 5.14 shows the time-distance images along the CYRA scanned direction. In other words, the y-axis is perpendicular to the slits of CYRA, and its length is roughly 4”.8. It can be seen from panels (a) and (b) that the Doppler velocities of CO molecular lines are a little small, which are roughly §1 km s¡1. They are characterized by a series of vertical slashes which are changing from red shifts to blue shifts, including the strong line of CO 3-2 R14 and the weak CO 7-6 R67 line. Notice that the short time disturbances near ∼17:04 UT, ∼17:10 UT, ∼17:20 UT correspond to the time when the image stabilization system does not work. These repeating dynamical behaviors can be considered as the quasi-periodic oscillations of sunspot. The oscillation periods in Doppler shifts can be determined from the numbers of red patterns, which are roughly 5 minutes in both CO 3-2 R14 and CO 7-6 R67 lines. Panel (c) shows that the line width of CO 3-2 R14 exhibits weak oscillations with similar periods as its Doppler velocity. But the line width of CO 7-6 R67 does not display any clearly signatures of quasi-periodic oscillations, as shown in panel (f). Panels (e)-(g) plots the time-distance images of radiation intensity from CO 3-2 R14 and 7-6 R67 lines, as well as the infrared continuum spectrum. They exhibit very weak signatures of quasi-periodic oscillations, but their periods are impossible to be identified by the naked eyes. Finally, the time-distance image of Doppler velocity from telluric line is given in panel (h), which also has not any oscillation behaviors. This also confirms that the quasi-periodic oscillations are indeed from the Sun, but not from the CYRA instruments or Earth’s atmosphere.

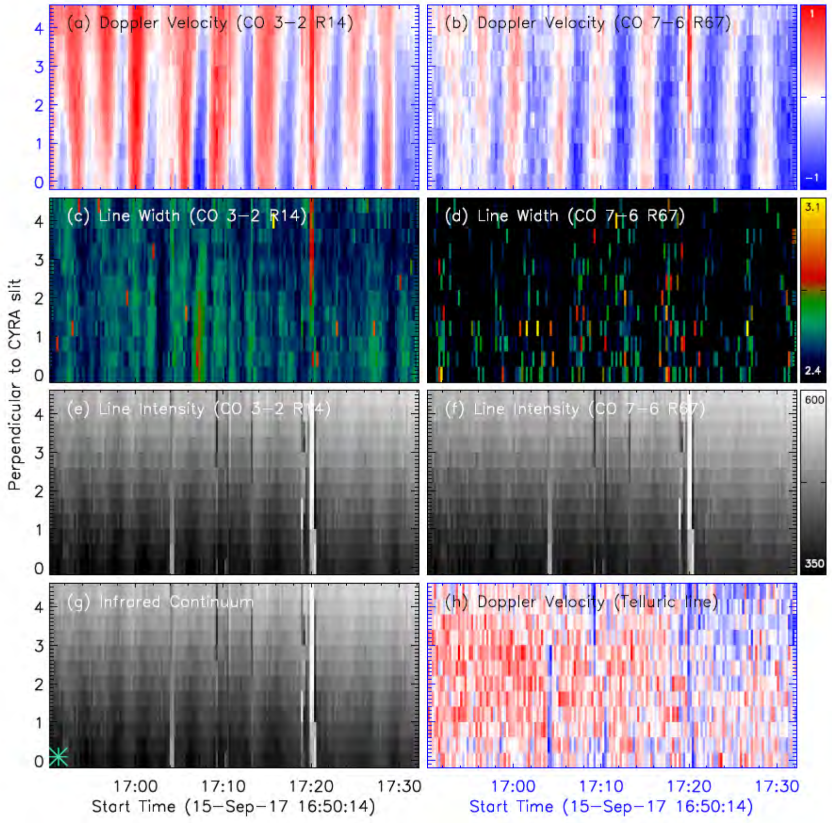

Figure 5.14 Time-distance images of Doppler velocity, line width, and intensity in CO 3-2 R14, CO 7-6 R67, infrared continuum spectrum, and telluric lines, respectively. The y-axis is perpendicular to the slits of CYRA. The cyan $*$ symbol marks the start point in y-axis, which is same as that in Figure 5.12 (g).

Source: Li & Yang et al., 2019a

To further investigate the sunspot oscillations, I also plot the time-distance images along the first slit of CYRA, as shown in Figure 5.15. Y-axis is parallel to the slit direction between about 18” × 68”. The Doppler velocity of CO 3-2 R14 exhibits pronounced oscillations that change from red shifts to blue shifts, as shown in panel (a). The Doppler shift oscillations show two distinguish periods, one is ∼5 minutes at the slit positions nearby 30” and 55”, another one is ∼3 minutes at the slit positions around 40”. Considering the slit positions, I can conclude that the 3-minute oscillations appear at sunspot umbra, while the 5-minute oscillations tend to take place at sunspot penumbra. On the other hand, panel (b) shows that the

Doppler velocity of CO 7-6 R67 has weak oscillations with a period of roughly ∼5 minutes at sunspot umbra and penumbra. The line width of CO 3-2 R14 has a weak behavior of quasi-periodic oscillations at sunspot umbra nearby 4000, and its period is roughly 3 minutes, but the 5-minute oscillations are not found at sunspot penumbra, as shown in panel (c). The 5-minute oscillations are impossible to be identified by naked eyes in the line width and intensity of CO 7-6 R67, as seen in panels (d) and (f). Panels (e) and (g) show that there are also not any apparent oscillations in the radiation intensity of CO 3-2 R14 and infrared continuum spectrum at sunspot umbra, i.e., nearby 40". I finally plot the time-distance image of the Doppler velocity in telluric line, which also has not any signature of quasi-periodic oscillations, as shown in panel (h). All these observational results agree with previous findings in Figure 5.14.

Spectroscopic Observations in NUV IRIS measured the sunspot in a "2-step raster" mode between 16:40:15 UT and 18:01:59 UT. The spectrograph aboard IRIS covered a small FOV of around 2" × 119", with an exposure time of ∼8 s. Luckily, the slits of IRIS crossed nearly the sunspot center, and the second slit (blue solid line in Figure 5.12) was crisscross with the first slit of CYRA (red solid line in Figure 5.12) at sunspot umbra, as indicated by the cyan ∗ symbol in Figure 5.12 (g). So, the IRIS spectra from its second slit were used to investigate the sunspot oscillations, i.e., Mg II H (2803.53 Å) & K (2796.35 Å), and Si IV 1393.76 ÅṪhe double resonance lines of Mg II H & K are usually optically thick in solar spectrum, and their line profiles often exhibit central reversals at line cores (Leenaarts et al. 2013a,b[133, 134]; Cheng et al. 2015[135]). However, the Mg II H & K lines at sunspot do not appear the prominent central reversals of line cores (see., Tian et al. 2014[105]; Zhang et al. 2017[64]). Figure 5.13 (b) shows the line profiles of Mg II H & K lines at sunspot umbra, and their line cores are not central reversals, but they are also non-Gaussian

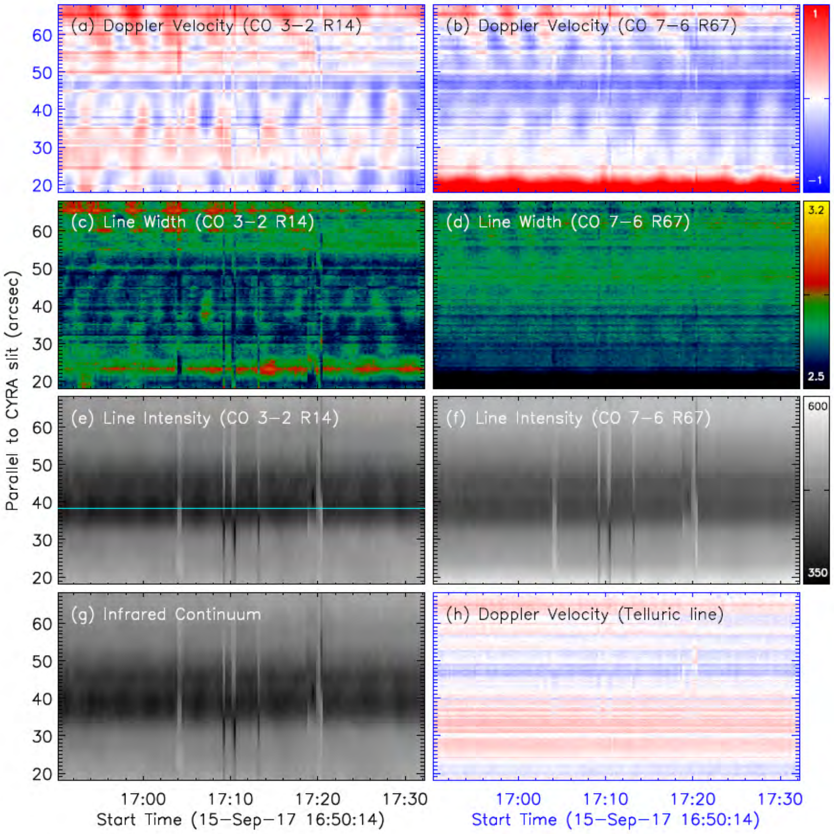

Figure 5.15 Time-distance images along the first CYRA slit (a red solid line in Figure 5.12) of Doppler velocity, line width, and intensity in CO 3-2 R14, CO 7-6 R67, infrared continuum spectrum, and telluric lines, respectively. The y-axis is parallel to the slits of CYRA. A horizontal cyan line in panel (e) outline the umbral position to perform the FFT analysis in Figure 5.20.

Source: Li & Yang et al., 2019a

profiles. Therefore, the moment analysis method but not the single Gaussian fit is applied to estimate the Doppler velocity, line width and intensity of Mg II H & K (see detail in Li et al. 2017[136]). Figure 5.16 shows the time-distance images of Doppler velocity (a, b), line intensity (c, d) and line width (e, f) for Mg II H & K, respectively. Here, the y-axis is parallel to the slits of IRIS (blue lines) with a length of ∼50” between around -1”∼49” along solar-Y direction. The Doppler velocities of Mg II H & K lines at sunspot umbra nearby y ∼20” exhibit pronounced oscillations with a quasi-period of around three minutes. They are characterized by a group of repeating oblique streaks, which are changing from red shifts to blue shifts. The oblique streaks always appear as pairs, propagate with bi-direction and eventually become invisible at the umbral-penumbral boundary, as marked by the green arrows as an example. On the other hand, the sunspot penumbra does not show any signature of Doppler shift oscillations, such as the positions of around y ∼10" and y ∼35". The line intensity and width show the same oscillation behaviors as Doppler velocity. For example, the quasi-periodic oscillations with a period of roughly 3 minutes are identified as the repeating oblique slashes at sunspot umbra, which also show the propagation movement with bi-direction and gradually disappear when they reach the outer umbral boundary. The propagation speeds are also estimated, which are roughly 35 km s^{-1} and 45 km s^{-1}, respectively. But I do not find any clearly signature of oscillations at sunspot penumbra. I also notice that the light bridge of sunspot is brighter and broader than the sunspot umbra, as shown in panels (c)∼(f). However, it is hard to tell whether there are any oscillations here due to the saturated effects, especially for the line intensity at the light bridge. Figure 5.13 (c) has demonstrated that the signal-to-noise ratios of Si IV 1393.76 Å in most positions of sunspot is low, so I do not show their fitting or moment results.

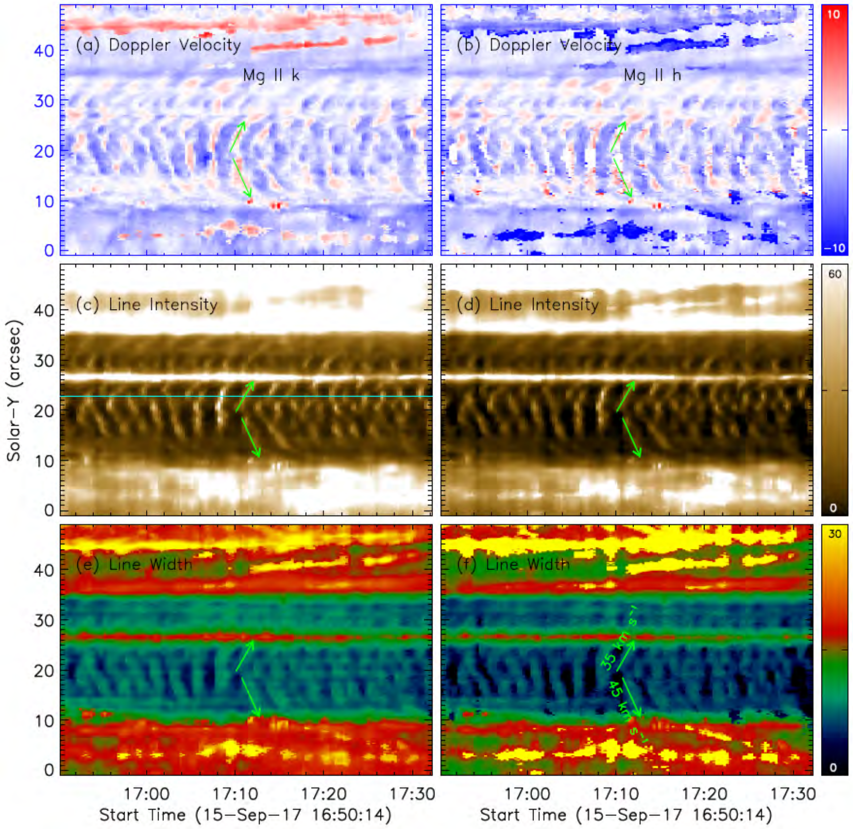

Figure 5.16 Time-distance images along the second slit of IRIS (a blue solid line Figure 5.12) of Doppler velocity, line width, and intensity in Mg II k and h lines, respectively. A horizontal cyan line in panel (c) outline the umbral position to perform the FFT analysis in Figure 5.20 The green arrows indicate a pair of umbral waves.

Source: Li & Yang et al., 2019a

Imaging Diagnostic Using SJI and AIA observations Figure 5.17 shows the time-distance images from imaging observations measured by IRIS/SJI and SDO/AIA in NUV and UV wavebands. The y-axis is parallel to the IRIS slit direction (Solar-Y direction) and takes the region nearby the second slit, as indicated by the blue solid line in Figure 5.12 (g). Panels (a) presents the intensity image derived from SJI 2796 Å observations, while panels (b) shows the detrended image by removing a four-minute running average (see., Wang et al. 2009; Tian et al. 2012; Li et al. 2018). They all exhibit the quasi-periodic oscillations at sunspot umbra (i.e., around y∼20”), which are characterized by a series of repeating oblique streaks with bi-direction, and their oscillation period is estimated to roughly 3 minutes. In other regions, such as sunspot penumbra nearby y $\approx$ 10" and y $\approx$ 35", there are not any apparent oscillation behaviors, including the intensity and detrended images. The observational results derived from SJI 2796 Å images are consistent with these detected by the double Mg II k & h lines in Figure 5.16.

Figure 5.17 (c)$\sim$(f) present the intensity and detrended images in AIA 1700 Å and 1600 Å, respectively. I can not find any obviously signature of quasi-periodic oscillations in the intensity images, no matter at sunspot umbra or sunspot penumbra, as shown in panels (c) and (e). However, the over-plotted light curves of AIA UV intensities derived from the sunspot umbra (y $\approx$ 23") appear a series of repeating peaks, which might be considered as quasi-periodic oscillations. Moreover, the numbers of peaks in AIA 1600 Å light curve are more than these in AIA 1700 Å, suggesting a short period in AIA 1600 Å at sunspot umbra. Then, their detrended images after removing a four-minute running average are plotted in panels (d) and (f), both of which show no apparently signature of quasi-periodic oscillations at sunspot umbra, i.e., around y $\approx$ 20". On the other hand, a weak behavior of oscillations with a period of roughly 5 minutes can be seen at sunspot penumbra (such as nearby y $\approx$ 10" and y $\approx$ 35") in both AIA 1700 Å and 1600 Å. Here, the penumbral-photospheric boundaries are marked by two purple lines.The quasi-periodic oscillations are characterized by a series of oblique slashes, indicating a propagation motion. Their apparent speeds can be estimated to 20 km s_{-1}, as shown by the magenta arrows. Finally, I want to stress that the light bridge can be seen in these images. It displays as a bright and horizontal strip at the positions of nearby y $\approx$ 26" in panels (c) and (e), but exhibits as a group of repeating bright and dark kernels along a horizontal direction nearby y $\approx$ 26" in panels (d) and (f).

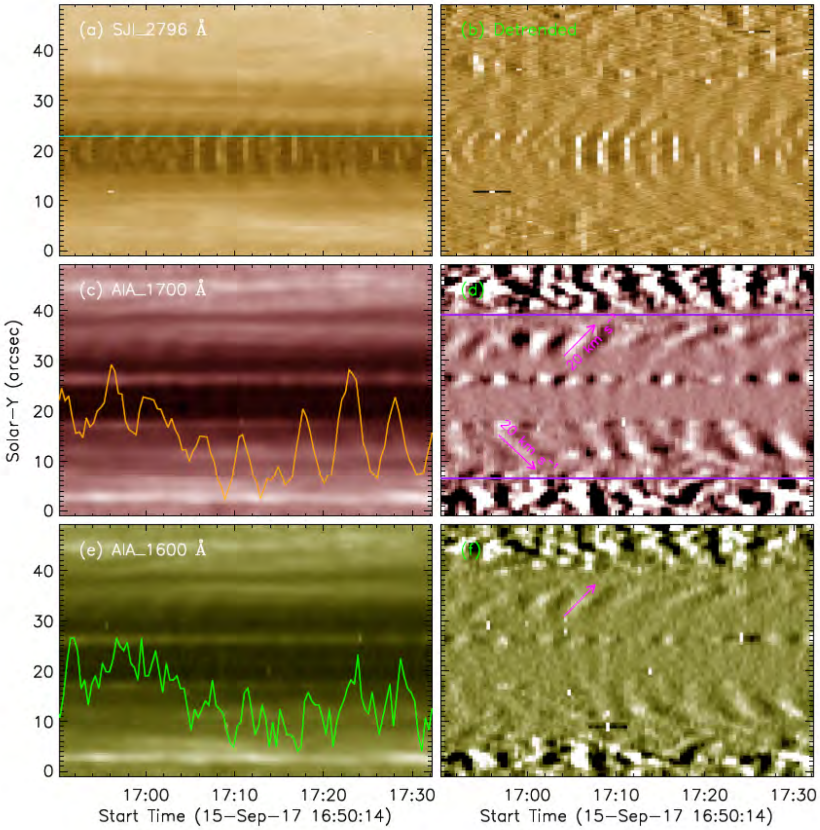

Figure 5.17 Time-distance images along the second slit of IRIS (a blue solid line Figure 5.12) in SJI 2796 Å, AIA 1700 Å and 1600 Å, respectively. The over-plotted curves in panels (c) and (e) are the UV intensity at the umbral position marked with a horizontal cyan line in panel (a), which are used to perform the FFT analysis in Figure 5.20. The magenta arrows indicate the penumbral waves, while the double purple lines in panel (d) outline the penumbral-photospheric boundaries.

Source: Li & Yang et al., 2019a

Figure 5.18 plots the time-wavelength images from CYRA and IRIS spectra in solar infrared, NUV and FUV passbands at one site (x ≈ -67", y ≈ 23") of sunspot umbra, as indicated by the cyan ∗ symbol in Figure 5.12. Panel (a) presents the spectrum of CO 3-2 R14 line at the first slit (red solid line in Figure 5.12) of CYRA. The line-center shift can reach nearly ∼3 km s_{-1}, but the signature of quasi-periodic oscillations is impossible to be identified by naked eyes. This is also explain the weak oscillation features in radiation intensity of CO molecular lines in Figures 5.14 and 5.15. Panel (b) and (c) display the Mg II k and Si IV 1393.76 Å spectra at the second slit (a blue solid line in Figure 5.12) of IRIS. Both of these two spectral lines are characterized by a series of slashes. However, the slashes of Mg II k line are composed of a series of bright vertical slices and faint oblique strips, while these of Si IV 1393.76 Å line are a group of repeating bright oblique strips. In other words, the line intensity enhancement of Mg II k occurs before the maximum speed of blue shifts. But the maximum line intensity of Si IV 1393.76 Å takes place slightly later than its maximum blue shift. This is considered as the spectroscopic signature of shock (Lites 1986[102]; Rouppe van der Voort et al. 2003 [116]; Centeno et al. 2006[137]; Bard & Carlsson 2010[138]). The different behaviors maybe due to the fact that the optical thickness of Mg II k line is much deeper than that of the Si IV 1393.76 Å line (Tian et al. 2014[105]). The over-plotted light curve in panel (c) is the time series of line intensity in Si IV 1393.76 Å integrated over between ±20 km s_{-1}, and it is used to perform the FFT analysis in Figure 5.20.

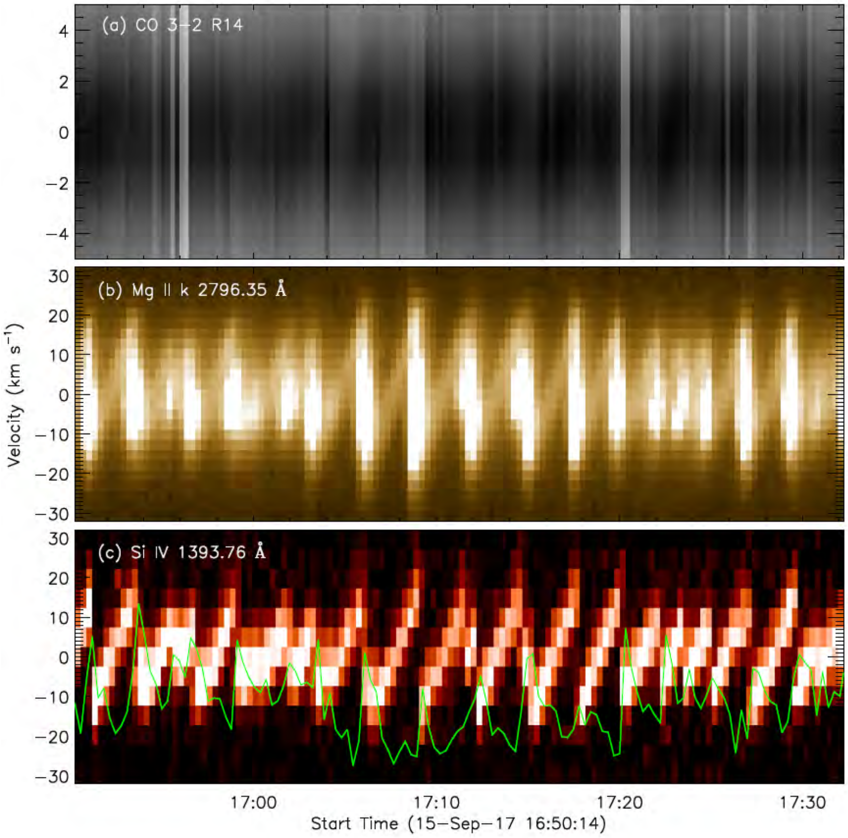

Figure 5.18 Time-wavelength images at one position of sunspot umbra (a cyan $*$ symbol in Figure 5.12) in the CO 3-2 R14, Mg II K, and Si IV lines, respectively. The over-plotted light curve in panel (c) is the line intensity of Si IV integrated over between ∼20 km s^{-1}, which is used to perform the FFT analysis in Figure 5.20.

Source: Li & Yang et al., 2019a

Detrended Light Curves and FFT Power Spectra To look closely at the periods of sunspot oscillations, in particular the umbral oscillations, I extract the light curves at one position of sunspot umbra, as indicated by the cyan $*$ symbol and the horizontal cyan line in Figures 5.12, 5.15-5.17. And then, the detrended light curves are derived by subtracting a four-minute running average (Tian et al. 2012[139]; Li et al. 2018[140]). Figure 5.19 shows the detrended light curves compared with their peak values of the original light curves, including the Doppler velocity (a) in two CO molecular and Mg II k lines, the line width (b) in CO 3-2 R14 & Mg II K lines, the line intensity (c) in Mg II K & Si IV lines, and also the UV intensity (c) in AIA 1600 Å & 1700 Å. It can be seen that the oscillation amplitudes of Doppler velocity are very large, up to 50% in most regions. Therefore, their oscillations can be clearly seen in the time-distance image, as shown in Figures 3∼5. On the other hand, the oscillation amplitudes of UV intensity in AIA 1600 Å & 1700 Å are no more than 5%, indicating small-amplitude oscillations superimposed on strong background emissions. So, it is hard to identify these small-amplitude oscillations (see, Figure 5.17) only by naked eyes. Moreover, the duration of most peaks in AIA 1600 Å is shorter than that in AIA 1700 Å which suggest that the oscillation period in AIA 1600 Å could be short.

To look closely these periods, I then perform the fast Fourier transform (FFT) analysis for the detrended light curves using the Lomb-Scargle periodogram (Scargle 1982[141]; Yuan et al. 2011[142]). Figure 5.20 shows their normalized FFT power spectra, and a horizontal magenta line in each panel represents the 99.99% confidence level defined by Horne & Baliunas (1986[143]). The dominant period can be derived from the peak value of FFT power spectra, while an error bar is calculated from both the width of spectral peak in FFT spectrum and the discreetness of the Fourier frequency grid (Li & Zhang 2017[136]). Finally, the dominant periods with an error bar are determined in multiple channels.

The Doppler velocity of the weak CO 7-6 R67 line shows a long period of ∼4.7 ±0.91 minutes. Double oscillation periods are derived from the Doppler velocity of the strong CO 3-2 R14 line, i.e., a long period of ∼4.7 ±0.88 minutes and a short period of ∼3.3 ±0.51 minutes. But the line width of strong CO 3-2 R14 line exhibits only one short period of ∼3.3 ±0.44 minutes. The long period of ∼4.2 ±0.71 minutes can also be found in AIA 1700 Å radiation intensity. While a short period of ∼3.1 minutes is identified in the line profiles of Mg II k, such as the Doppler velocity (±0.39 minutes), line width (±0.43 minutes) and intensity (±0.36 minutes). Finally, the radiation intensities of Si IV 1393.76 Å line and AIA 1600 Å image are found to be oscillated with much shorter periods, which are ~2.9 ±0.29 minutes and ~2.8 ±0.29 minutes, respectively. Notice that the periods are derived from a same location at sunspot umbra, as marked by the cyan $*$ symbol in Figure 5.12 (g).

Cross-correlation Analysis Figure 5.19 shows that the detrended light curves in different wavebands seems to appear the phase shifts. To determine their phase shifts, the cross-correlation analysis (Tian et al. 2016[144]; Li et al. 2018[140]) is applied to investigate the time lags, as shown in Figure 5.21. Panel (a) presents the cross-correlation results in Doppler velocities between Mg II K and two CO molecular lines. A maximum correlation coefficient (cc.) between Mg II K and CO 3-2 R14 lines (cyan line) is found at the time lag of around -2 minutes, implying a big phase shift between them. It can be seen that the black and cyan curves reach peak cc. at a little different time such as roughly 0.5 minutes, suggesting a small phase shift between two CO molecular lines. Panel (b) displays the time lags in radiation intensity in multiple wavelengths. The time lag (black line) between Mg II K and Si IV line intensities is nearly 0.5 minutes, and the similar time lag (magenta line) can be found between Mg II k line intensity and AIA 1600 Å intensity. This fact suggests a small phase shift between Mg II K and Si IV lines (or AIA 1600 Å), but almost no phase shift between Si IV line and AIA 1600 Å. On the other hand, the time lag between Mg II k line and AIA 1700 Å is nearly 2.5 minuets (green line), indicating a big phase shift between them. This time lag is very close to that in panel (a), which implies a small phase shift between CO molecular lines and AIA 1700 Å. Noting that all these cross-correlation results are from a same position, i.e., sunspot umbra.

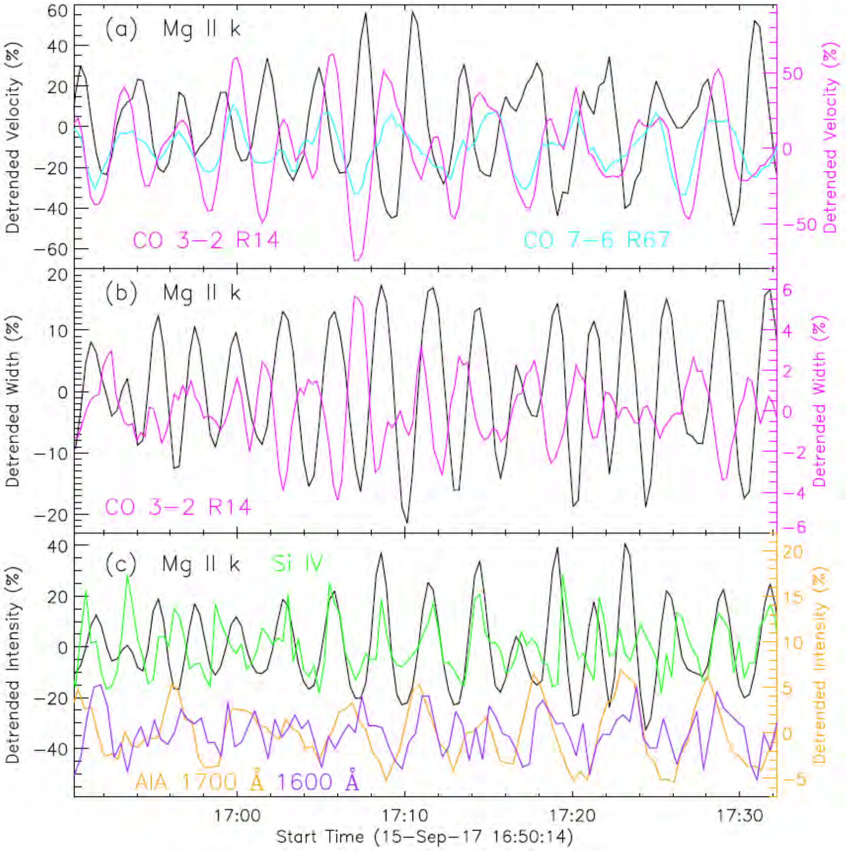

Figure 5.19 Detrended light curves derived from a same umbral position, as marked by the cyan ∗ symbol in Figure 5.12 (g). Panel (a): Detrended Doppler velocity in Mg II k and two CO molecular lines. Panel (b): Detrended line width in Mg II K and CO 3-2 R14 lines. Panel (c): Detrended intensity in Mg II k & Si IV 1393.76 Å lines, and AIA 1600 Å, 1700 Å.

Source: Li & Yang et al., 2019a

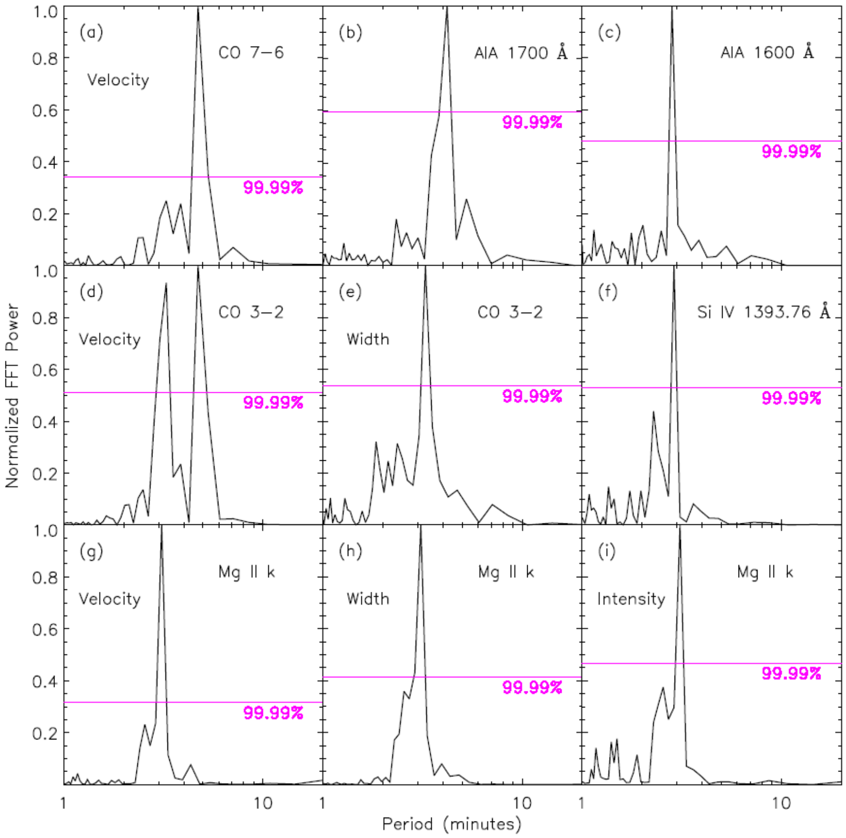

Figure 5.20 Normalized FFT power spectra of the detrended light curves derived from sunspot umbra, as marked by the horizontal cyan line in Figures 5.15 - 5.17. A horizontal magenta line in each panel indicates the 99.99% confidence level.

Discussion Using the spectroscopic observations in solar infrared and NUV bands measured by GST/CYRA and IRIS, I obtain the line profiles of two CO molecular lines, i.e., CO 3-2 R14 and 7-6 R67, as well as one telluric line and double Mg II H & K lines. The weak line of CO 7-6 R67 exhibits only one oscillation period of nearly five minutes at sunspot, including umbra and penumbra. This oscillation phenomenon can be clearly seen in Doppler velocity, but not found in line width and intensity (Figure 5.14 and Figure 5.15). However, the strong CO 3-2 R14 line shows a complex oscillation behavior. At sunspot penumbra, an oscillation period of around five minutes is found, which is similar to that of the weak CO 7-6 R67 line. On the other hand, double periods are detected at sunspot umbra, which are nearly five minutes and roughly 3 minutes (Figure 5.20), respectively. The double oscillation periods indicate that the strong CO 3-2 R14 line contain two-layer radiation on the Sun, i.e., the upper photosphere and temperature minimum region (Uitenbroek 2000[126]; Ayres et al. 2006[127]). These oscillations are strong in Doppler velocity, weak in line width, and very weak or even not visible in line intensity, as can be seen in Figure 5.14 and Figure 5.15. Those oscillations are not seen in telluric line, suggesting that they are from the sunspot but not from the Earth' atmosphere or the CYRA instrument. The line profiles of Mg II H & K lines also show the typical 3-minute oscillations at sunspot umbra, such as the Doppler velocity, line intensity and width, as can be seen in Figure 5.16. However, there is no pronounced signature of oscillations at sunspot penumbra. The typical 3-minute oscillations at sunspot umbra can also be seen in SJI 2796 Å images (upper panels in Figure 5.17), which mainly contain the Mg II k line emission (De Pontieu et al. 2014). The primarily 5-minute oscillations at sunspot penumbra could be found in AIA 1700 Å detrended image, but no clearly oscillations are identified by naked eyes at sunspot umbra in AIA 1600 Å and 1700 Å, as shown in Figure 5.17. In this dissertation, the quasi-periodic oscillations at sunspot umbra are studied in details, since their oscillation periods are complex and can be seen in both solar infrared and NUV/FUV lines, as well as the NUV/UV intensity.

An interesting aspect is that the oscillation periods at sunspot umbra decrease with the formation height of spectral lines, as shown in Figure 5.20. In the lower solar atmosphere, i.e., photosphere, a quasi-period of nearly 5 minutes can be clearly seen in the Doppler velocity of CO 3-2 R14 and 7-6 R67 lines and AIA 1700 Å images. This is consistent with previous observations in white light images or continuum spectrum (Beckers & Schultz 1972[90]; Lites 1988[91]; Nagashima et al. 2007[110]; Yuan et al. 2014b[111]; Su et al. 2016[112]), and might be considered as the solar p-mode waves (Thomas 1985[92]; Bogdan 2000[93]; Solanki 2003[35]). In the middle layers of solar atmosphere, such as chromosphere and transition region, a quasi-period of roughly 3 minutes are found in the line profiles of Mg II H & H and Si IV 1393.76 Å, as well as the SJI 2796 Å and AIA 1600Å images. Meanwhile, the chromospheric line shows a period of ∼3.1 minutes, while the transition region line or images display a period of ∼2.9/2.8 minutes. Moreover, a short time lag of nearly 0.5 minute can be found between the chromospheric (Mg II K) and transition region (Si IV 1393.76 Å) lines, as shown in Figure 5.21 (b). All these observational facts imply a little decreased periods from chromosphere to transition region. This observational results agree well with previous findings in UV/infrared lines or images at sunspot, particularly in the sunspot center. And they are explained as the resonant modes of sunspot oscillations. I also detect a period of ∼3.3 minutes in the Doppler velocity and line with of CO 3-2 R14, and it is believed to provide the information in the temperature minimum region, where is overlying photosphere and underlying chromosphere. On the other hand, a long time lag of about two minutes are observed between the Mg II K and CO molecular lines, as can be seen in Figure 5.21 (a). This observational facts suggest that the 3-minute oscillations at sunspot umbra come from the temperature minimum region and could propagate to the transition region, which support the interpretation of propagating waves above sunspots originate from the lower solar atmosphere (De Moortel et al. 2002[94]; O'Shea et al. 2002[95]; Brynildsen et al. 2004[96]).

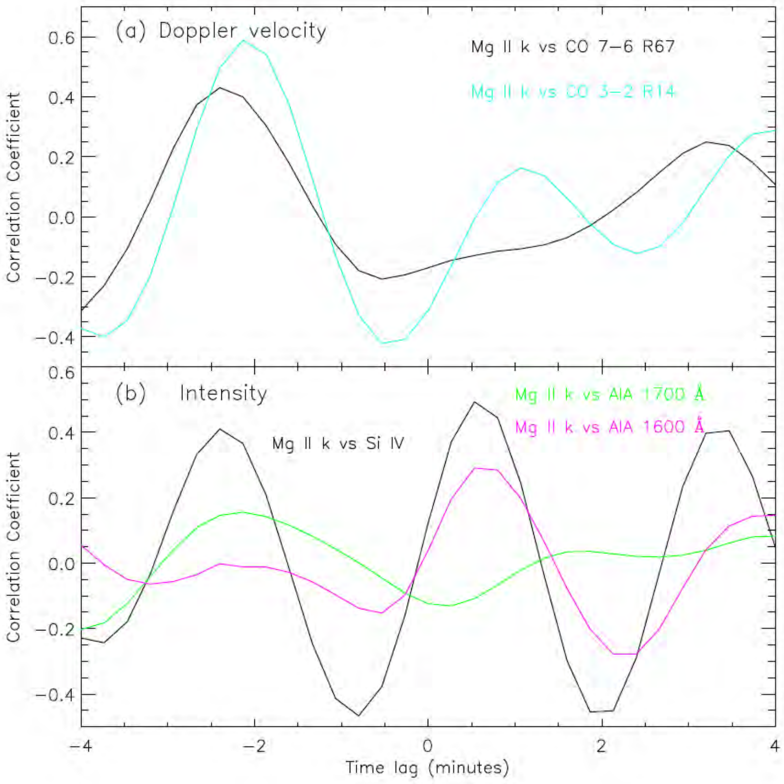

Figure 5.21 Correlation coefficients between two parameters as a function of time lag, such as the Doppler velocity (panel a) in Mg II K and two CO molecular lines, the radiation intensity (panel b) in Mg II K & Si IV 1393.76 Å lines, and AIA 1600 Å & 1700 Å.

Source: Li & Yang et al., 2019a

Figure 5.22 shows the diagram of outer solar atmosphere based on the classical layered paradigm, which is a plane-parallel stratification. According to the oscillation periods at sunspot umbra, the formation height of spectral lines and imaging channels can be determined, as listed in the right-hand side of Figure 5.22. In this observation, only the strong CO 3-2 R14 line exhibits double periods of ~4.7 minutes and ~3.3 minutes at sunspot umbra, indicating it strides over two layers of lower solar atmosphere, varying from photosphere to temperature minimum (Uitenbroek 2000; Ayres et al. 2006), as outlined with two magenta arrows. The weak CO 7-6 R67 line shows only one long period of ∼4.7 minutes at sunspot umbra, which is roughly close to the five-minute photospheric oscillations (Beckers & Schultz 1972; Lites 1988), supporting that it is formed in photosphere. Both Mg II H & H lines and SJI 2796 Å image show a short period of ∼3.1 minutes, while the Si IV 1393.96 Å line displays a much shorter period of ∼2.9 minutes, confirming that they are formed in the chromosphere and transition region, respectively (De Pontieu et al. 2014). Usually, AIA 1700 Å radiation is thought to be emitted from photosphere and temperature minimum region (Lemen et al. 2012). In this observation, AIA 1700 Å intensity at sunspot umbra shows a long period of ∼4.2 minutes, implying it is dominated by the photospheric emissions. On the other hand, AIA 1600 Å emission is generally composed of both photospheric continuum and the C IV line emission in transition region (Lemen et al. 2012). Recently observations also showed that photospheric continuum emission dominates in plage region (Simoes et al. 2019), and the AIA 1600 Å and 1700 Å images in Figure 5.12 (a) and (b) are almost similarity in plage region. So, the contribution of the photospheric continuum cannot be ignored in AIA 1600 Å emissions in plage region. However, it is hard to tell that if the photospheric continuum dominates the AIA 1600 Å emission at sunspot umbra, because that the umbral oscillations with a short period of ∼2.8 minutes are detected in AIA 1600 Å intensity. Moreover, the big phase shift between AIA 1600 Å and 1700 Å intensities (Figure 5.21) suggests that they are formed in different heights. Therefore, AIA 1600 Å emissions are most likely from transition region at umbra, at least in this observation. But it should be mentioned that this is still an open issue, since only one example is given here. Finally, the multiple periods at sunspot umbra indicate the layered atmosphere on the Sun, while the double periods in CO 3-2 R14 line suggest that the outer solar atmosphere is not the strict hierarchy of distinct layers (Penn 2014[6]). It is a little pity that the periods of sunspot oscillations in high solar atmosphere (corona) are not obtained, which is due to the absence of spectroscopic observations in coronal lines, as shown in Figure 5.22. It will be discussed in future work.

It is necessary to stress that the sunspot oscillations could be observed along several directions in solar atmosphere. Figures 5.14 and 5.15 demonstrate that the sunspot oscillations at umbra and penumbra can appear in the directions which are perpendicular and parallel to the CYRA slits, including the long period of nearly 5 minutes and the short period of around 3 minutes. On the other hand, the three-minute oscillations at umbra (around y ~ 20") can also be found to be parallel to the slits of IRIS, as can be seen in Figures 5.16 and 5.17 (a)-(b). I can not see any apparent oscillations at umbra in Figure 5.17 (c)~(f), which might be due to their small amplitudes (5%) superimposed on the strong background emissions, as can be seen in Figure 5.19 (c). Conversely, the five-minute oscillations can be seen at penumbrae in panels (d) and (f), such as the region nearby y ~ 10" and y ~ 35". I have demonstrated that the CYRA slits show a roll angle of ~29° with the slits of IRIS, as can be seen in Figure 5.12 (g). Therefore, my observational results suggest that the sunspot oscillations can spread with an arbitrary direction in the outer layers of solar atmosphere but have not a fixed direction.

It is also worthwhile to stress that the running umbral waves in chromosphere are identified in the line profiles of Mg II H & K lines (Figure 5.16), i.e., Doppler velocity, line width and intensity. They are characterized by a series of oblique streaks with bi-direction and eventually disappear at the umbral-penumbral boundary. The apparent speeds are estimated to ~35 km s^{-1} and ~45 km s^{-1}, which are consistent with previous findings about the running umbral waves, i.e., 30~60 km s^{-1} (Kobanov & Makarchik 2004[97]; Liang et al. 2011[98]). However, such running umbral waves are not found in photosphere and temperature minimum region, since the Doppler shift oscillations of CO molecular lines appear as vertical but not oblique slashes (Figures 5.14 and 5.15). Meanwhile, the running penumbral waves are observed in

AIA 1700 Å and 1600 Å, which originatefrom the umbral-penumbral boundary with a propagation speed of roughly 20 km s^{-1}. This agrees with previous observations about the running penumbral waves, which have a slow propagation velocity of 10∼25 km s^{-1} (Zirin & Stein 1972[145]; Tsiropoula et al. 2000[146]; Tziotziou et al. 2002[147]). The similar propagation motions are not found in the line profiles of Mg II H & K and CO molecular lines. Furthermore, the quasi-periods of sunspot oscillations detected by the Doppler velocity of CO 3-2 R14 line are changing from ∼3 minutes at umbra to ∼5 minutes at penumbra, implying that the running umbral waves might be closely related to the penumbral waves (Tziotziou et al. 2006[148];), and their nature could be the magnetoacoustic waves at sunspot (Bloomfield et al. 2007[149]; Su et al. 2016[112]).

The Doppler velocity of both CO molecular lines are around 1 km s^{-1}, but no more than 3 km s^{-1}, as shown in Figure 5.12 - 5.15, and 5.18. These speeds are similar to previous results in photospheric lines, such as the infrared CO molecular lines of 3-2 R14, 4-3 R23, 6-5 R47, 7-6 R68, and also the visible lines of Fe I 5250 Å and 5434 Å, TiO 6496.2 Å. The formation height of CO molecular lines at around 46655 Å is in photosphere or temperature minimum region (Uitenbroek 2000[126]; Ayres et al. 2006[127]), where the density is very high, so the Doppler velocity is as small as ∼1 km s^{-1}. Meanwhile, their formation height is also very deep, which make the oscillation amplitudes of line radiation are difficult to be measured. Therefore, the sunspot oscillations in line width are weak, while the sunspot oscillations in radiation intensity from the CO molecular lines or infrared continuum spectrum are much weaker or even invisible, as can be seen in Figures 5.14 and 5.15. The quasi-periodic oscillations with a period of around three minutes can be easily seen at sunspot umbra in Doppler velocity, line width and intensity of double Mg II H & K lines which formed in chromosphere, as shown in Figures 5.16 and 5.20. Their Doppler velocities are around ∼10 km s^{-1}, and could be as fast as 20 km s^{-1} (Figure 5.18).

This is also consistent with previous findings in chromospheric lines at sunspot umbra (Centeno et al. 2008[104]; Tian et al. 2014[105]; Khomenko & Collados 2015[89]). Although the Si IV 1393.76 Å line in transition region also show a large Doppler velocity, i.e., as high as 20 km s^{-1}, I do not give the moment or fitting results due to their low signal-to-noise ratios at the most positions of the sunspot.

At last, I want to stress that the signature of shock waves can be found in the line profiles of IRIS spectrum, i.e., Mg II k and Si IV 1393.76 Å. Their line cores firstly exhibit a quickly and blue-ward excursion which followed by an increase of line intensity, and then a red-ward but gradual excursion appears. However, the movements of Mg II k and Si IV 1393.76 Å lines are different, such as the maximum values of their line intensities and blue shifts are asynchrony, which is firstly discovered by Tian et al. (2014). Such motions are attributed to the shock waves (Lites 1986; Bard & Carlsson 2010), and they have been observed at sunspots in the chromospheric and transition region lines, i.e., Ca II H and K, He I 10830 Å, O V 629 Å as well as N V 1238 Å, and 1242 Å (Brynildsen et al. 1999; Rouppe van der Voort et al. 2003; Centeno et al. 2006; Felipe et al. 2010). These observations suggest that the 3-minute oscillations in chromosphere and transition region at sunspot umbra are associated with a vertical wave propagation, which may be caused by an upward shock propagation (Gurman 1987; Rouppe van der Voort et al. 2003). However, I do not find the similar movement behaviors in the spectral profiles of CO molecular lines, i.e., the first fast blue-ward excursion and then the red-ward gradual excursion, as shown in Figure 5.18 (a). This might because that the CO molecular lines are mainly formed in photosphere and temperature minimum region, and they are dominated by five-minuet oscillations, which could be the global solar p-mode waves (Thomas 1985[92]; Bogdan 2000[93]; Solanki 2003[35]).

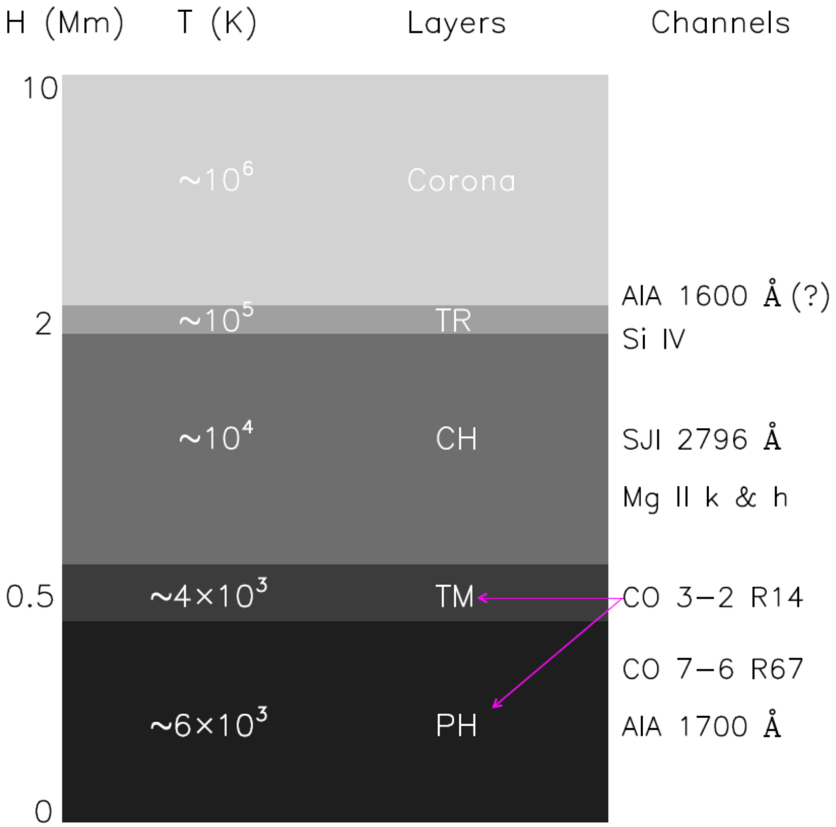

Figure 5.22 Diagram of outer solar atmosphere based on the classical model (Ayres 1998, 2002). Here, height "0" is at τ_{500}=1. The spectral lines and imaging channels used in this dissertation are also listed in the right-hand side. "?" indicates that the height of AIA 1600 Å emissions at the sunspot umbra is still under discussion.

Source: Li & Yang et al., 2019a

Summary Based on the spectroscopic and imaging observations derived from GST/CYRA, IRIS, and SDO/AIA, I investigate the quasi-periodic oscillations in a sunspot between 16:50:14 UT and 17:32:25 UT on 2017 September 15. The primary observational results are summarized as following:

1. The oscillation periods at sunspot umbra decrease with the height of outer solar atmosphere, i.e., nearly 5 minutes in photosphere, and around 3 minutes in temperature minimum region, chromosphere and transition region. And this is also confirmed by the time lags between different parameters.

2. The sunspot oscillations do not show a fixed direction, including the quasi-periodic oscillations at umbra and penumbra.

3. The running umbral waves are detected in chromosphere, which can be clearly seen as bi-directional oblique streaks in Doppler velocity, line width and intensity of Mg II H & K lines, as well as the SJI 2796 Å image. The running penumbral waves are observed in AIA 1700 Å and 1600 Å detrended images, but do not appear in SJI 2796 Å detrended images.

4. The shock waves can be clearly seen in the IRIS lines of Mg II k, and Si IV 1393.76 Å, but failed to be found in the solar infrared CO molecular lines.

5. The typical 5-minutes oscillations at sunspot penumbra could be found in Doppler velocity of CO molecular lines, the detrended images of AIA 1700 Å and 1600 Å. However, they are not observed in the line profiles of Mg II H & K.

5.4.3 Ti I 2231 nm

Thanks to the strong umbra magnetic field, spectral lines are completely Zeeman split, which makes the measurement of umbra field strength relatively simple. However, many other factors, for example, strengthening of line profiles due to neutral species at low umbra temperature, contamination due to stray-light from the surrounding penumbra and plage, and the blending by purely umbra lines, may distort the profiles of some Zeeman sensitive spectral lines. It has been suggested that thermal effects in some visible lines combined with their weaker Zeeman splitting have produced erroneous measurements, and that the field strength distribution measured by the IR lines is more representative of the true solar magnetic fields (Collados et al, 2005). Fortunately, the multiplet of Ti I lines at 2.2 microns are not affected by those problems above. Table 5.3 shows the magnetic sensitivities of these Ti I lines.

The Ti I absorption line at 2231 nm is the only Zeeman triplet of the multiplet. It was first found in sunspot in 1974 and it was first used to explore the sunspot

Table 5.3 Titanium Multiplet: Atomic Parameters.

Ion	λ [nm]	Transition	g$_{eff}$	χ_e [eV]	$\log gf$
Ti I	2231.061	$a\,^5P_1$ - $z\,^5D^o_0$	2.500	1.73	-2.21
Ti I	2221.122	$a\,^5P_1$ - $z\,^5D^o_1$	2.000	1.73	-1.85
Ti I	2223.291	$a\,^5P_2$ - $z\,^5D^o_2$	1.667	1.74	-1.74
Ti I	2227.407	$a\,^5P_3$ - $z\,^5D^o_3$	1.583	1.75	-1.84
Ti I	2189.738	$a\,^5P_1$ - $z\,^5D^o_3$	1.167	1.74	-1.53

Source: Rüedi, A&A, 1998[150].

magnetic fields in 1998 (Rüedi, A&A, 1998[150]). Benefit from the relative long wavelength and large effective Landé factor, its magnetic sensitivity, $\lambda \cdot g_{eff}$, is 5578 nm, which is 18% larger than the value of 4695 nm for the widely used extremely sensitive Fe I 1565 nm line.

Another very important advantage for the Ti multiplet at 2.2 microns is its temperature response. Its relative line depth peaks around 4000 K, which is the temperature of sunspot umbra. Thus, these line only shows in the cool sunspots umbra region and the observation will not get influenced by stray light from the surrounding structures.

We have developed the a single beam poloarimeter with rotating plate for CYRA to observe polarized solar light. A rotating retarder has been mounted on a movable stage and a frame for the analyzer has been made. In order to observe the polarimetry data, the retarder will move in to the beam and the analyzer will be placed after the retarder. During the observation, the rotating retarder will stay in eight different positions from 0° to 157.5° with 22.5° difference in each position. At 0° position, the optical axis of retarder and the analyzer is aligned and therefore allow all light to transmit. At 90° position, the optical axis of retarder and the analyzer is perpendicular and all light is blocked. 15 frames of image is taken at each position and totally 120 frames will be recorded for each full polarimetry measurement. After demodulation, the full Stokes I/Q/U/V signal will be ready for scientific research.

CHAPTER 6

SUMMARY AND FUTURE WORK

This dissertation researches the infrared solar physics from scientific and instrumentation aspect. With the help of ground-based high-resolution telescope – GST and the advanced optical techniques, high quality infrared observations become possible. By involved in the data reduction for NIRIS as well as the instrumentation development for CYRA, the author has obtained plenty of knowledge and research experience. This study is focused on how the mass and energy transferred from lower solar atmosphere to higher solar atmosphere. Understanding this mass and energy transferring process through the infrared observations is an new path to approach the very important coronal heating problem. In the following, the major results of the presented observational studies are summarized and listed below.

6.1 Major Results and Discussion

Firstly, in the study of counter-streaming motions in active region magnetic loops, high-resolution spectroscopic observation carried out the evidence of mass and energy flows in the interface region from below. The magnetic loops connect two plage regions with opposite polarities. Well aligned He I 10830 Å spectroscopic images and TiO photospheric images shows the hot plasma is pumped up from and drained down to the inter-granule lanes. The plasma flow in small arches seems to be driven by the 5-minute photospheric oscillations and presents no further correspondence in the TR. However, those long arches are possibly driven by magnetic reconnection or siphon effect and are accompanied with obvious brightening in the AIA 304 Å and 171 Å and in other wavelengths with higher temperature.

Secondarily, solar plasma emerges from the bottom of photosphere and brings magnetic field out from the convection zone. The newly emerged highly twisted magnetic flux ropes may reconnect with the pre-exist magnetic field in the solar surface and trigger plasma ejections. The observation in this study is a step forward to understand small-scale magnetic flux emergence and reconnection in a LB. It is the first report of LB granulation presents brightness enhancement due to the corresponding MFE. The chromospheric footpoint of associated Hα fan-shape jets are also witnessed as the reconnection point between the horizontal magnetic field of the new emerging flux and the vertical magnetic field of the existing penumbral flux. Therefore, the mass and energy brought by MFE from the convection zone could be released to chromosphere through magnetic reconnection and jetting activities.

Finally, the study of spectroscopic diagnostic of sunspot oscillation with IR and EUV lines presents how oscillation energy is transferred from photosphere to TR through the the solar temperature minimum. Time lags between the oscillation in each layer are found and oscillation periods are found to be decrease with the height of the solar atmosphere. The MHD waves propagates from the bottom of the solar atmosphere to the interface region, and therefore, brought oscillation energy to higher atmosphere during this process.

Infrared wavelengths brought us various of new information from the solar atmosphere. Based on the results presented above, following conclusions are made. (1) The mass and energy in the solar atmosphere originates from the solar structure below (convection zone). They are brought to the solar surface through emerging process. (2) Mass and energy can be transferred from solar lower atmosphere to solar higher atmosphere by magnetic reconnection and MHD waves. (3) With magnetic reconnection, energy can be transferred to corona in the form of hot plasma ejections and with MHD waves energy may reach to TR in the form of oscillations.

6.2 Foreseeing the Future Work

As a concluding remark to this dissertation, following studies are expected to be done in the future based on the results of previous researches:

Magnetic emergence plays an key role in the energy release and transportation process. To obtain accurate vertical magnetic field data, proper inversion methods should be applied on the observed Stokes profiles. ME code is currently used to inverse the NIRSI data. It runs pretty quick, however, itself has some limitations with its simplified solar atmosphere models. SIR method, takes height gradient of magnetic field and atmospheric temperature into consideration and can fit the asymmetric Stokes profiles, is a widely accepted inversion method. The SIR method should be applied on the NIRIS Stokes profiles. For those MFE event happens in active regions, which are always with strong background magnetic field, two-component inversion should be also include into the inversion code package. Unfortunately, SIR inversion usually need more calculations and more iterations and therefore requires more time to process the whole data set. Up to now, there are not many studies performed with time sequence of SIR inverted vector magnetic field data. Machine Learning, as an popular data reduction method, is possible to solve the conflict [151]. The author is now working with computer scientist in the machine learning field to applied this method on Stokes inversions. I begin with the simple ME code to train the machine and have got decent ME inversion results. In the next step, I will work on the machine learning inversions with SIR code.

CYRA is a promising infrared instrument, which has the potential to release important physics in the solar temperature minimum. Currently, it is ready for intensity observation with CO lines at 4667 nm. Data reduction pipe line and code has been developed. I am now working on CO observations of a group of pores recorded on Sept.11 2018. Interest CO clouds[152] are presented in the observations.

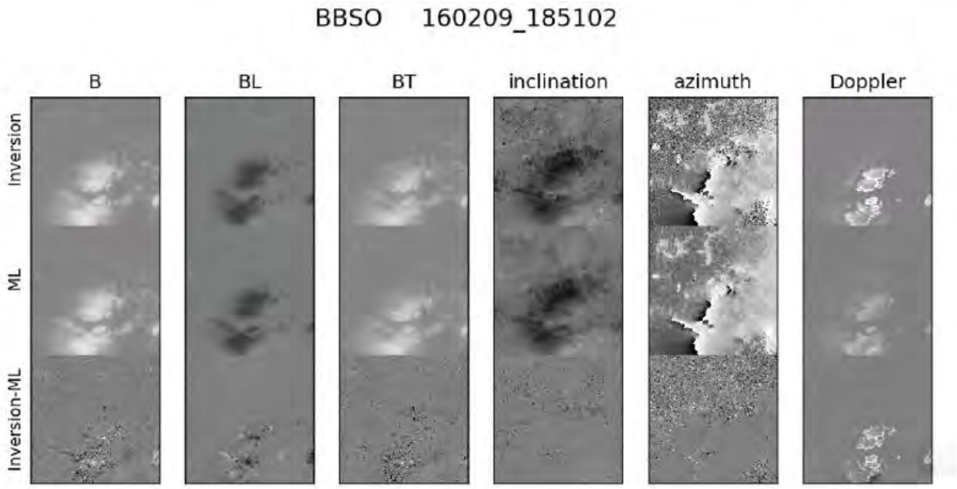

Figure 6.1 Machine learning results of ME inversion.

The mystery of corona heating problem may be hide behind the high-speed chromosphere-TR spicules. Current study of Yurshychyn et al. describes the morphology change of the Hα jet under extremely high temporal-resolution observations. With the help with Hα and He I 10830 Å spectroscopic data obtained by GST, I may find out the driven mechanics of these fast spicules and understand how they bring mass and energy upwards.

(a) Vibration in spectral direction

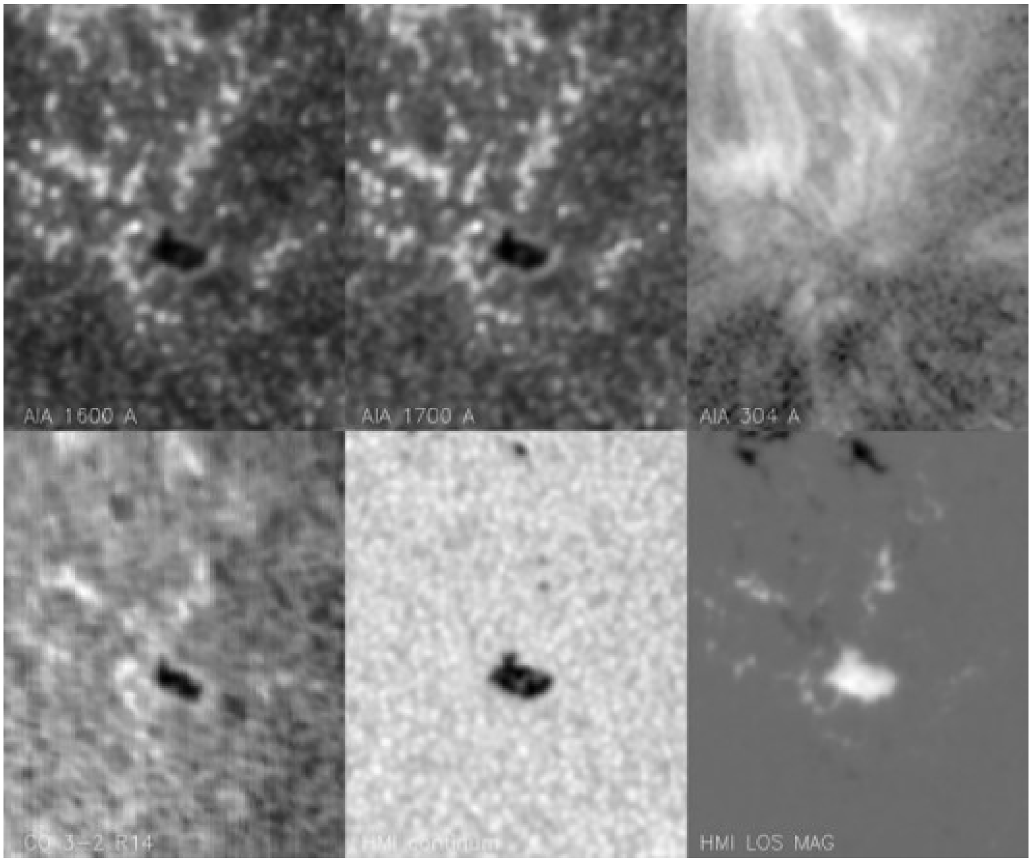

(b) Vibration in spatial direction

Figure 6.2 CYRA observation of pores on Sept. 11 2018

BIBLIOGRAPHY

[1] T. R. Ayres, Co and the temperature structure of the solar atmosphere, in: F.-L. Deubner, J. Christensen-Dalsgaard, D. Kurtz (Eds.), New Eyes to See Inside the Sun and Stars, Vol. 185 of IAU Symposium, 1998, p. 403.

[2] T. R. Ayres, Does the sun have a full-time COmosphere?, The Astrophysical Journal 575 (2) (2002) 1104–1115. doi:10.1086/341428.

[3] V. I. Abramenko, V. B. Yurchyshyn, P. R. Goode, I. N. Kitiashvili, A. G. Kosovichev, Detection of small-scale granular structures in the quiet sun with the new solar telescope, The Astrophysical Journal 756 (2) (2012) L27. doi:10.1088/2041-8205/756/2/l27.

[4] E. Schatzman, A theory of the role of magnetic activity during star formation, Mount Wilson and Palomar Observatory 25 (1962) 18.
URL `http://adsabs.harvard.edu/abs/1962AnAp...25...18S`

[5] E. N. Parker, Nanoflares and the solar x-ray corona, The Astrophysical Journal 330 (1988) 474. doi:10.1086/166485.

[6] M. J. Penn, Infrared solar physics, Living Reviews in Solar Physics 11 (2014). doi:10.12942/lrsp-2014-2.

[7] P. Goode, R. Coulter, N. Gorceix, V. Yurchyshyn, W. Cao, The NST: First results and some lessons for ATST and EST, Astronomische Nachrichten 331 (6) (2010) 620–623. doi:10.1002/asna.201011387.

[8] W. Cao, N. Gorceix, R. Coulter, K. Ahn, T. R. Rimmele, P. R. Goode, Scientific instrumentation for the 1.6 m new solar telescope in big bear, Astronomische Nachrichten 331 (6) (2010) 636–639. doi:10.1002/asna.201011390.

[9] F. Wöger, O. von der Lühe, K. Reardon, Speckle interferometry with adaptive optics corrected solar data, Astronomy & Astrophysics 488 (1) (2008) 375–381. doi:10.1051/0004-6361:200809894.

[10] J. Chae, S. Park, Magnetic activity on the sun revealed by hinode/sot (keynote), in: B. Lites, M. Cheung, T. Magara, J. Mariska, K. Reeves (Eds.), The Second Hinode Science Meeting: Beyond Discovery-Toward Understanding, Vol. 415 of Astronomical Society of the Pacific Conference Series, 2009, p. 101.

[11] B. R. Cobo, J. C. del Toro Iniesta, Inversion of stokes profiles, The Astrophysical Journal 398 (1992) 375. doi:10.1086/171862.

[12] J. Martinez-Sykora, B. D. Pontieu, V. Hansteen, S. W. McIntosh, What do special line profile asymmetries tell us about the solar atmosphere?, The Astrophysical Journal 732 (2) (2011) 84. doi:10.1088/0004-637x/732/2/84.

[13] M. Aschwanden, R. Nightingale, D. Alexander, Evidence for nonuniform heating of coronal loops inferred from multithread modeling ofTRACEData, The Astrophysical Journal 541 (2) (2000) 1059–1077. doi:10.1086/309486.

[14] F. Reale, Coronal loops: Observations and modeling of confined plasma, Living Reviews in Solar Physics 11 (2014). doi:10.12942/lrsp-2014-4.

[15] T. Sakao, R. Kano, N. Narukage, J. Kotoku, T. Bando, E. E. DeLuca, L. L. Lundquist, S. Tsuneta, L. K. Harra, Y. Katsukawa, M. Kubo, H. Hara, K. Matsuzaki, M. Shimojo, J. A. Bookbinder, L. Golub, K. E. Korreck, Y. Su, K. Shibasaki, T. Shimizu, I. Nakatani, Continuous plasma outflows from the edge of a solar active region as a possible source of solar wind, Science 318 (5856) (2007) 1585–1588. doi:10.1126/science.1147292.

[16] H. Hara, . Watanabe, L. K. Harra, J. L. Culhane, P. R. Young, J. T. Mariska, G. A. Doschek, Coronal plasma motions near footpoints of active region loops revealed from spectroscopic observations withHinodeEIS, The Astrophysical Journal 678 (1) (2008) L67–L71. doi:10.1086/588252.

[17] B. D. Pontieu, S. W. McIntosh, Quasi-periodic propagating signals in the solar corona: The signature of magnetoacoustic waves of the high-velocity upflows?, The Astrophysical Journal 722 (2) (2010) 1013–1029. doi:10.1088/0004-637x/722/2/1013.

[18] J. He, E. Marsch, W. Curdt, H. Tian, C. Tu, L. Xia, S. Kamio, Magnetic and spectroscopic properties of supergranular-scale coronal jets and erupting loops in a polar coronal hole, Astronomy and Astrophysics 519 (2010) A49. doi:10.1051/0004-6361/201014709.

[19] H. Tian, S. W. McIntosh, B. D. Pontieu, J. Martínez-Sykora, M. Sechler, X. Wang, Two components of the solar coronal emission revealed by extreme-ultravilet imaging spectroscopic observations, The Astrophysical Journal 738 (1) (2011) 18. doi:10.1088/0004-637x/738/1/18.

[20] H. Tian, S. W. McIntosh, B. D. Pontieu, The spectroscopic signature of quasi-periodic upflows in the active region timeseries, The Astrophysical Journal 727 (2) (2011) L37. doi:10.1088/2041-8205/727/2/l37.

[21] H. Tian, Probing the solar transition region: Current status and future perspectives, Research in Astronomy and Astrophysics 17 (11) (2017) 110. doi:10.1088/1674-4527/17/11/110.

[22] G. W. Pneuman, R. A. Kopp, Downflow in the supergranulation network and its implications for transition region models, Solar Physics 57 (1) (1978) 49–64. doi:10.1007/bf00152043.

[23] A. Winebarger, D. Tripathi, H. E. Mason, G. D. Zanna, Doppler shifts in active region moss using SOHO/SUMER, The Astrophysical Journal 767 (2) (2013) 107. doi:10.1088/0004-637x/767/2/107.

[24] L. Teriaca, D. Banerjee, A. Falchi, J. G. Doyle, M. S. Madjarska, Transition region small-scale dynamics as seen by SUMER on SOHO, Astronomy & Astrophysics 427 (3) (2004) 1065–1074. doi:10.1051/0004-6361:20040503.

[25] X. Yang, W. Cao, H. Ji, P. Hashim, J. Shen, High-resolution spectroscopic imaging of counter-streaming motions in solar active region magnetic loops, The Astrophysical Journal 881 (1) (2019) L25. doi:10.3847/2041-8213/ab365b.

[26] S. Parenti, J. Vial, On the nature of the prominence - corona transition region, Proceedings of the International Astronomical Union 8 (S300) (2013) 69–78. doi:10.1017/s1743921313010764.

[27] H. Ji, W. Cao, P. R. Goode, Observation of ultrafine channels of solar corona heating, The Astrophysical Journal 750 (1) (2012) L25. doi:10.1088/2041-8205/750/1/l25.

[28] J. B. Zirker, O. Engvold, S. F. Martin, Counter-streaming gas flows in solar prominences as evidence for vertical magnetic fields, Nature 396 (6710) (1998) 440–441. doi:10.1038/24798.

[29] Y. Shen, Y. Liu, Y. D. Liu, P. F. Chen, J. Su, Z. Xu, Z. Liu, Fine magnetic structure and origin of counter-streaming mass flows in a quiescent solar prominence, The Astrophysical Journal 814 (1) (2015) L17. doi:10.1088/2041-8205/814/1/l17.

[30] P. Zou, C. Fang, P. F. Chen, K. Yang, Q. Hao, W. Cao, Material supply and magnetic configuration of an active region filament, The Astrophysical Journal 831 (2) (2016) 123. doi:10.3847/0004-637x/831/2/123.

[31] H. Wang, R. Liu, Q. Li, C. Liu, N. Deng, Y. Xu, J. Jing, Y. Wang, W. Cao, Extending counter-streaming motion from an active region filament to a sunspot light bridge, The Astrophysical Journal 852 (1) (2018) L18. doi:10.3847/2041-8213/aaa2f4.

[32] Z. Hong, X. Yang, Y. Wang, K. Ji, H. Ji, W. Cao, Location of energy source for coronal heating on the photosphere, Research in Astronomy and Astrophysics 17 (3) (2017) 25. doi:10.1088/1674-4527/17/3/25.

[33] L. J. November, G. W. Simon, Precise proper-motion measurement of solar granulation, The Astrophysical Journal 333 (1988) 427. doi:10.1086/166758.

[34] C. Torrence, G. P. Compo, A practical guide to wavelet analysis, Bulletin of the American Meteorological Society 79 (1) (1998) 61–78. doi:10.1175/1520-0477(1998)079¡0061:apgtwa¿2.0.co;2.

[35] S. K. Solanki, A. Lagg, J. Woch, N. Krupp, M. Collados, Three-dimensional magnetic field topology in a region of solar coronal heating, Nature 425 (6959) (2003) 692–695. doi:10.1038/nature02035.

[36] Z. Xu, A. Lagg, S. K. Solanki, Magnetic structures of an emerging flux region in the solar photosphere and chromosphere, Astronomy and Astrophysics 520 (2010) A77. doi:10.1051/0004-6361/200913227.

[37] A. Lagg, J. Woch, S. K. Solanki, N. Krupp, Supersonic downflows in the vicinity of a growing pore, Astronomy & Astrophysics 462 (3) (2006) 1147–1155. doi:10.1051/0004-6361:20054700.

[38] S. J. G. Manrique, C. Kuckein, M. Collados, C. Denker, S. K. Solanki, P. Gomory, M. Verma, H. Balthasar, A. Lagg, A. Diercke, Temporal evolution of arch filaments as seen in he 10830 å, Astronomy & Astrophysics 617 (2018) A55. doi:10.1051/0004-6361/201832684.

[39] R. Muller, The fine structure of light-bridges in sunspots, Solar Physics 61 (2) (1979) 297–300. doi:10.1007/bf00150414.

[40] H. Zirin, H. Wang, Flows, flares, and formation of umbrae and light bridges in BBSO region no. 1167, Solar Physics 125 (1) (1990) 45–60. doi:10.1007/bf00154778.

[41] M. Sobotka, J. A. Bonet, M. Vazquez, A high-resolution study of the structure of sunspot light bridges and abnormal granulation, The Astrophysical Journal 426 (1994) 404. doi:10.1086/174076.

[42] A. Lagg, S. K. Solanki, M. van Noort, S. Danilovic, Vigorous convection in a sunspot granular light bridge, Astronomy & Astrophysics 568 (2014) A60. doi:10.1051/0004-6361/201424071.

[43] M. Schüssler, A. Vögler, Magnetoconvection in a sunspot umbra, The Astrophysical Journal 641 (1) (2006) L73–L76. doi:10.1086/503772.

[44] J. Jurčák, V. M. Pillet, M. Sobotka, The magnetic canopy above light bridges, Astronomy & Astrophysics 453 (3) (2006) 1079–1088. doi:10.1051/0004-6361:20054471.

[45] X. Yang, V. Yurchyshyn, K. Ahn, M. Penn, W. Cao, Light bridge brightening and plasma ejection driven by a magnetic flux emergence event, The Astrophysical Journal 886 (1) (2019) 64. doi:10.3847/1538-4357/ab4a7d.

[46] E. Pariat, K. Dalmasse, C. R. DeVore, S. K. Antiochos, J. T. Karpen, Model for straight and helical solar jets, Astronomy & Astrophysics 573 (2015) A130. doi:10.1051/0004-6361/201424209.

[47] E. Pariat, K. Dalmasse, C. R. DeVore, S. K. Antiochos, J. T. Karpen, A model for straight and helical solar jets, Astronomy & Astrophysics 596 (2016) A36. doi:10.1051/0004-6361/201629109.

[48] H. Kurokawa, Surge activity in an emerging magnetic region of the sun, Vistas in Astronomy 31 (1988) 67–71. doi:10.1016/0083-6656(88)90177-8.

[49] H. Kurokawa, G. Kawai, H alpha Surge Activity at the First Stage of Magnetic Flux Emergence, in: H. Zirin, G. Ai, H. Wang (Eds.), IAU Colloq. 141: The Magnetic and Velocity Fields of Solar Active Regions, Vol. 46 of Astronomical Society of the Pacific Conference Series, 1993, p. 507.

[50] T. Yokoyama, K. Shibata, Magnetic reconnection as the origin of x-ray jets and hα surges on the sun, Nature 375 (6526) (1995) 42–44. doi:10.1038/375042a0.

[51] A. Asai, T. T. Ishii, H. Kurokawa, Plasma ejections from a light bridge in a sunspot umbra, The Astrophysical Journal 555 (1) (2001) L65–L68. doi:10.1086/321738.

[52] R. E. Louis, C. Beck, K. Ichimoto, Small-scale chromospheric jets above a sunspot light bridge, Astronomy & Astrophysics 567 (2014) A96. doi:10.1051/0004-6361/201423756.

[53] L. Bharti, T. Rimmele, R. Jain, S. N. A. Jaaffrey, R. N. Smartt, Detection of opposite polarities in a sunspot light bridge: Evidence of low-altitude magnetic reconnection, Monthly Notices of the Royal Astronomical Society 376 (3) (2007) 1291–1295. doi:10.1111/j.1365-2966.2007.11525.x.

[54] R. E. Louis, L. R. B. Rubio, J. de la Cruz Rodríguez, H. Socas-Navarro, A. Ortiz, Small-scale magnetic flux emergence in a sunspot light bridge, Astronomy & Astrophysics 584 (2015) A1. doi:10.1051/0004-6361/201526854.

[55] S. Toriumi, Y. Katsukawa, M. C. M. Cheung, Light bridge in a developing active region. i. observation of light bridge and its dynamic activity phenomena, The Astrophysical Journal 811 (2) (2015) 137. doi:10.1088/0004-637x/811/2/137.

[56] S. Toriumi, M. C. M. Cheung, Y. Katsukawa, Light bridge in a developing active region. ii. numerical simulation of flux emegence and light bridge formation, The Astrophysical Journal 811 (2) (2015) 138. doi:10.1088/0004-637x/811/2/138.

[57] H. Tian, V. Yurchyshyn, H. Peter, S. K. Solanki, P. R. Young, L. Ni, W. Cao, K. Ji, Y. Zhu, J. Zhang, T. Samanta, Y. Song, J. He, L. Wang, Y. Chen, Frequently occurring reconnection jets from sunspot light bridges, The Astrophysical Journal 854 (2) (2018) 92. doi:10.3847/1538-4357/aaa89d.

[58] V. Yurchyshyn, V. Abramenko, A. Kosovichev, P. Goode, High resolution obsevervations of chromopheric jets in sunspot umbra, The Astrophysical Journal 787 (1) (2014) 58. doi:10.1088/0004-637x/787/1/58.

[59] L. Bharti, Fine structure above a light bridge in the transition region and corona, MNRAS 452 (2015) L16–L20. arXiv:1505.02412, doi:10.1093/mnrasl/slv071.

[60] S. Yang, J. Zhang, F. Jiang, Y. Xiang, Oscillating light wall above a sunspot light bridge, The Astrophysical Journal 804 (2) (2015) L27. doi:10.1088/2041-8205/804/2/l27.

[61] Y. Hou, J. Zhang, T. Li, S. Yang, L. Li, X. Li, A solar flare disturbing a light wall above a sunspot light bridge, The Astrophysical Journal 829 (2) (2016) L29. doi:10.3847/2041-8205/829/2/l29.

[62] S. Yang, J. Zhang, R. Erdélyi, Enhancement of a sunspot light wall with external disturbance, The Astrophysical Journal 833 (2) (2016) L18. doi:10.3847/2041-8213/833/2/l18.

[63] D. Song, J. Chae, V. Yurchyshyn, E.-K. Lim, K.-S. Cho, H. Yang, K. Cho, H. Kwak, Chromospheric plasma ejections in a light bridge of a sunspot, The Astrophysical Journal 835 (2) (2017) 240. doi:10.3847/1538-4357/835/2/240.

[64] J. Zhang, H. Tian, J. He, L. Wang, Surge-like oscillations above sunspot light bridges driven by magnetoacoustic shocks, The Astrophysical Journal 838 (1) (2017) 2. doi:10.3847/1538-4357/aa63e8.

[65] Y. Katsukawa, T. E. Berger, K. Ichimoto, B. W. Lites, S. Nagata, T. Shimizu, R. A. Shine, Y. Suematsu, T. D. Tarbell, A. M. Title, S. Tsuneta, Small-scale jetlike features in penumbral chromospheres, Science 318 (5856) (2007) 1594–1597. doi:10.1126/science.1146046.

[66] K. Ichimoto, B. Lites, D. Elmore, Y. Suematsu, S. Tsuneta, Y. Katsukawa, T. Shimizu, R. Shine, T. Tarbell, A. Title, J. Kiyohara, K. Shinoda, G. Card, A. Lecinski, K. Streander, M. Nakagiri, M. Miyashita, M. Noguchi, C. Hoffmann, T. Cruz, Polarization calibration of the solar optical telescope onboard hinode, Solar Physics 249 (2) (2008) 233–261. doi:10.1007/s11207-008-9169-9.

[67] T. Kosugi, K. Matsuzaki, T. Sakao, T. Shimizu, Y. Sone, S. Tachikawa, T. Hashimoto, K. Minesugi, A. Ohnishi, T. Yamada, S. Tsuneta, H. Hara, K. Ichimoto, Y. Suematsu, M. Shimojo, T. Watanabe, S. Shimada, J. M. Davis, L. D. Hill, J. K. Owens, A. M. Title, J. L. Culhane, L. K. Harra, G. A. Doschek, L. Golub, The hinode (solar-b) mission: An overview, Solar Physics 243 (1) (2007) 3–17. doi:10.1007/s11207-007-9014-6.

[68] J. I. Sakai, P. D. Smith, Modeling penumbral microjets by two-fluid simulations, The Astrophysical Journal 687 (2) (2008) L127–L130. doi:10.1086/593204.

[69] T. Magara, A magnetohydrodynamic model focused on the configuration of magnetic field responsible for a solar penumbral microjet, The Astrophysical Journal 715 (1) (2010) L40–L43. doi:10.1088/2041-8205/715/1/l40.

[70] S. K. Tiwari, R. L. Moore, A. R. Winebarger, S. E. Alpert, Transition region/coronal signature and magnetic setting of sunspot penumbral jets: Hinode(sot/fg), hi-c, and sdo/aia observations, The Astrophysical Journal 816 (2) (2016) 92. doi:10.3847/0004-637x/816/2/92.

[71] M. Ryutova, T. Berger, Z. Frank, A. Title, On the penumbral jetlike features and chromospheric bow shocks, The Astrophysical Journal 686 (2) (2008) 1404–1419. doi:10.1086/591498.

[72] K. Reardon, A. Tritschler, Y. Katsukawa, Spectral signatures of penumbral transients, The Astrophysical Journal 779 (2) (2013) 143. doi:10.1088/0004-637x/779/2/143.

[73] D. C. Solana, L. R. B. Rubio, J. C. del Toro Iniesta, Sensitivity of spectral lines to temperature, velocity, and magnetic field, Astronomy & Astrophysics 439 (2) (2005) 687–699. doi:10.1051/0004-6361:20052720.

[74] M. C. M. Cheung, M. Schüssler, T. D. Tarbell, A. M. Title, Solar surface emerging flux regions: A comparative study of radiative MHD modeling andHinodeSOT observations, The Astrophysical Journal 687 (2) (2008) 1373–1387. doi:10.1086/591245.

[75] E.-K. Lim, V. Yurchyshyn, V. Abramenko, K. Ahn, W. Cao, P. Goode, Photospheric signatures of granular-scale flux emergence and cancellation at the penumbral boundary, The Astrophysical Journal 740 (2) (2011) 82. doi:10.1088/0004-637x/740/2/82.

[76] V. Yurchyshyn, V. Abramenko, P. R. Goode, The relationship between the occurrence of type ii spicules and the dynamics of underlying magnetic fields, AGU Fall Meeting Abstracts (2012) SH32A–05.
URL `http://adsabs.harvard.edu/abs/2012AGUFMSH32A..05Y`

[77] Z. Zeng, W. Cao, H. Ji, Observation of magntic reconnection driven by granular scale advection, The Astrophysical Journal 769 (2) (2013) L33. doi:10.1088/2041-8205/769/2/l33.

[78] X. Bai, H. Socas-Navarro, D. Nóbrega-Siverio, J. Su, Y. Deng, D. Li, W. Cao, K. Ji, Signatures of magnetic reconnection at the footpoints of fan-shaped jets on a light bridge driven by photospheric convective motions, The Astrophysical Journal 870 (2) (2019) 90. doi:10.3847/1538-4357/aaf1d1.

[79] R. Schlichenmaier, R. Rezaei, N. B. González, T. A. Waldmann, The formation of a sunspot penumbra, Astronomy and Astrophysics 512 (2010) L1. doi:10.1051/0004-6361/201014112.

[80] C. E. Fischer, J. M. Borrero, N. B. González, A. J. Kaithakkal, Observations of solar small-scale magnetic flux-sheet emergence, Astronomy & Astrophysics 622 (2019) L12. doi:10.1051/0004-6361/201834628.

[81] C. Jin, J. Wang, M. Zhao, Vector magnetic fields of solar granulation, The Astrophysical Journal 690 (1) (2008) 279–287. doi:10.1088/0004-637x/690/1/279.

[82] M. J. M. González, L. R. B. Rubio, Emergence of small-scale magnetic loops through the quiet solar atmosphere, The Astrophysical Journal 700 (2) (2009) 1391–1403. doi:10.1088/0004-637x/700/2/1391.

[83] P. Gömöry, C. Beck, H. Balthasar, J. Rybák, A. Kučera, J. Koza, H. Wöhl, Magnetic loop emergence within a granule, Astronomy and Astrophysics 511 (2010) A14. doi:10.1051/0004-6361/200912807.

[84] T. Oba, T. L. Riethmüller, S. K. Solanki, Y. Iida, C. Q. Noda, T. Shimizu, The small-scale structure of photospheric convection retrieved by a deconvolution technique applied to hinode/SP data, The Astrophysical Journal 849 (1) (2017) 7. doi:10.3847/1538-4357/aa8e44.

[85] L. Bharti, S. K. Solanki, J. Hirzberger, Lambda-shaped jets from a penumbral intrusion into a sunspot umbra: A possibility for magnetic reconnection, Astronomy & Astrophysics 597 (2017) A127. doi:10.1051/0004-6361/201629656.

[86] K. A. P. Singh, H. Isobe, K. Nishida, K. Shibata, Systematic motionof fine-scale jets and successive reconnection in solar chromosperic anemone jet observed withthe solar optical telescope/hinode, The Astrophysical Journal 760 (1) (2012) 28. doi:10.1088/0004-637x/760/1/28.

[87] K. Ahn, W. Cao, S. Shumko, J. Chae, Data pocessing of the magnetograms for the near infrared imaging spectropolarimeter at big bear solar observatory, in: AAS/Solar Physics Division Meeting, Vol. 47 of AAS/Solar Physics Division Meeting, 2016, p. 2.07.

[88] D. N. B. Hall, R. W. Noyes, T. R. Ayres, The identification of ^{13}c^{16}o in the infrared sunspot spectrum and the determination of the solar ^{12}c/^{13}c abundance ratio, The Astrophysical Journal 171 (1972) 615. doi:10.1086/151316.

[89] E. Khomenko, M. Collados, Oscillations and waves in sunspots, Living Reviews in Solar Physics 12 (1) (nov 2015). doi:10.1007/lrsp-2015-6.

[90] J. M. Beckers, R. B. Schultz, Oscillatory motions in sunspots, Solar Physics 27 (1) (1972) 61–70. doi:10.1007/bf00151770.

[91] B. W. Lites, Photoelectric observations of chromospheric sunspot oscillations. v - penumbral oscillations, The Astrophysical Journal 334 (1988) 1054. doi:10.1086/166898.

[92] J. H. Thomas, Oscillations in sunspots, Australian Journal of Physics 38 (6) (1985) 811. doi:10.1071/ph850811.

[93] T. Bogdan, Sunspot oscillations: A review, Solar Physics 192 (1/2) (2000) 373–394. doi:10.1023/a:1005225214520.

[94] I. D. Moortel, J. Ireland, A. W. Hood, R. W. Walsh, The detection of 3 & 5 min period oscillations in coronal loops, Astronomy & Astrophysics 387 (1) (2002) L13–L16. doi:10.1051/0004-6361:20020436.

[95] E. O'Shea, K. Muglach, B. Fleck, Oscillations above sunspots: Evidence for propagating waves?, Astronomy & Astrophysics 387 (2) (2002) 642–664. doi:10.1051/0004-6361:20020375.

[96] N. Brynildsen, P. Maltby, C. Foley, T. Fredvik, O. Kjeldseth-Moe, Oscillations in the umbral atmosphere, Solar Physics 221 (2) (2004) 237–260. doi:10.1023/b:sola.0000035065.10112.fc.

[97] N. I. Kobanov, D. V. Makarchik, Pulsating evershed flows and propagating waves in a sunspot, Astronomy Reports 48 (11) (2004) 954–964. doi:10.1134/1.1822978.

[98] H. Liang, L. Ma, R. Yang, H. Li, L. Zhao, Running umbral waves observed with hinode, Publications of the Astronomical Society of Japan 63 (3) (2011) 575–584. doi:10.1093/pasj/63.3.575.

[99] R. Howard, A. S. Tanenbaum, J. M. Wilcox, A new method of magnetograph observation of the photospheric brightness, velocity, and magnetic fields, Solar Physics 4 (3) (1968) 286–299. doi:10.1007/bf00149559.

[100] D. Soltau, E. H. Schroeter, H. Woehl, On velocity oscillations in sunspot umbrae., Astronomy & Astrophysics 50 (3) (1976) 367–370.

[101] B. W. Lites, A. Skumanich, V. Martinez Pillet, Vector magnetic fields of emerging solar flux. i. properties at the site of emergence, Astronomy & Astrophysics 333 (1998) 1053–1068.

[102] B. W. Lites, Photoelectric observations of chromospheric sunspot oscillations. IV - the CA II h line and he i 10830 a, The Astrophysical Journal 301 (1986) 1005. doi:10.1086/163964.

[103] S. K. Solanki, W. Livingston, K. Muglach, L. Wallace, The beat of the solar chromosphere's cold heart., Astronomy & Astrophysics 315 (1996) 303–311.

[104] R. Centeno, J. T. Bueno, H. Uitenbroek, M. Collados, The influence of coronal EUV irradiance on the emission in the he i10830 åand d3 multiplets, The Astrophysical Journal (2008).

[105] H. Tian, E. DeLuca, K. K. Reeves, S. McKillop, B. D. Pontieu, J. Martínez-Sykora, M. Carlsson, V. Hansteen, L. Kleint, M. Cheung, L. Golub, S. Saar, P. Testa, M. Weber, J. Lemen, A. Title, P. Boerner, N. Hurlburt, T. D. Tarbell, J. P. Wuelser, C. Kankelborg, S. Jaeggli, S. W. McIntosh, High-resolution observations of the shock wave behavior for sunspot oscillations with the interface region imaging spectrograph, The Astrophysical Journal 786 (2) (2014) 137. doi:10.1088/0004-637x/786/2/137.

[106] J. B. Gurman, J. W. Leibacher, R. A. Shine, B. E. Woodgate, W. Henze, Transition region oscillations in sunspots, The Astrophysical Journal 253 (1982) 939. doi:10.1086/159692.

[107] A. Fludra, Transition region oscillations above sunspots, Astronomy & Astrophysics 368 (2) (2001) 639–651. doi:10.1051/0004-6361:20000574.

[108] P. Maltby, N. Brynildsen, O. Kjeldseth-Moe, K. Wilhelm, Plumes and oscillations in the sunspot transition region, Astronomy & Astrophysics 373 (1) (2001) L1–L4. doi:10.1051/0004-6361:20010578.

[109] L. R. B. Rubio, M. Collados, B. R. Cobo, I. R. Hidalgo, Oscillations in the photosphere of a sunspot umbra from the inversion of infrared stokes profiles, The Astrophysical Journal 534 (2) (2000) 989–996. doi:10.1086/308791.

[110] K. Nagashima, T. Sekii, A. G. Kosovichev, H. Shibahashi, S. Tsuneta, K. Ichimoto, Y. Katsukawa, B. Lites, S. Nagata, T. Shimizu, R. A. Shine, Y. Suematsu, T. D. Tarbell, A. M. Title, Observations of sunspot oscillations in g band and ca II h line with solar optical telescope on hinode, Publications of the Astronomical Society of Japan 59 (sp3) (2007) S631–S636. doi:10.1093/pasj/59.sp3.s631.

[111] D. Yuan, V. M. Nakariakov, Z. Huang, B. Li, J. Su, Y. Yan, B. Tan, Oscillations in a sunspot with light bridges, The Astrophysical Journal 792 (1) (2014) 41. doi:10.1088/0004-637x/792/1/41.

[112] J. T. Su, K. F. Ji, W. Cao, D. Banerjee, T. G. Priya, J. S. Zhao, X. Y. Bai, J. Chen, M. Zhang, H. S. Ji, OBSERVATIONS OF OPPOSITELY DIRECTED UMBRAL WAVEFRONTS ROTATING IN SUNSPOTS OBTAINED FROM THE NEW SOLAR TELESCOPE OF BBSO, The Astrophysical Journal 817 (2) (2016) 117. doi:10.3847/0004-637x/817/2/117.

[113] A. Wittmann, Some properties of umbral flashes, Solar Physics 7 (3) (1969) 366–369. doi:10.1007/bf00146141.

[114] G. L. Phillis, Hα oscillations in sunspot umbrae, Solar Physics 41 (1) (1975) 71–79. doi:10.1007/bf00152957.

[115] J. B. Gurman, Sunspot umbral oscillations in mgii k, Solar Physics 108 (1) (1987) 61–75. doi:10.1007/bf00152077.

[116] L. H. M. R. van der Voort, R. J. Rutten, P. Sütterlin, P. J. Sloover, J. M. Krijger, La palma observations of umbral flashes, Astronomy & Astrophysics 403 (1) (2003) 277–285. doi:10.1051/0004-6361:20030237.

[117] B. Handy, L. Acton, C. Kankelborg, C. Wolfson, D. Akin, M. Bruner, R. Caravalho, R. Catura, R. Chevalier, D. Duncan, C. Edwards, C. Feinstein, S. Freeland, F. Friedlaender, C. Hoffmann, N. Hurlburt, B. Jurcevich, N. Katz, G. Kelly,

J. Lemen, M. Levay, R. Lindgren, D. Mathur, S. Meyer, S. Morrison, M. Morrison, R. Nightingale, T. Pope, R. Rehse, C. Schrijver, R. Shine, L. Shing, K. Strong, T. Tarbell, A. Title, D. Torgerson, L. Golub, J. Bookbinder, D. Caldwell, P. Cheimets, W. Davis, E. Deluca, R. McMullen, H. Warren, D. Amato, R. Fisher, H. Maldonado, C. Parkinson, The transition region and coronal explorer, Solar Physics 187 (2) (1999) 229–260. doi:10.1023/a:1005166902804.

[118] V. M. Nakariakov, E. Verwichte, D. Berghmans, E. Robbrecht, Slow magnetoacoustic waves in coronal loops, Astronomy & Astrophysics 362 (2000) 1151–1157.

[119] V. M. Uritsky, J. M. Davila, N. M. Viall, L. Ofman, Measuring temperature-dependent propagating disturbances in coronal an loops using multiple SDO/AIA channels and the surfing transform technique, The Astrophysical Journal 778 (1) (2013) 26. doi:10.1088/0004-637x/778/1/26.

[120] K. Shibasaki, Microwave detection of umbral oscillation in NOAA active region 8156: Diagnostics of temperature minimum in sunspot, The Astrophysical Journal 550 (2) (2001) 1113–1118. doi:10.1086/319820.

[121] G. B. Gelfreikh, Y. T. Tsap, Y. G. Kopylova, T. B. Goldvarg, Y. A. Nagovitsyn, L. I. Tsvetkov, Variations of microwave emission from solar active regions, Astronomy Letters 30 (7) (2004) 489–495. doi:10.1134/1.1774401.

[122] R. A. Sych, V. M. Nakariakov, The pixelised wavelet filtering method to study waves and oscillations in time sequences of solar atmospheric images, Solar Physics 248 (2) (2007) 395–408. doi:10.1007/s11207-007-9005-7.

[123] T. R. Ayres, G. R. Wiedemann, Non-LTE CO, revisited, The Astrophysical Journal 338 (1989) 1033. doi:10.1086/167256.

[124] D. Goorvitch, Infrared CO line for the x 1 sigma state, The Astrophysical Journal Supplement Series 95 (1994) 535. doi:10.1086/192110.

[125] S. K. Solanki, W. Livingston, T. Ayres, New light on the heart of darkness of the solar chromosphere, Science 263 (5143) (1994) 64–66. doi:10.1126/science.263.5143.64.

[126] H. Uitenbroek, The CO fundamental vibration-rotation lines in the solar spectrum. i. imaging spectroscopy and multidimensional LTE modeling, The Astrophysical Journal 531 (1) (2000) 571–584. doi:10.1086/308454.

[127] T. R. Ayres, C. Plymate, C. U. Keller, Solar carbon monoxide, thermal profiling, and the abundances of c, o, and their isotopes, The Astrophysical Journal Supplement Series 165 (2) (2006) 618–651. doi:10.1086/504847.

[128] R. W. Noyes, D. N. B. Hall, Thermal oscillations in the high solar photosphere, The Astrophysical Journal 176 (1972) L89. doi:10.1086/181027.

[129] T. R. Ayres, J. W. Brault, Fourier transform spectrometer observations of solar carbon monoxide. III - time-resolved spectroscopy of the delta v = 1 bands, The Astrophysical Journal 363 (1990) 705. doi:10.1086/169377.

[130] J. R. Lemen, A. M. Title, D. J. Akin, P. F. Boerner, C. Chou, J. F. Drake, D. W. Duncan, C. G. Edwards, F. M. Friedlaender, G. F. Heyman, N. E. Hurlburt, N. L. Katz, G. D. Kushner, M. Levay, R. W. Lindgren, D. P. Mathur, E. L. McFeaters, S. Mitchell, R. A. Rehse, C. J. Schrijver, L. A. Springer, R. A. Stern, T. D. Tarbell, J. Wuelser, C. J. Wolfson, C. Yanari, J. A. Bookbinder, P. N. Cheimets, D. Caldwell, E. E. Deluca, R. Gates, L. Golub, S. Park, W. A. Podgorski, R. I. Bush, P. H. Scherrer, M. A. Gummin, P. Smith, G. Auker, P. Jerram, P. Pool, R. Soufli, D. L. Windt, S. Beardsley, M. Clapp, J. Lang, N. Waltham, The atmospheric imaging assembly (AIA) on the solar dynamics observatory (SDO), Solar Physics 275 (1-2) (2011) 17–40. doi:10.1007/s11207-011-9776-8.

[131] J. Evershed, Radial movement in sun-spots, Monthly Notices of the Royal Astronomical Society 69 (5) (1909) 454–458. doi:10.1093/mnras/69.5.454.

[132] H. Uitenbroek, R. W. Noyes, D. Rabin, Imaging spectroscopy of the solar CO lines at 4.67 microns, The Astrophysical Journal 432 (1994) L67. doi:10.1086/187513.

[133] J. Leenaarts, T. M. D. Pereira, M. Carlsson, H. Uitenbroek, B. D. Pontieu, The formation ofirisdiagnostics. i. a quintessential model atom of mg ii and genera formation properties of the mg ii h & k lines, The Astrophysical Journal 772 (2) (2013) 89. doi:10.1088/0004-637x/772/2/89.

[134] J. Leenaarts, T. M. D. Pereira, M. Carlsson, H. Uitenbroek, B. D. Pontieu, The formation ofirisdiagnostics. II. the formation of the mg II h & k lines in the solar atmosphere, The Astrophysical Journal 772 (2) (2013) 90. doi:10.1088/0004-637x/772/2/90.

[135] X. Cheng, M. D. Ding, C. Fang, Imaging and spectroscopic diagnostics on the formation of two magnetic flux ropes revealed by SDO/AIA and IRIS, The Astrophysical Journal 804 (2) (2015) 82. doi:10.1088/0004-637x/804/2/82.

[136] Q.Li, N. Deng, J. Jing, H. Wang, High-resolution observations of downflows at one end of a pre-eruption filament, The Astrophysical Journal 841 (2) (2017) 112. doi:10.3847/1538-4357/aa6faa.

[137] R. Centeno, M. Collados, J. T. Bueno, Spectropolarimetric investigation of the propagation of magnetoacoustic waves and shock formation in sunspot atmospheres, The Astrophysical Journal 640 (2) (2006) 1153–1162. doi:10.1086/500185.

[138] S. Bard, M. Carlsson, Radiative hydrodynamic simulations of acoustic waves in sunspots, The Astrophysical Journal 722 (1) (2010) 888–898. doi:10.1088/0004-637x/722/1/888.

[139] H. Tian, S. W. McIntosh, T. Wang, L. Ofman, B. D. Pontieu, D. E. Innes, H. Peter, Persistent doppler shift oscillations observed with hinode/EIS in the solar corona: Spectroscopic signatures of alfvénic waves and recurring upflows, The Astrophysical Journal 759 (2) (2012) 144. doi:10.1088/0004-637x/759/2/144.

[140] D. Li, D. Yuan, Y. N. Su, Q. M. Zhang, W. Su, Z. J. Ning, Non-damping oscillations at flaring loops, Astronomy & Astrophysics 617 (2018) A86. doi:10.1051/0004-6361/201832991.

[141] J. D. Scargle, Studies in astronomical time series analysis. II - statistical aspects of spectral analysis of unevenly spaced data, The Astrophysical Journal 263 (1982) 835. doi:10.1086/160554.

[142] D. Yuan, V. M. Nakariakov, N. Chorley, C. Foullon, Leakage of long-period oscillations from the chromosphere to the corona, Astronomy & Astrophysics 533 (2011) A116. doi:10.1051/0004-6361/201116933.

[143] J. H. Horne, S. L. Baliunas, A prescription for period analysis of unevenly sampled time series, The Astrophysical Journal 302 (1986) 757. doi:10.1086/164037.

[144] H. Tian, P. R. Young, K. K. Reeves, T. Wang, P. Antolin, B. Chen, J. He, Global sausage oscillation of solar flare loops detected by the interface region imaging spectrograph, The Astrophysical Journal 823 (1) (2016) L16. doi:10.3847/2041-8205/823/1/l16.

[145] H. Zirin, A. Stein, Observations of running penumbral waves, The Astrophysical Journal 178 (1972) L85. doi:10.1086/181089.

[146] G. Tsiropoula, C. E. Alissandrakis, P. Mein, Association of chromospheric sunspot umbral oscillations and running penumbral waves. I. Morphological study, Astronomy & Astrophysics 355 (2000) 375–380.

[147] K. Tziotziou, G. Tsiropoula, P. Mein, Ca II 8542 åsunspot oscillations observed with themis, Astronomy & Astrophysics 381 (1) (2002) 279–289. doi:10.1051/0004-6361:20011419.

[148] K. Tziotziou, G. Tsiropoula, N. Mein, P. Mein, Observational characteristics and association of umbral oscillations and running penumbral waves, Astronomy & Astrophysics 456 (2) (2006) 689–695. doi:10.1051/0004-6361:20064997.

[149] D. S. Bloomfield, A. Lagg, S. K. Solanki, The nature of running penumbral waves revealed, The Astrophysical Journal 671 (1) (2007) 1005–1012. doi:10.1086/523266.

[150] I. Ruedi, S. Solanki, C. Keller, C. Frutiger, Infrared lines as probes of solar magnetic features. xiv. ti i and the cool components of sunspots, Astronomy and Astrophysics 338 (1998) 1089–1101.

[151] A. A. Ramos, I. S. Requerey, N. Vitas, DeepVel: Deep learning for the estimation of horizontal velocities at the solar surface, Astronomy & Astrophysics 604 (2017) A11. doi:10.1051/0004-6361/201730783.

[152] M. J. Penn, T. Schad, E. Cox, Probing the solar atmosphere using oscillations of infrared co spectral lines, The Astrophysical Journal 734 (1) (2011) 47. doi:10.1088/0004-637x/734/1/47.